Transient Growth in Rayleigh-Bénard-Poiseuille/Couette flows

J. John Soundar Jerome

To cite this version:

J. John Soundar Jerome. Transient Growth in Rayleigh-Bénard-Poiseuille/Couette flows. Fluids mechanics [physics.class-ph]. Ecole Polytechnique X, 2011. English. NNT : . pastel-00680236

HAL Id: pastel-00680236

https://pastel.hal.science/pastel-00680236

Submitted on 29 Mar 2012

HAL is a multi-disciplinary open access archive for the deposit and dissemination of scientific research documents, whether they are published or not. The documents may come from teaching and research institutions in France or abroad, or from public or private research centers.

L'archive ouverte pluridisciplinaire **HAL**, est destinée au dépôt et à la diffusion de documents scientifiques de niveau recherche, publiés ou non, émanant des établissements d'enseignement et de recherche français ou étrangers, des laboratoires publics ou privés.

École Polytechnique
Laboratoire d'Hydrodynamique

Thèse présentée pour obtenir le grade de

DOCTEUR DE L'ÉCOLE POLYTECHNIQUE

Spécialité : Mécanique

par

J John Soundar Jerome

Transient growth in Rayleigh-Bénard-Poiseuille/Couette flows

Soutenance prévue le 17 octobre 2011 devant le jury composé de

Jean-Marc CHOMAZ	directeur de thèse	LadHyX, Palaiseau, FR
Patrick HUERRE	directeur de thèse	LadHyX, Palaiseau, FR
Alessandro BOTTARO	rapporteur	DICAT, Genova, IT
Colm-cille P. CAULFIELD	rapporteur	DAMTP, Cambridge, UK
François GALLAIRE	examinateur	EPFL, Laussane, SWI
Jean-Christophe ROBINET	examinateur	DYNFLUID, Paris, FR
Peter J. SCHMID	examinateur	LadHyX, Palaiseau, FR

Contents

I Transient Growth in Rayleigh-Bénard-Poiseuille/Couette flows 19

1 Introduction 21
- 1.1 Basic concepts 22
  - 1.1.1 Method of normal modes 22
  - 1.1.2 Transient growth analysis 24
- 1.2 Rayleigh-Bénard-Poiseuille/Couette flows 27
  - 1.2.1 Motivation 27
  - 1.2.2 A brief history of RBP and RBC flows: Modal stability 28
  - 1.2.3 A brief history of RBP and RBC flows: Non-modal stability 31
- 1.3 Objective 32

2 Linear stability analysis of RBP and RBC flows 33
- 2.1 Base flow 33
- 2.2 Governing Equations 34
- 2.3 Squire's transformation 38
- 2.4 Adjoint equations and the norm 38

3 Modal Stability Analysis 41
- 3.1 Formulation 41
- 3.2 Squire's Theorem in RBP and RBC flows 42
- 3.3 Numerical Technique 42
  - 3.3.1 Chebyshev discretization of the governing equations 42
  - 3.3.2 Validation 45
- 3.4 Modal stability characteristics 45
  - 3.4.1 Road to the stability diagram 45
  - 3.4.2 Dominant modal instability 54

4 Non-modal Stability Analysis 57
- 4.1 Road to Santiago 57
  - 4.1.1 Choice of an appropriate norm 57
  - 4.1.2 Computational method 58
  - 4.1.3 Validation 62
- 4.2 Results: Non-modal stability analysis 62
  - 4.2.1 Effect of varying Rayleigh number at constant Reynolds number . 62

4.2.2 Effect of varying Reynolds number at constant Rayleigh number . 64
4.2.3 Domain of Transient Growth 75
4.3 Transient growth of streamwise-uniform disturbances in RBP and RBC flows 76
4.3.1 Lift-up Mechanism in the presence of temperature perturbations . 76
4.3.2 Short-time dynamics 79
4.3.3 Reynolds number scaling for $G_{max}(\alpha, \beta; Re, Ra, Pr)$ 80
4.3.4 Long-time Optimal Response 81
4.3.5 Transient Growth at arbitrary time 82
4.3.6 Effect of Prandtl number 83
4.3.7 Effect of the norm $\|\boldsymbol{q}\|_\gamma$ 87
4.4 Conclusion 92

II Consequences of the Squire transformation on 3D Optimal Perturbations 95

5 Squire's transformation and 3D disturbances 97
5.1 Introduction 97
5.2 Governing equations 97
5.3 Consequences on the eigenfunctions 99
5.4 Consequences on long-time optimal gains 102
5.4.1 Case (1): Streamwise-uniform disturbances ($\alpha = 0$) 103
5.4.2 Case (2): $3D$ long-time optimal perturbations 104
5.5 Discussion 108
5.6 Conclusion 110

6 Remarks and Perspectives 111

Bibliography 120

List of Figures

1.1 Bénard cells in spermaceti[10]. 23
1.2 Schematic of the lift-up mechanism. 24
1.3 Schematic of the Orr mechanism [34]. 25
1.4 Schematic of “longitudinal” rolls as observed by Bénard and Avsec (1938) 28
1.5 Sketch of Idrac’s experiment (1920). It accounts for the first published result of “longitudinal” convection rolls. 29
1.6 Cloud-streets as formed due to the presence of convection rolls aligned along the shear of the atmospheric boundary layers [79]. This photograph was taken from a Japan Coast Guard aircraft off the north-eastern coast of Hokkaido. It shows a bird’s-eye view of cloud streets over the Sea of Okhotsk. According to the source [59], these clouds floated just over the sea surface, stood 300 meters tall and stretched for over 100 kilometers. . 29
1.7 Rotating disk experiments from Ingersoll [43]: Nusselt number as a function of Rayleigh number for various Reynolds numbers. 31

2.1 Schematic view of Rayleigh-Bénard-Couette (top) and Rayleigh-Bénard-Poiseuille (bottom) flows. 34

3.1 Growth rate ω_i^{max} of the dominant streamwise-uniform ($\alpha = 0$) eigenmode in Rayleigh-Bénard-Poiseuille/Couette flow at various Rayleigh numbers: $- - - -$ $Ra = 1856$, —— $Ra = 1707.78$, and $- \cdot - \cdot -$ $Ra = 1536$ when $Pr = 1$ for all Reynolds numbers (see discussion in the text) 47
3.2 Growth rate ω_i^{max} of the dominant spanwise-uniform ($\beta = 0$) eigenmode ω_i^{max} in RBP flow: $Re = 3510$, $Ra = 4.85 \times 10^7$ and $Pr = 1$ 48
3.3 Growth rate ω_i^{max} of the dominant spanwise-uniform ($\beta = 0$) eigenmode ω_i^{max} in RBP flow: $Re = 90$, $Ra = 31329$ and $Pr = 1$. 48
3.4 Growth rate ω_i^{max} of the dominant spanwise-uniform ($\beta = 0$) eigenmode ω_i^{max} in RBC flow: $Re = 3000$, $Ra = 1.64 \times 10^8$ and $Pr = 1$. 49
3.5 Rayleigh-Bénard-Poiseuille flow: Critical phase speed $c_r = \omega_r/\alpha$ versus Reynolds number of the first few dominant spanwise-uniform eigenmodes ($\beta = 0$); □ - transverse rolls, ○ - Tollmien-Schlichting waves and ◁ - W-modes 50
3.6 Rayleigh-Bénard-Poiseuille flow: Critical wavenumber α_{crit} versus Reynolds number of the first few dominant spanwise-uniform eigenmodes ($\beta = 0$); □ - transverse rolls, ○ - Tollmien-Schlichting waves and ◁ - W-modes . . . 50

3.7 Rayleigh-Bénard-Couette flow: Critical phase speed c_r versus Reynolds number of the first few dominant spanwise-uniform eigenmodes ($\beta = 0$); ☐ - Non-stationary modes, and ○ - Stationary modes 51

3.8 Rayleigh-Bénard-Couette flow: Critical wavenumber α_{crit} versus Reynolds number of the first few dominant spanwise-uniform eigenmodes ($\beta = 0$); ☐ - Non-stationary modes, and ○ - Stationary modes 51

3.9 Rayleigh-Bénard-Couette flow: Velocity vector plots and temperature contours of spanwise-uniform perturbations ($\beta = 0$) at $Re = 1000$: (a) stationary mode ($\alpha = 0.05472$) and (b) non-stationary mode ($\alpha = 3.375$) when $Ra = 6.343 \times 10^6$ and $Ra = 1.807 \times 10^7$, respectively. 53

3.10 Rayleigh-Bénard-Poiseuille flow: Velocity vector plots and temperature contours of transverse rolls ($\alpha = 11$, $\beta = 0$) at $Re = 3510$ and $Ra = 4.8\times10^7$. 54

3.11 Marginal Stability Diagram of Rayleigh-Bénard-Poiseuille flow for $Pr = 1$: (——) streamwise-uniform ($\alpha = 0$) Rayleigh-Bénard convection rolls (RB), ($-\,-\,-$) Transverse Rolls (TR), ($\cdot - \cdot - \cdot$) Tollmien-Schlichting (TS) waves and ($\cdot\cdot\cdot\cdot\cdot$) Oblique Rolls ($OR$), $\alpha/\beta = 9.95$. The flow is linearly stable in the hatched rectangular region formed by the lines corresponding to the onset of the RB and TS modes at the lower left of the plot. 56

3.12 Marginal Stability Diagram of Rayleigh-Bénard-Couette for $Pr = 1$: (——) streamwise-uniform ($\alpha = 0$) Rayleigh-Bénard convection Rolls (RB), ($-\,-\,-$) Stationary spanwise-uniform mode (SM), ($-\cdot\cdot-$) Non-stationary spanwise-uniform mode (NSM), ($\cdot - \cdot - \cdot$) Oblique stationary spanwise-uniform mode (OSM): $\alpha/\beta = 9.95$. The flow is linearly stable everywhere in the hatched region below the continuous line corresponding to the onset of the RB mode. 56

4.1 Convergence of the computed value of G_{max} with respect to the number of eigenmodes M considered for computations of transient growth: $Re = 1000$, $Pr = 1$ and ○ $Ra = 0$, ☐ $Ra = 500$ ($\alpha = 0$, $\beta = 1.8$). 63

4.2 Contour plot of $\log G_{max}$ for RBP at $Re = 1000$, $Pr = 1$, and $(a)Ra = 0$, $(b)Ra = 500$, $(c)Ra = 1500$ and $(d)Ra = 1700$. The dashed lines correspond to iso-lines of the growth $G_{max} = \frac{2}{3}S$. 66

4.3 Contour plot of $\log G_{max}$ for RBC at $Re = 1000$, $Pr = 1$, and $(a)Ra = 0$, $(b)Ra = 500$, $(c)Ra = 1500$ and $(d)Ra = 1700$. The dashed lines correspond to iso-lines of the growth $G_{max} = \frac{2}{3}S$. 68

4.4 Contour plot of t_{max} for RBP at $Re = 1000$, $Pr = 1$, and $(a)Ra = 0$, $(b)Ra = 500$, $(c)Ra = 1500$ and $(d)Ra = 1700$. The dashed lines correspond to iso-lines of $t_{max} = \frac{2}{3}T_{max}$, where T_{max} is the global maximum of all t_{max} in the α-β plane. 70

4.5 Contour plot of t_{max} for RBC at $Re = 1000$, $Pr = 1$, and $(a)Ra = 0$, $(b)Ra = 500$, $(c)Ra = 1500$ and $(d)Ra = 1700$. The dashed lines correspond to iso-lines of $t_{max} = \frac{2}{3}T_{max}$, where T_{max} is the global maximum of all t_{max} in the α-β plane. 72

4.6 Effect of Rayleigh number on (a) G_{max} and (b) t_{max} in RBP for streamwise-uniform disturbances of various spanwise wavenumbers β at $Re = 1000$, $Pr = 1$, and $+Ra = 0$, $\triangle Ra = 500$ and $\circ Ra = 1500$. 73

4.7 Optimal growth curves at various Reynolds numbers for streamwise-uniform disturbances in RBP at $Ra = 1500$ ($\alpha = 0$, $\beta = 2.04$): —— $Re = 5000$, $\times$ $Re = 1000$, $+$ $Re = 500$, $\diamond$ $Re = 300$, $\Box$ $Re = 200$, $\circ$ $Re = 100$ and $- - -$ $Ra = 0$, $Re = 5000$ 74

4.8 Optimal growth curves at various Reynolds numbers for streamwise-uniform disturbances in RBC at $Ra = 1000$ ($\alpha = 0$, $\beta = 1.558$): —— $Re = 5000$, $\triangleleft$ $Re = 3000$, $+$ $Re = 2000$, $\times$ $Re = 1000$, $\circ$ $Re = 400$, $\Box$ $Re = 200$ and $- - -$ $Ra = 0$, $Re = 5000$ 75

4.9 Same as figure 4.8 at a supercritical Rayleigh number $Ra = 1800$ 76

4.10 Contours of global maximum transient growth S in Rayleigh-Bénard-Poiseuille flow ($Pr = 1$). For any Ra and Re in the hatched region that is bounded by the thick line and the axes, $S = 1$ wherein the flow is monotonically stable. The symbols denote the numerical results of Shuhlze and Carmi (1976). 77

4.11 Same as in figure 4.10 but for Rayleigh-Bénard-Couette flow. The symbols $\Box$ and $\diamond$ denote the theoretical results of Joseph (1966) and the numerical results of Shuhlze and Carmi (1976). 78

4.12 *RBP* flow: Comparison between computed optimal gain curve (——) and the asymptotic estimates for short and large times ($- - -$) at various Rayleigh numbers (from inside to outside: $Ra = 300, 500, 800, 1000, 1500, 1700$) at $Re = 1000$, $Pr = 1$, $\alpha = 0$ and $\beta = 2.04$ 84

4.13 *RBC* flow: Comparison between computed optimal gain curve (——) and the asymptotic estimates for short and large times ($- - -$) at various Rayleigh numbers (from inside to outside: $Ra = 300, 500, 800, 1000, 1500, 1700$) at $Re = 1000$, $Pr = 1$, $\alpha = 0$ and $\beta = 1.558$ 85

4.14 Time history of the growth $\frac{\|\boldsymbol{q}\|^2_{RB}}{\|\boldsymbol{q}_0\|^2_{RB}}$ with $\boldsymbol{q}_0$ being the optimal input at each time horizon (——); optimal input corresponding to G_{max} ($\cdot - \cdot - \cdot$) and dominant-adjoint-mode input ($- - -$) at $Re = 1000$, $Ra = 1000$, $Pr = 1$, $\alpha = 0$ and $\beta = 1.558$. 86

4.15 Optimal growth at different Reynolds numbers in *RBP* flow at $Ra = 1000$ and $Pr = 10^{-2}$ ($\alpha = 0$, $\beta = 1.8$): —— $Re = 5000$, $\times$ $Re = 2000$, $+$ $Re = 1000$, $\diamond$ $Re = 500$, $\Box$ $Re = 300$, $\circ$ $Re = 100$ and $- - -$ $Ra = 0$, $Re = 5000$ 87

4.16 Optimal gain at various Prandtl numbers when $Re = 1000$, $\alpha = 0$ and $\beta = 1.558$ for $Ra = 0$ ($- - --$) and $Ra = 1700$ (——): $\circ$ $Pr = 10^2$, $\Box$ $Pr = 10$, $\triangleleft$ $Pr = 1$, $\triangle$ $Pr = 10^{-1}$, $\triangleright$ $Pr = 10^{-2}$, ∇ $Pr = 10^{-3}$ and $*$ $Pr = 10^{-4}$. 88

4.17 Effect of Prandtl number on G_{max} ($Re = 1000$, $\alpha = 0$ and $\beta = 1.558$) . . 88

4.18 Effect of Prandtl number on the optimal gain curves ($Pr = 10^{-3}$ ——; $Pr = 10^2$ $\cdots\cdots$); Time evolution of the growth of perturbations $\frac{\|\boldsymbol{q}\|^2_{RB}}{\|\boldsymbol{q}_0\|^2_{RB}}$, where $\boldsymbol{q}_0$ is the normalised adjoint of the leading eigenmode ($Pr = 10^{-3}$ $- - -$; $Pr = 10^2$ $- \cdot \cdot -$) at $Re = 1000$, $\alpha = 0$ and $\beta = 2.04$. 89

4.19 Optimal gain computations for the norm $\|\boldsymbol{q}\|_\gamma$ with $\gamma = 1$ at $Re = 1000$, $Pr = 1$ and $\Box$ $Ra = 0$, $\diamond$ $Ra = 500$, $\circ$ $Ra = 1500$: (a) $\beta = 0$, (b) $\beta = 1$, (c) $\alpha = 0$ and (d) $\alpha = 1$ 90

4.20 Optimal gain in RBP as computed for the norm $\|\boldsymbol{q}\|_\gamma$ for $\gamma = 1$ at $Ra = 1300$ ($\alpha = 0$, $\beta = 2.04$): —— $Re = 5000$, $\times$ $Re = 2000$, $\cdot$ $Re = 1000$, $+$ $Re = 500$, $\triangle$ $Re = 200$, $\circ$ $Re = 100$, $\Box$ $Re = 50$ and $- - -$ $Ra = 0$, $Re = 5000$ 91

4.21 Optimal gain curve (——) and time evolution of the growth of perturbations $\frac{\|\boldsymbol{q}\|^2_{\gamma=1}}{\|\boldsymbol{q}_0\|^2_{\gamma=1}}$, where $\boldsymbol{q}_0$ is the normalized adjoint of the leading eigenmode $(- - --)$, the optimal initial condition corresponding to the maximum optimal gain $(- \cdot - \cdot -)$ and the normalized Rayleigh-Bénard mode without its streamwise velocity component $(\cdots\cdots)$ at $Re = 1000$, $Ra = 1300$, $Pr = 1$, $\alpha = 0$ and $\beta = 2.04$ for $\gamma = 1$. 93

5.1 Direct computations in Plane Poiseuille flow for $\alpha = 1$, $\beta = 0$ and $Re = 1000$: Temporal variation of optimal gain (——) and the growth of perturbations $Z = \frac{\|\boldsymbol{q}(t)\|^2}{\|\boldsymbol{q}(t_0)\|^2}$ for various normalized initial conditions: adjoint of the leading OS-mode $(- \cdot \cdot -)$, adjoint of the leading SQ-mode $(- \cdot - \cdot)$, leading OS-mode $(\cdot \cdot \cdot \cdot \cdot)$ and leading SQ-mode $(- - -)$ at $Re_{2D} = 1000$ and $\alpha_{2D} = 1$, $\beta_{2D} = 0$. 105

5.2 Direct computations in Plane Poiseuille flow for $\alpha = \frac{1}{\sqrt{2}}$, $\beta = \frac{1}{\sqrt{2}}$ and $Re = 1414.2$: Same as figure 5.1. 106

5.3 Direct computations in Plane Poiseuille flow for $\alpha = 0.1$, $\beta = 0.9949$ and $Re = 10^4$: Same as figure 5.1. 106

5.4 Direct computations in Plane Poiseuille flow for $\alpha = 0.01$, $\beta = 0.99995$ and $Re = 10^5$: Same as figure 5.1. 107

5.5 Direct computations in Plane Poiseuille flow for when $Re = 10^5$ and $\alpha = 0$, $\beta = 1$: Same as figure 5.1 107

5.6 Plane Poiseuille flow at $Re_{2D} = 3000$ and $\alpha_{2D} = 1$, $\beta_{2D} = 0$: Same as figure 5.1 when $\alpha = 1$, $\beta = 0$ and $Re = 3000$. 108

List of Tables

3.1 Comparison of the critical Rayleigh numbers for transverse $2D$ rolls (spanwise-uniform mode) in RBP when $Pr = 1$ $(N = 100)$. 45

Acknowledgement

If it was not for my mother and father who brought me to this beautiful, mysterious and turbulent world; if my school teachers had never taught me to be obedient and listen to them; if Ravichandran sir never nurtured my curiosity in botany; if i had not heard about my first inspiration, Mendel and his laws; if my family had not had a lovely backyard garden (my first-ever field-lab); if Vinoth Babu and Bala Yeshwanth Ram did not collect stamps, play cricket and nintendo, take the same school bus, go scouting and camping; if Mari Muthu sir had chose not to come to Chellammal Vidyalaya; if Paul mama did not take matters in his hand (and God bless him because he did!); if San-Thome high school had never even existed and if Ravichandran sir and Sampath sir had never worked there; if Victor and Venkataraghavan talked about contemporary Indian philosophy instead of relativity and quantum mechanics; if Srinivasan sir, Iyengaran sir and Iyyappen sir were unpopular in K. K. Nagar and Saligramam; if they were less inspiring and dull at their tuitions; if Annamalai and Ravikanth did not stop-by for a chat after tuitions; if Rohit Dinakar, Vivek, Venkataraman and Pramod had registered for tuitions in Saligramam; if Madras Insitiue of Technology's own library had had only little books on modern physics and higher mathematics; if Prof. Bhaskaran had stopped coming to the aerospace department way before 2004 (because some teachers just inspire you with their mere presence and have you ever noticed that?); if Dhanaraj sir, B. T. N. Sridhar sir and Elangoven sir were experts in engineering drawing or electrical systems and if they had not had a clue about fluid mechanics, aerodynamics and shockwaves; if Krishna Chaitanya was mean, unfriendly and cheerless and if he had not been friends with Rajesh the witty and practical, Rohan Vishwanathan the merry-go-friend and Priya Anita the cheerful friend gal; if Bharani Ravishankar and Sangeetha had not been kind and lovely with their words and action; if Anand Narayanan had not asked me to look beyond mathematical physics and into modern analysis and algebraic topology; if some memorable football had not been played every week with him, Yogeshwaran, Srivatsan, Karthik and Anand junior; if Rajesh (state), Rajesh and Rakesh had not given me some good lessons of cricket; If Sriram had always missed the $G73$ bus to Vadapalani that I took; if chance had never come my way and so if i had not met Abishek Ravi, a gem of friend (more of a brother to me, back then); and if Abi had not been boyfriend's with Uma Sekar, another gem of friend (even when we are not in touch); if Cognizant Technology Solutions was the only way out for an inspired mind caught in an engineering school and if GATE exams and MHRD scholarships had not been introduced by some good-hearted old Indians; if the aerospace engineering department of IISc had never recruited Prof. Joseph Mathew the authoritative, insightful teacher, Prof. O N Ramesh the vivid/animated, stimulating teacher and Prof. Jyothimar Dey the candid teacher; if the inspiring demeaner and stimulating lectures of Prof. Kumaran and Prof. Rahul Pandit had been by chance absent at IISc; if making friends had been difficult at IISc; if IISc's campus, its library, the mornings and evenings in the Maleswaram market and Sankey tank had not been just as lovely as they were; if Venkata Subrahmanyam, Vadivel senior, Anzar Bhai, Ram Kumar, Kannan senior had not been kind, friendly, ready-to-help and encouraging; if the witty, good friend Varun Kulkarni had chosen to live in R-block in stead of PD-Block; if Senthil Kumar had always avoided me hanging out with him and had not been a eccentric, intelligent, motivating, cynical, lovely person and friend to me; if Preeta and i had shied away from each other; if Guruji had taught me only to play Snooker; if Prof. Mathew had chosen to ignore my enthusiasm to work with him; if he had not understood my urge and determination for analytical methods and mathematical models and had kept me ignorant about Patrick Huerre and Jean-Marc Chomaz in France; if my undergraduate score was more than 8.5 and hence, if Berkeley had took me in; if France and India had dreaded each other and discouraged any immigration and talent exchange; if i had not had a chance to know and work together with someone like Patrick Huerre who, sometimes oddly by his mere presence, inspire and instill you with self-confidence and sprout your hope at your second-class, yet-to-mature research; if Jean-Marc Chomaz had reserved his Pandora box of ideas from his students; if i had not taken the roller-coaster ride inside his Pandora box past his graffiti-explanations and franglish-narrations; if he had not always been hopeful, encouraging and patient with me; if I had not been alone and tongue-tied for the first 3 months in CROUS and had that crushed me into pieces; if it had not been for kind friends like Sonia Poullain, Taj, Yogeshwaran, Maria-Luisa Cordero, Cristobal Arratia, Gianluca Meneghello, Giorgio Krstulović and Gustavo Düring; and if Chileans had not had their mafia in Paris, like for example, if Cristobal did not hang out with Jaime Arancibia Monreal, Jorge Zamorano, Miguel Trejo, Lucho Briceno, Mario Bravo, Carolina Oviedo Aguilar, Claudia Márquez Thomas, Francisca Gutierrez Crocco; and if he had not met Marie Hjeltman, the shy, kind one from Sweden; if they all had not been so very generous, cheerful, passionate and dance-loving; if Sheriyar had always ignored and shunted me off every time i ran to him for help, advise and talk; if Rémi Violette had not by chance told me about rock climbing and when I went to the forest with Xavier Garnaud, Rémi Dangla and Mathieu Rodriguez, if only the Fontainebleau forest had not been as magical as it has always been; Rémi Dangla and me had refrained from the generous, always-smiling Romain Meyrand at the gym and if he had not been friends with the cheerful Corrine Sullivan, the impeccable zen Wietze Herreman and the sweet Liesbeth Vanmol; if the quirky-humored Pierre-Thomas Brun and the kind Victoria Campbell did not know Rémi D.; if Yongyun Hwang, the quick-smart, hard-working Korean had chosen to goto the USA and ignored my lack of education in modern fluid stability; if some of the gradate students (the French-humoured Joran, the girl with a honest laugh Madiha Ahmed, the outspoken Mathieu R., the sweet and my sisterly Elena, the good-friendly, cheerful, my elder brotherly Cristobal, the good-hearted, welcoming Xavier, my younger brotherly, Spain-loving, happy-weather, ever-present Miguel Fosas de Pándo, the sweet girl with the brightest smile, Nadia Vertti and the ever-German Franz) in LadHyX were are all nerds, eating sandwiches in front the screen and blissfully ignorant about others during weekends; if LadHyX had been less of a family without Fulvio Martinelli, Eletta Negretti, Paul Manneville (another with an inspiring demeanor), Paul Billant, Sabin Ortiz, Lutz Lesshafft, Daniel Guy (the kind and generous), Antonio Garcia, Thérèse Lescuyer, Sandrine Laguerre, François Gallaire, Christophe Clanet (another stimulating mind), Charles Baroud (the friendly, welcoming, ready-to-help, witty), Peter Schmid, Emmanuel de Langre (another with an inspiring demeanor), Alexandre Rosinski (always has a hand to give and always with a smile), Pascal Hémon and Caroline Frot; if Sonia Poullain and Miguel Fosas de Pándo had continued to stay in CROUS while the ever-so-merry Alba Gonzalez Aldea, the party-guy Emanuele Bezzecchi, the considerate Italian Francesco Fiore, the Spanglish blonde Catherine Holmes Lyn and the jolly Catalan Enric Roca randomly came to Paris at the Cité Universitaire; if they had not been so much of a fine family for me in 2010; if Gianluca had never introduced me to Chiara Pettenella; if the outspoken, dandy-n-generous Clément Fallet and the kind-n-lovely Sarah Moulin from Melun had despised Indians after their first trip to India; if he had not brightly invited me over for one of his many evenings and if i had not stumbled upon Aline Martin, Pierre Dabre, Aude Charrier, Emile Laurent, Chloé Laizeau, Bertrand Eyraud and many others; if the affable, witty Julien Labaune had refrained from a simple hand-shake and some pleasant talk; if the compassionate Diego Lopez had not been friends with the sweet climbing geek Hugo Jacquin and if they both had been late to the queue, say, for example, 4'O clock in the morning, for Roc14's registration; if the patriotic, outspoken, quirky, friendly Hugo Jacquin had not been friends with the jeu-de-mots experts Corentin Coulais, the most-considerate and Simone Thalabard, the impulsive and eccentric; and with them and i, if the sweet Bretonne princesse Fanny Chereau and Miss sunshine Christelle Der Loughian had not been part of our travels and adventures; if Adrien Benusiglio, Caroline Cohen and Baptiste Darbois Texier had not been the sweetest of the people that i have known; and if Pascal Raux, Alexandre Ponomarenko, Keyvan Piroird, Guillaume Dupeux had never dropped at LadHyX; if neither Benjamin Vezon and Jules Simha had not been friends with Giorgio K.; if they had not been quite a usual at Roc14 and if it had not been for their company and good laugh; if, in 2010, the registration at Roc14 had been by random drawing of lots and if i had not met all those friendly faces at the club; if Audrey Lemarechal, Cécile Vigouroux, Sylvain Ferrari and Christine Ferrat at the École Polytechnique had not been helpful and patient with all the red tape; if the referees of the thesis, Alessandro Bottaro and Colm-cille Caulfield had suggested the graduate school to not allow me to defend my thesis publicly; if the other members of the jury, namely, François Gallaire, Jean-Christophe Robinet and Peter Schmid had graciously present at my thesis defense; (and i almost forgot) if the École Polytechnique could not have funded me for 3 years; and most importantly, if life had not been as kind as it had been, my thesis, well, in fact, nothing, absolutely nothing, would have ever been possible.

Thank you.
– Jon

To my beloved teachers ...

Abstract

Optimal growth mechanisms in wall-bounded shear flows, in particular, plane Couette and plane Poiseuille flow, with and without a destabilizing wall-normal temperature gradient are studied extensively. New insights on the transient growth mechanisms of arbitrary perturbations in both cases are obtained via the adjoint of the dominant eigenmode and the extension of Squire's transformation allowing us to propose universal scaling laws.

In the case with a cross-stream temperature gradient in a Boussinesq fluid, a comprehensive non-modal stability analysis is performed over various Reynolds, Rayleigh and Prandtl numbers. The scaling laws pertaining to transient growth in pure shear flows are shown to hold even in the presence of a destabilizing temperature gradient. This unstable temperature gradient only moderately increases the optimal growth. The lift-up effect remains the predominant transient growth mechanism. The classical inviscid lift-up mechanism characterizes the *short-time* behavior whereas the Rayleigh-Bénard eigenmode without its streamwise velocity component characterizes the *long-time* behavior. In this fashion, the entire optimal gain curve is fully retrieved and interpreted. Consequently, the role played by the Prandtl number as a parameter that couples temperature perturbations and the lift-up mechanism is understood. The results are shown to remain qualitatively similar over a general class of norms that can be considered as growth functions.

In the case of pure shear flows, the implications of the Squire transformation are extended to the (direct/adjoint) Squire equation and the entire eigenfunction structure of the Orr-Sommerfeld and Squire modes (direct/adjoint). The role of this extended-Squire transformation on the optimal transient growth of arbitrary 3D disturbances is thereby elucidated in the case of parallel shear flows bounded in the cross-stream direction. It also permits to demonstrate that the *long-time* optimal growth for perturbations of arbitrary wavenumbers may be decomposed as a product of the respective gains arising from the $2D$ Orr-mechanism and the lift-up mechanism. This asymptotic solution is shown to describe the *long-time* and even the *intermediate-time* dynamics of the optimal disturbances and provides a good estimate of the maximum optimal gain at all time.

Part I

Transient Growth in Rayleigh-Bénard-Poiseuille/Couette flows

Chapter 1

Introduction

> *"Yet not every solution of the equations of motion, even if it is exact, can actually occur in Nature. The flows that occur in Nature must not only obey the equations of fluid dynamics, but also be stable."*
>
> – L. D. Landau & E. M. Liftshitz (1959)

There are many examples in fluid flows wherein a very small action leads to the development of a series of complex spatio-temporal behaviors. Hence, for over a century now, hydrodynamic stability theory has been recognized as one of the important aspects of fluid mechanics. By the early twentieth century, various problems of hydrodynamic stability were recognized and formulated, thanks to Helmholtz [35], Lord Kelvin [48], Reynolds [73], Bénard [4], Orr [65], Lord Rayleigh [71], Taylor [81], etc. Osborne Reynolds [73] made one of the seminal contributions to the study of hydrodynamic stability. In his well-known pipe flow experiments [73], a *laminar flow*, the smooth flow which he recognized with a colored streak that extended in "a beautiful straight line" through the tube, was shown to breakdown when a non-dimensional parameter $U_{max}a/\nu^*$ (U_{max} being the maximum velocity of water in the tube, a radius of the tube, and ν^* the kinematic viscosity of the fluid at an appropriate temperature) exceeded a certain critical value. This non-dimensional parameter is now called the Reynolds number. He noted, "On viewing the tube by the light of an electric spark, the mass of color resolved itself into a mass of more or less distinct curls, showing eddies, .." and thus, introduced some of the most essential questions in modern hydrodynamic stability: (1) When do laminar flows break down? (2) What are the origins of such a breakdown? How are time-dependent flows realized for given steady boundary conditions? (3) What are the consequent developments of the breakdown, and do they eventually lead to turbulence?

More generally, it is in the differentiation between stable and unstable patterns of admissible flows that the problems of hydrodynamic stability originate. The Navier-Stokes equations admit a variety of steady solutions, the simplest being the so-called parallel shear flows: plane Couette flow, Hagen-Poiseuille flow (pipe flow), plane Poiseuille flow (plane channel flow), etc. These flow patterns are, however, not realized for various ranges of parameters that characterize them, for example, the Reynolds number in engineering applications, in nature, etc. It is reasonable to expect that such flow patterns are inherently unstable to small perturbations which are inevitably present in the physical systems and an instability could be regarded as the inability of a fluid flow to sustain against these perturbations. It is of fundamental interest in fluid dynamics to study such instabilities, in order to understand many common flow situations.

1.1 Basic concepts

1.1.1 Method of normal modes

The analysis in terms of normal modes to study the stability of dynamical system of particles and rigid bodies was already well-developed in Reynolds' time. Stokes, Kelvin and Rayleigh adapted the method of normal modes to fluid dynamics. In this method, a known steady solution of the equations of motion for the system is perturbed by infinitesimal disturbances and the equations are linearised by neglecting the products of the perturbations. It is further assumed that the perturbation of each quantity can be resolved into independent components or modes varying with time t like $e^{\lambda t}$ for some constant λ, which is in general complex. If the real part of λ is found to be positive for any mode, the system is deemed unstable because a general initial perturbation, however small, will grow exponentially until it is no longer small. In fluid dynamics, the motivation to analyze such linearized equations arises from the fact that the growth-rate of a finite amplitude disturbance can, at each instant of its evolution, be found from an infinitesimal disturbance with an identical shape. This is a consequence of the conservative nature of the nonlinear terms in the Navier-Stokes equations. Thus, the onset of any instability is always related to the mechanisms that are present in the linearized equations. A general solution to these equations can be sought in terms of independent modes varying exponentially in time. In the method of normal modes, one seeks such modes which would grow, or decay, exponentially in time. Mathematically, this is inferred from the spectrum of the linearized equations wherein the eigenvalues correspond to exponential growth rates and phase speed of the disturbance. The eigenfunctions represent the structure of the secondary flow at the onset of the instability.

In general, instability occurs because there is some perturbation of the equilibrium between external forces, inertia and internal stresses of a fluid. To understand some of the most basic physical mechanisms leading to instability in fluids it is important to remove inessential characteristics of the flow. It is conventional in physical sciences to consider a simple situation in which only one or a very few aspects of the flow are important. Thus, a few idealized flows have been the subject of extensive theoretical and experimental research for more than one hundred years. For example, Rayleigh-Bénard convection bounded by horizontal planes is a classic situation wherein instabilities arising from buoyancy forces can be analyzed; plane Poiseuille flow and plane Couette flow are one of the simplest flow configurations wherein shear flow instabilities can be studied.

The onset of thermal instability in horizontal layers of a fluid heated from below is well-suited to illustrate the many mathematical and physical facets of the general theory of hydrodynamic stability. It commonly arises when a fluid is heated from below: a horizontal layer of static fluid in which an adverse temperature gradient is maintained by heating the underside. The temperature thus maintained is called adverse since, on account of thermal expansion, the fluid at the bottom will be lighter than the fluid at the top; and this is a top-heavy arrangement whereby there is a tendency for the static fluid to redistribute itself and "fix the weakness" in its arrangement. This tendency of the fluid, however, will be inhibited by its own viscosity and thermal conductivity. In other words, if the temperature gradient is too small, heat will be transfered through

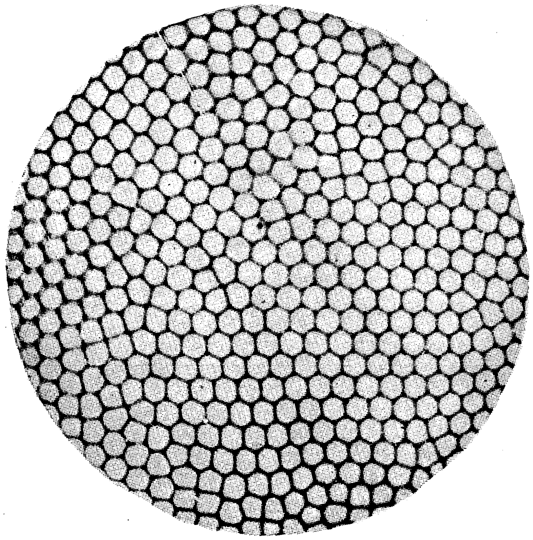

Figure 1.1: Bénard cells in spermaceti[10].

the fluid by conduction alone and it is expected that the adverse temperature gradient must exceed a certain value before the instability can manifest itself.

The first experiments on thermal convection date back to Count Rumford (1797), Thomson (1881) and Bénard (1900). The experiments by Bénard, in particular, have attracted great attention and are considered today as the first published results on thermal convection. This early interest is also due to the fascinating pattern of regular hexagonal cells (see figure 1.1) obtained for large time in his experiments. Stimulated by Bénard's experiments, Lord Rayleigh [71] wrote, "Bénard worked with very thin layers, ... the layer rapidly resolves itself into a number of cells, the motion being an ascension in the middle of a cell and a descension at the common boundary between a cell and its neighbours.. ...they acquire surfaces nearly identical, their forms being nearly regular convex polygons.... ..etc." Rayleigh chose equations of motion and boundary conditions to model the experiments. He assumed that the amplitude of the disturbances was infinitesimal so that the equations could be linearized. Rayleigh introduced the method of normal modes and showed that what determines the stability, or instability, of a layer of fluid heated from below is the value of the non-dimensional parameter $g\alpha^*\Delta T h^4/\kappa^*\nu^*$, which is the well-known Rayleigh number. Here, g is the acceleration due to gravity, α^* the thermal expansion coefficient of the fluid, ΔT the magnitude of the vertical temperature gradient across the fluid layer, h the height of the fluid layer, κ^* the fluid thermal conductivity and ν^* the fluid kinematic viscosity at a given temperature. In fact, Rayleigh derived the critical value of the Rayleigh number at which thermal instability would occur along with the wavenumber of the disturbance at the onset of thermal convection and the spatial structure of such disturbances.

The early success of the method of normal modes comes from the works of Kelvin [48], Helmholtz [35], Rayleigh [71] and Taylor [81] who derived criteria for the onset of instability in different flow situations. Indeed, the thermal convection problem is a special case where at the onset of instability *the principle of exchange of stability* is valid and a stationary pattern of motion prevails. The instability, thus, sets in as a steady

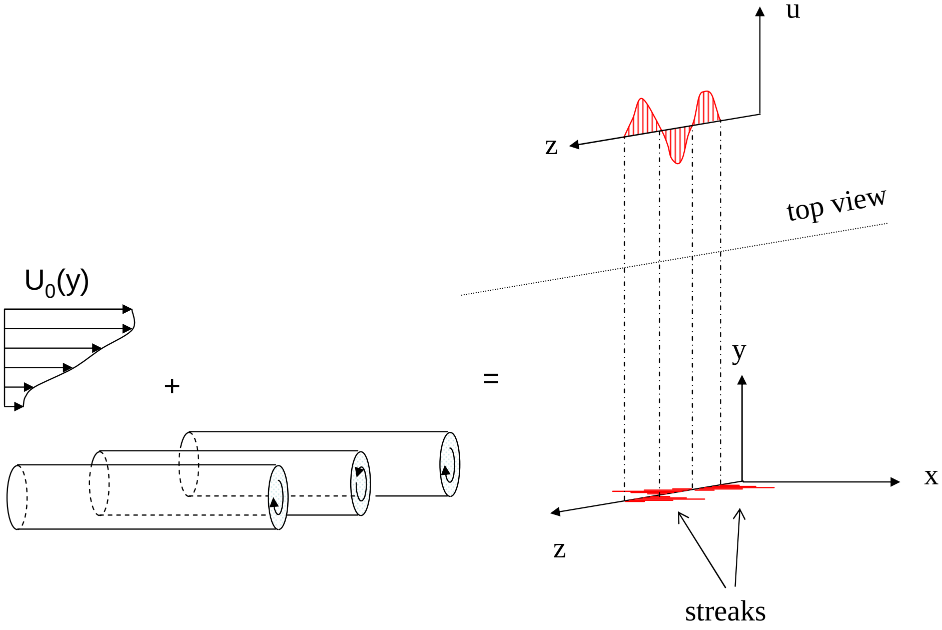

Figure 1.2: Schematic of the lift-up mechanism.

secondary flow. In the case of a static fluid heated from below, the secondary motion results from thermal convection. In contrast, if at the onset of instability oscillatory motion prevails, one has a case of *overstability*, a term coined by Eddington [**?**]. In such cases, a very small displacement from equilibrium provokes restoring forces so strong that the system "overshoots" on the other side of equilibrium.

1.1.2 Transient growth analysis

One of the biggest shortcomings of the modal stability analysis is that it fails to predict the onset of instability in some of the most common wall-bounded flows, for example, pipe flow, plane Couette flow, etc. This is mainly due to the fact that the spectrum of the linearized perturbation equations cannot completely describe the disturbance behavior at all times because it fails to capture their short-term characteristics [75]. In the case of parallel shear flows, the modal stability analysis predicts that two-dimensional spanwise-uniform disturbances provide the most dangerous asymptotic state at any given Reynolds number. Many experiments in the presence of high free-stream turbulence [50, 49, 60] show that transition is usually preceded by the presence of streamwise motion in the form of streaks and not via Tollmien-Schlichting waves as predicted by modal stability analysis. For example, a boundary layer which is subjected to free-stream turbulence levels in the range $1-6\%$ develops streamwise elongated regions of high and low streamwise velocity which lead to secondary instability and breakdown to turbulence [60]. In addition, it was commonly observed in experimental investigations [50, 49, 76] that a secondary flow is established on a substantially shorter time scale compared to that via Tollmien-Schlichting waves. It is, however, known that oblique disturbances, in particular streamwise-uniform disturbances, result in large perturbation kinetic energy at short times [21, 53]. In plane Poiseuille flow, the maximum non-dimensional growth rate

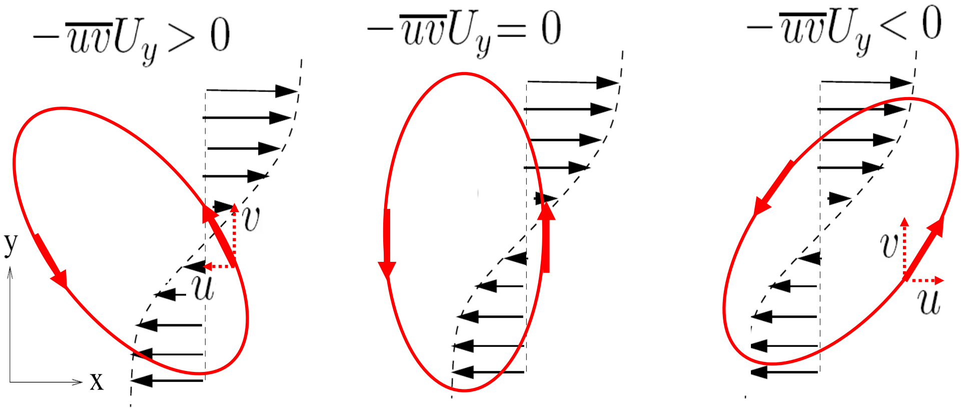

Figure 1.3: Schematic of the Orr mechanism [34].

based on half-width and centerline velocity is approximately 0.04 for two-dimensional spanwise-uniform disturbances and at this growth rate, it would take the mode about 57 time units to grow one order of magnitude. It was not until a few decades ago that the short-term perturbation dynamics and its consequences on transition to turbulence and scale selection at the onset of such transitions was considered seriously in hydrodynamic stability theory.

> *"..a finite disturbance independent of the streamwise coordinate may lead to instability of linear flow, even though the basic [flow] velocity does not possess any inflection point."*
>
> – T. Ellingsen & E. Palm (1975)

This was one of the earliest statements on the importance of transient growth of disturbances which may, however, be exponentially stable in the sense of modal stability analysis. Later, Landhal [53] showed that all parallel inviscid shear flows are unstable to a wide range of initial infinitesimal three-dimensional disturbances, in the sense that, according to the linear theory, the kinetic energy of the perturbations will grow at least as fast as linearly in time. He remarked that such a finding should have strong implications on the observed tendency of shear flows to develop streamwise streaky structures before leading to turbulence via Klebanoff modes [50] in the so-called by-pass transition route [62, 63]. In fact it was observed that in boundary layer flows with high free stream turbulence levels, the initial growth of streaky structures is related to such transient growth processes [60]. For flows such as plane Couette flow that do not support unstable normal modes, this transient growth must account for whatever increase of disturbance kinetic energy is observed, assuming that the initial disturbance is sufficiently small that nonlinear terms in the governing equations are negligible. For flows such as plane Poiseuille flow, that do support unstable normal modes, the onset of transition to turbulence is determined by the nature of initial perturbations [31]. The importance of the transient growth mechanisms in understanding how finite amplitude two-dimensional disturbances arise in shear flows was soon established [6, 72]. It was later shown that it is possible to tap the mean shear energy using certain perturbations, such as streamwise-uniform perturbations with non-zero wall normal velocity, that develop into the required primary disturbance on time scales comparable to those associated with the secondary instabilities even though the basic shear flow is stable or supports, at most, weak exponential instability [24, 6, 54, 75, 76].

This process of short-term increase in disturbance kinetic energy occurs in the absence of nonlinear effects. Mathematically, it can be explained by the non-normality of the governing linear operator [6, 72] i.e., the non-orthogonality of the associated eigenfunctions and it is not necessarily limited to degenerate eigenvalues [72]. Even though each eigenfunction may decay at its own rate (related to its eigenvalue), a superposition of non-orthogonal eigenfunctions may produce large transient growth before eventually decreasing at the rate of the least stable eigenfunction. Physically, the source of transient growth of disturbances is related to the inviscid vortex tilting process in the presence of base flow shear whereby a disturbance can feed on the base flow kinetic energy for a short time. The lift-up mechanism [6, 21, 53] and the Orr mechanism [65] are two such commonly identified growth phenomena in a shear flow. The former is considered as the dominant mechanism in many wall-bounded shear flows, for instance, the two-dimensional boundary layer. According to the lift-up mechanism, a very small streamwise-uniform vortex superimposed on a parallel shear flow can lift-up low-speed fluid from the wall and push down high-velocity fluid towards the wall (see figure 1.2). In the schematic shown in figure 1.2, x, y and z denote the streamwise, cross-stream and spanwise directions, $U_0(y)$ the base flow velocity and u the streamwise disturbance velocity. The sketch depicts an initial disturbance configuration in the form of streamwise vortices (x-component vorticity) which due to the presence of a base flow with non-zero cross-stream vorticity results in the production of streamwise perturbation velocity. In fact it is possible to show from the linearized perturbation equations that a streamwise-uniform vortex will continuously produce a u-velocity proportional to time t and base flow shear u_y via the lift-up mechanism until viscous dissipation becomes important at times of the order of Reynolds number Re [21, 53]. Hence, the growth in disturbance kinetic energy could be $\mathcal{O}(Re^2)$. The Orr-mechanism, is associated to the increase in disturbance kinetic energy due to an initial disturbance field that principally consists of spanwise-uniform vortices (z-component vorticity) that are tilted against the direction of the base flow as shown in figure 1.3. Such a disturbance can feed on the base flow kinetic energy via the Reynolds stress production term $\int -\overline{uv}U_y dy$. Here, $\overline{uv}$ is the average of the product of the streamwise velocity u and cross-stream velocity v (along y-direction) over an x-z plane at some height y and U_y is the base flow shear. This term is positive for an initial configuration as shown on the left of figure 1.3 and hence there is continuous production of disturbance kinetic energy until the base flow velocity $U(y)$ tilts this disturbance configuration to such an extent that viscous dissipation and Reynolds stress production terms become equal. Eventually, the perturbations start to lose their kinetic energy to the base flow as they are tilted indefinitely so as to align with the base flow vorticity (rightmost sketch of figure 1.3).

> *"To accurately describe disturbance behavior [in wall-bounded shear flows] at all times, it appears necessary to introduce a finite-time horizon over which an instability is observed."*
>
> – Peter J. Schmid (2007)

Thus, it is fundamental to the understanding of shear flow instabilities that one follows an analysis which determines the most amplified perturbations in such flows and, eventually, describes their evolution in time. The quantitative determination of the short-term disturbance dynamics is the goal of the so-called transient growth analysis. Many new concepts and techniques have been developed and successfully implemented during the last two decades to characterize such phenomena [75, 76].

1.2 Rayleigh-Bénard-Poiseuille/Couette flows

1.2.1 Motivation

It is clear that modal stability analysis offers good predictions for the onset of instability in Rayleigh-Bénard convection problem. It fails, however, in the case of many simple yet common wall-bounded shear flows, for example, plane Couette flow and plane Poiseuille flow. In the study of turbulent shear flows, plane Poiseuille flow and plane Couette flow are prototypes in which perturbations exhibit large transient growth in disturbance kinetic energy $\mathcal{O}(Re^2)$ via the mechanisms discussed earlier. It is reasonable to assume that the presence of a cross-stream temperature gradient in a parallel shear flow would influence transient growth. If so, what are the dominant physical mechanisms of transient growth in such flows? Is lift-up dominant at all Rayleigh and Prandtl numbers? *It is the aim of the present dissertation to examine thoroughly the influence of buoyancy induced by an adverse cross-stream temperature gradient on the transient growth phenomenon in plane Couette flow and plane Poiseuille flow.*

Indeed, there are simple stationary solutions to the Navier-Stokes equations for fluid motion between two infinitely long, rigid walls (moving/fixed) maintained at different temperatures (cold upper wall or vice versa) with no-slip boundary condition. If the temperature difference between the walls is small enough then conduction would be the only means of heat transfer and one expects a linear temperature variation between both walls to prevail. The base flow, under the assumption that the buoyancy force is the only temperature effect in the momentum equation, could be plane Poiseuille or plane Couette flow depending on whether the walls are stationary or moving relative to each other. Hereafter, the former is referred to as Rayleigh-Bénard-Poiseuille flow (RBP) and the latter is referred to as Rayleigh-Bénard-Couette flow (RBC). From an experimental as well as a theoretical point of view, the Rayleigh-Bénard convection problem is the simplest and most easily accessible case, in which the onset of instabilities can be readily studied. Plane Couette and plane Poiseuille flow represent prototype shear flows in which the onset of instabilities depends strongly on the initial conditions and hence, on the background disturbance field. Thus, the linear stability analysis of Rayleigh-Bénard-Poiseuille and Rayleigh-Bénard-Couette flows is expected to be of fundamental interest in hydrodynamic stability.

Moreover, this type of fluid motion is commonly encountered in various forms in geophysical flows, heat exchangers, electroplating, chemical vapor deposition, etc. Thermal convection in the presence of the atmospheric boundary layer that leads to the alignment of clouds in the lower atmosphere is a well-known example of thermal instability in the presence of a shear flow [52]. The study of such flows is useful in fields often remote from fluid dynamics such as plankton research. For example, the motion and spatial distribution of phytoplankton and algal suspensions are affected by convection in the presence of shear flows in ice-covered lakes [46, 14]. It is not surprising that shear flows involving thermal convection are fundamental to flow situations arising in astrophysics, meteorology, and many engineering applications.

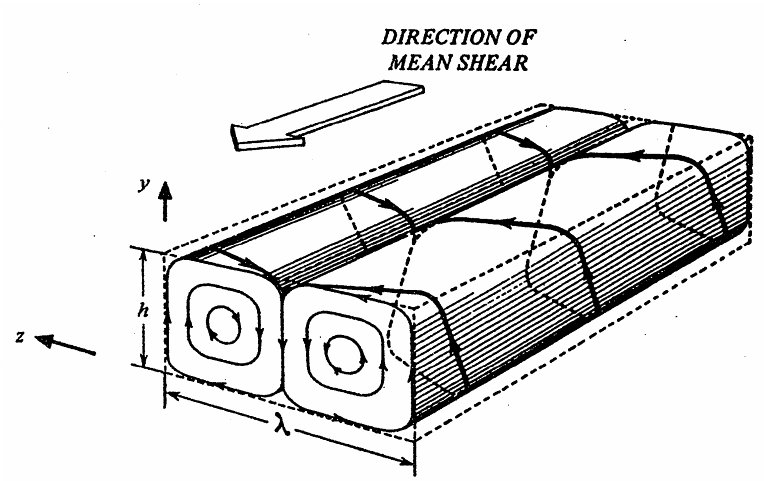

Figure 1.4: Schematic of "longitudinal" rolls as observed by Bénard and Avsec (1938)

1.2.2 A brief history of *RBP* and *RBC* flows: Modal stability

The thermal instability leading to secondary motion in the form of Rayleigh-Bénard convection rolls has been well-known for more than a century. If the domain is large enough compared to the depth of the fluid layer, the convection rolls do not have a preferential orientation. In the presence of a shear flow, however, modal stability theory predicts that streamwise-uniform convection rolls would occur. In fact, the preference for streamwise-uniform convection rolls (called longitudinal rolls in the literature) in unstably stratified (adverse temperature gradient) shear flows was first discovered by Idrac [41]. It is interesting to note that Idrac was interested mainly in possible atmospheric applications, including migration patterns of birds from Europe to Africa. The phenomenon, however, has long since intrigued a number of researchers. In the case of a static fluid heated from below, convection develops in the form of locally two-dimensional rolls. If allowed to develop in a sufficiently large aspect ratio apparatus and from background disturbances instead of controlled initial disturbances, rolls can have a random orientation. Thus, in Idrac's experiments, the emergence of a well-ordered motion from a seemingly random state is fascinating to say the least. Terada [42] made quantitative observations of these rolls in shear flows. For example, he noted that, for small values of the gap height h, the wavelength of the rolls was about $2h$. Later, the linear stability analysis of *RBP* and *RBC* flows was motivated by the observation of cloud streets [2, 3, 52] and sand dunes in deserts [33]. The convection rolls in the lower atmosphere tend to align in the direction of the atmospheric boundary layer. The moisture in the up-flowing warm air of these rolls condenses to form clouds that are aligned in the streamwise direction, thereby leading to the formation of cloud streets [52] (see figure 1.6). It was not until Chandra in 1938 [9] that experimentalists claimed that shear does not affect the critical Rayleigh number for plane Couette flow. However, definitive evidence was not available until Ingersoll [43] showed via heat flux measurements that this is true. Ingersoll [43] used two horizontal concentric discs with fluid contained between them. Such a set-up allows for reduced end effects. The upper disc is rotated at a constant angular velocity

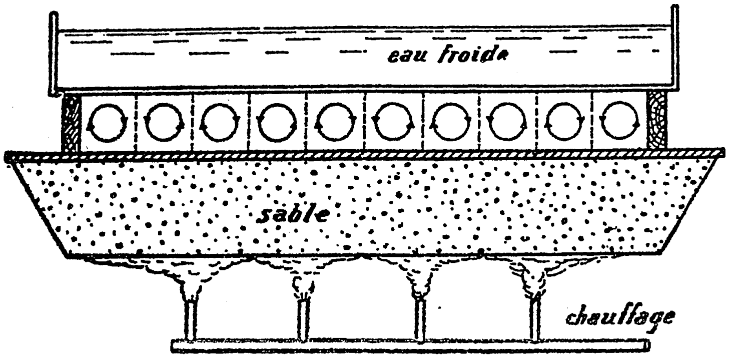

Figure 1.5: Sketch of Idrac's experiment (1920). It accounts for the first published result of "longitudinal" convection rolls.

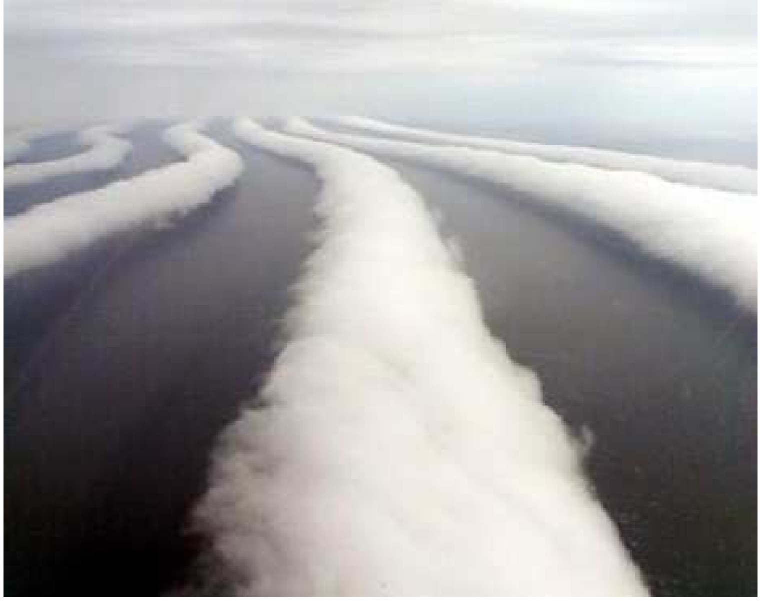

Figure 1.6: Cloud-streets as formed due to the presence of convection rolls aligned along the shear of the atmospheric boundary layers [79]. This photograph was taken from a Japan Coast Guard aircraft off the north-eastern coast of Hokkaido. It shows a bird's-eye view of cloud streets over the Sea of Okhotsk. According to the source [59], these clouds floated just over the sea surface, stood 300 meters tall and stretched for over 100 kilometers.

while the lower disc is kept at rest. The gap between the discs is maintained small. The results from Ingersoll's experiments are displayed in figure 1.7. It shows Nusselt number Nu which is the ratio of heat transports with and without convection as a function of Rayleigh number for various Reynolds numbers. The Reynolds numbers (evaluated at the outer radius) are denoted by various symbols. Since the symbols collapse on a single curve, it is concluded that the critical Rayleigh number of thermal convection in Couette flow is independent of Reynolds number. For the sake of completeness, it is here mentioned that Akiyama, Hwang and Cheng [1] determined experimentally that the longitudinal rolls form near the Rayleigh number $Ra = 1708$ (based on the channel width) for the case of fully developed, plane Poiseuille flow. This experimental result is close to the theoretical value $Ra_c^{RB} = 1707.78$. In fact Akiyama *et. al.* [1] observed weak convection in the form of rolls for $Ra < 1708$ and non-zero Reynolds numbers $Re > 0$. It was, however, attributed to the subcritical instability arising from non-Boussinesq effects.

Thus, the experimental results predominantly indicate that longitudinal rolls occur at a fixed Rayleigh number, independent of Reynolds number, and that the onset of secondary motion occurs via streamwise convective motion. However, in order to demonstrate that spanwise-uniform rolls are more stable than streamwise-uniform rolls, the linearized equations should be solved subject to appropriate boundary conditions. The earliest known stability analysis of plane Poiseuille flow with unstable thermal stratification in a Boussinesq fluid is due to Gage and Reid [26]. If $Re_c^{TS}(\approx 5772.2)$ is the Reynolds number (based on the channel half-width) at which Tollmien-Schlichting waves (TS) become unstable in plane Poiseuille flow without temperature effects, Gage and Reid showed that for all Reynolds numbers less than a critical value, approximately equal to Re_c^{TS}, the dominant eigenmode of RBP is in the form of streamwise-uniform convection rolls due to the Rayleigh-Bénard instability (RBI) above a critical Rayleigh number $Ra_c^{RB} = 1707.78$ (based on the channel width). This value is independent of both Reynolds number and Prandtl number. It was concluded that the effect of a shear flow on the linear stability of a fluid subjected to unstable cross-stream temperature gradient is only to align the rolls along the streamwise direction. Furthermore, the effect of the cross-stream temperature gradient on the Tollmien-Schlichting instability (TSI) is negligible for all $Ra < Ra_c^{RB}$: the critical Reynolds number for the onset of TS waves in RBP remains very close to $Re_c^{TS} \approx 5772.2$.

The complete linear stability characteristics of plane Couette flow with unstable thermal stratification in a Boussinesq fluid (RBC) were first computed by Gallagher and Mercer [27]. As in RBP flow, the dominant eigenmode at all Reynolds numbers is in the form of streamwise-uniform convection rolls due to RBI.

The energy method [77] has been used to obtain bounds on the Rayleigh and Reynolds numbers below which the flow is stable to disturbances of arbitrary amplitude (i.e., the flow is globally stable). It is to be noted, however, that such bounds can be obtained only via defining an appropriate "energy" for the system. This is a subject of debate in shear flows with adverse cross-stream temperature gradient and we simply postpone the discussion until chapter 4 (section 4.1.1). For the case of plane Couette flow, it was shown by Joseph [44] that if

$$Ra + \frac{1}{4}Re^2 < 1708, \tag{1.1}$$

any infinitesimal disturbance decays monotonically with time. Here, the Reynolds number Re is based on the half-channel width and the wall velocity for the case when the

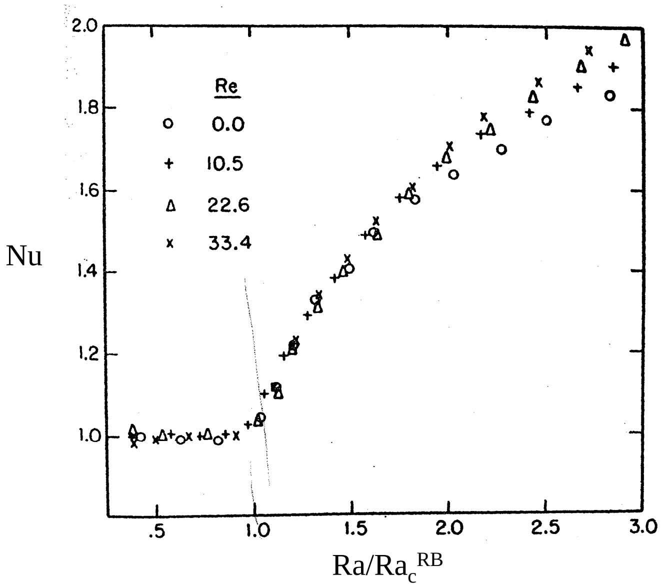

Figure 1.7: Rotating disk experiments from Ingersoll [43]: Nusselt number as a function of Rayleigh number for various Reynolds numbers.

rigid walls are moving at equal speed in opposite directions. Equation (1.1) implies that time-dependent subcritical instabilities do no exist in this domain of control parameters. In addition, it was demonstrated by Joseph [44] that the "most dangerous" disturbance, (i.e., the disturbance yielding the lowest "energy" bound for various Reynolds number) has the form of a longitudinal roll disturbance. It is to be mentioned, however, that these results are based on calculations wherein only kinematically admissible disturbances are considered.

Clever, Busse and Kelly [13] studied the secondary instability of the streamwise-uniform rolls in *RBC* in an effort to understand the onset of waviness in the rolls and to relate them to the formation of cloud streets in the lower atmosphere. The secondary instabilities of the convection rolls were determined to occur as standing waves or simply as waves that propagate along the rolls. Clever and Busse [11] later considered the three-dimensional flows arising from the secondary instability: they computed the finite-amplitude solutions that evolve from the wavy instability, even at vanishing or negative values of the Rayleigh number. The interested reader is referred to Kelly [47] for a comprehensive review of the major results on the onset and development of thermal convection in *RBP*.

1.2.3 A brief history of *RBP* and *RBC* flows: Non-modal stability

For the last two decades, non-modal stability analysis has been an active area of research in hydrodynamic stability and it has been recognized as fundamental to the understanding of shear flow instabilities. Many new concepts and techniques have been developed and successfully employed in various flows [76]. Recently, there had been an increased interest in the Rayleigh-Bénard-Poiseuille/Couette system as a prototype problem for transient growth mechanisms related to buoyancy forces [5, 74, 55], absolute and convective instabilities involving two propagation directions [7, 66, 29], three-dimensional global modes [8, 57, 56, 58], etc. The system has so far motivated many researchers in flow instabilities because of its simplicity and fascinating properties.

Biau and Bottaro [5] investigated the effect of *stable* thermal stratification, solely induced by buoyancy, on the spatial transient growth of energy in RBP flow. The analysis showed that the presence of stable stratification reduces the optimal transient growth of perturbations. Perhaps the most akin to this thesis is the article by Sameen and Govindarajan [74] who studied the effect of heat addition on the transient growth and secondary instability in plane channel flow. According to their study, the effect of heating may be split into three contributions: the first one is due to the generation of buoyancy forces as in classical Rayleigh-Bénard convection, the second one is associated with the temperature-dependent base flow viscosity, and the third one results from viscosity variations induced by temperature perturbations. The computations revealed that heat addition gives rise to very large optimal growth. For various control parameter settings, it was demonstrated that viscosity stratification had a very small effect on transient growth. At moderately large Reynolds number (= 1000), the optimal disturbances could be either streamwise-uniform vortices (as in pure shear flows) or spanwise-uniform vortices, largely depending on Prandtl number and Grashof number. However, the transient growth mechanisms related to such optimal initial disturbances, and their corresponding response were not examined. Finally, cross-stream viscosity stratification was determined to have a destabilizing influence on the secondary instability of TS waves.

A comprehensive study of the transient growth in plane Couette flow with cross-stream temperature gradient was performed by Malik, Dey and Alam[55] in the context of a *compressible* fluid. The optimal energy growth was determined to be strongly impaired by the presence of viscosity stratification in such flows.

1.3 Objective

In light of the previous works and in view of the fundamental nature of the phenomena under consideration, *the objective of the present investigation is to provide a comprehensive understanding of the effect of buoyancy alone on the transient growth in RBP and RBC flows.* Since viscosity stratification was observed to be ineffective for transient growth in RBP (Sameen and Govindarajan[74]), this effect will not be taken into account. Thus, the RBP and RBC flows under consideration form the simplest systems where the effect of buoyancy forces on shear flow instabilities can be studied. A thorough treatment of the non-modal growth in RBP and RBC flows will be given, as a function of the main control parameters, namely, the Reynolds number, Rayleigh number and Prandtl number.

This part of the thesis has been organized in the following way. Chapter 2 describes the base flow configuration and formulates the governing equations and basic concepts of both modal and non-modal stability analyses. Chapter 3 reviews and presents the modal stability characteristics of the various exponentially-growing eigenmodes. In chapter 4, major results from the non-modal stability analysis are discussed. The dominant transient growth processes are determined. The issues pertaining to the choice of the norm and to the effect of Prandtl number are also included in the same chapter.

Chapter 2

Linear stability analysis of *RBP* and *RBC* flows

"You will have to brace yourselves for this – not because it is difficult to understand, but because it is absolutely ridiculous: All we do is draw little arrows on a piece of paper – thats all"

– Richard Feynman
QED : The Strange Theory of Light and Matter (1985).

The basic concepts and equations dealt with in part I of the thesis are introduced in this chapter. The base flow configuration is discussed in section 2.1. The governing equations of infinitesimal perturbations in Rayleigh-Bénard-Poiseuille/Couette flows are derived for two different types of non-dimensionalization in section 2.2. The implication of such non-dimensinalizations are mentioned. The adjoint equations do not play a part in the modal stability analysis. However, they are derived in this chapter just for the sake of completeness.

2.1 Base flow

The base flows under study are shown in figure 2.1: plane Poiseuille flow (or plane Couette flow) in the presence of a cross-stream temperature gradient, namely, Rayleigh-Bénard-Poiseuille (or Rayleigh-Bénard-Couette) flow. If x and z are the non-dimensional streamwise and spanwise coordinates, such base flow velocity and temperature profiles are uniform along these directions and depend only on the wall-normal spatial coordinate y. Let h be the width of the channel. Then the non-dimensional velocity $U_0(y)$ and temperature $\Theta_0(y)$ profiles of RBP and RBC flows are

$$U_0(y) \quad = \begin{cases} 1 - y^2, & \text{plane Poiseuille flow} \\ y, & \text{plane Couette flow} \end{cases}, \tag{2.1}$$

$$\Theta_0(y) \quad = \Theta^* - y, \tag{2.2}$$

where y is normalized with the half-width of the channel $\frac{h}{2}$, velocity profiles have been normalized with respect to the maximum velocity of the base flow U_{max}, the temperature

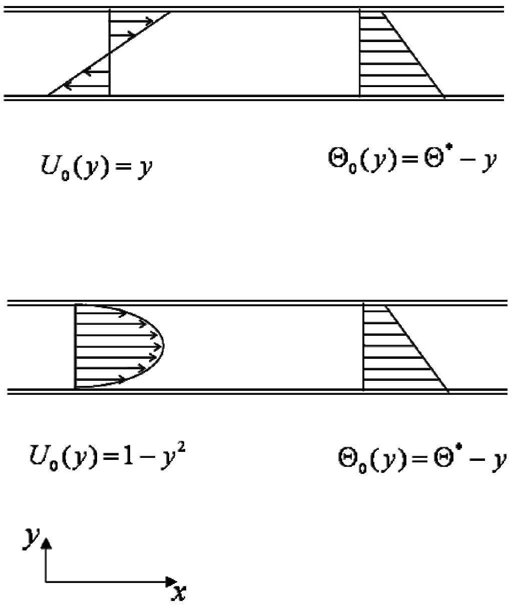

Figure 2.1: Schematic view of Rayleigh-Bénard-Couette (top) and Rayleigh-Bénard-Poiseuille (bottom) flows.

of the base flow has been normalized with $\frac{\Delta T}{2}$ and Θ^* is the average non-dimensional temperature of the channel.

Note that these profiles are solutions of the Navier-Stokes equations under the Boussinesq approximation: (1) all fluid physical properties, except density, are considered independent of pressure and temperature (Implicitly, it is assumed that the pressure and temperature variations are small and that the corresponding variations in fluid physical properties are negligible); (2) the density of the fluid is assumed to be related to temperature variations only (and considered to be independent of pressure variations) through an equation of state of the form $\rho = \rho^* \left[1 - \alpha^*(\Theta - \Theta^*)\right]$, where $\rho*$ and α^* are temperature-and-pressure-independent fluid density and thermal expansion coefficient, respectively; (3) and most importantly, the density variations are assumed to be negligible in every term of the equations of motion, except in the buoyancy term.

2.2 Governing Equations

A brief discussion of the governing equations for perturbations to this base flow is presented here. In general, there are two formal ways of normalizing the velocity components. Their implications are discussed in this section. One could go from one scaling to the other, as done in the following chapters, to extract interesting physics.

The non-dimensional control parameters of the problem, namely, Reynolds number, Rayleigh number and Prandtl number, are defined as follows:

$$Re = \frac{U_{max}\frac{h}{2}}{\nu^*}, \quad Ra = \frac{\alpha^* g \Delta T h^3}{\nu^* \kappa^*}, \quad Pr = \frac{\nu^*}{\kappa^*}, \tag{2.3}$$

where U_{max} is the maximum base flow velocity, h the height of the channel, ν^* is the kinematic viscosity, α^* is the thermal expansion coefficient of the fluid, g is the acceleration due to gravity, ΔT is the difference in temperature between the lower and upper wall and κ^* is the thermal diffusion coefficient.

The governing equations of the disturbance field in RBP and RBC flows can be obtained by linearizing the Oberbeck-Boussinesq equations about the respective base flow and temperature profiles. If $\vec{u}(\vec{x},t) = [u,v,w]^T$ and $\theta(\vec{x},t)$ are the disturbance velocity and temperature field, respectively, they read

$$\nabla \cdot \vec{u} \quad = 0, \tag{2.4}$$

$$\left(\frac{\partial}{\partial t} + RePrU_0\frac{\partial}{\partial x}\right)\vec{u} + RePrv\frac{dU_0}{dy}\vec{e}_x = -\nabla p + Pr\nabla^2\vec{u} + Ra_{h/2}Pr\theta\vec{e}_y, \tag{2.5}$$

$$\left(\frac{\partial}{\partial t} + RePrU_0\frac{\partial}{\partial x}\right)\theta + v\frac{d\Theta_0}{dy} \quad = \nabla^2\theta, \tag{2.6}$$

where, $Ra_{h/2} = Ra/16$ is the Rayleigh number based on the half-width of the channel. In equations (2.4)-(2.6), the thermal diffusive time scale $\frac{(h/2)^2}{\kappa^*}$ has been chosen to non-dimensionalize time, $\vec{u}(\vec{x},t)$ has been scaled with respect to $(\frac{\kappa^*}{h/2})$ while the base flow velocity $U_0(y)$ has been scaled with respect to U_{max}. The pressure p is scaled with the dynamic pressure $\frac{1}{2}\rho(\frac{\kappa^*}{h/2})^2$. These equations are to be solved with homogeneous Dirichlet boundary conditions on $\vec{u}(\vec{x},t)$ and $\theta(\vec{x},t)$ at $y = \pm 1$ [1]

The base flow is homogeneous in x and z, and hence the perturbation field may be decomposed into independent wave modes,

$$\vec{u}(\vec{x},t) = \vec{\tilde{u}}(y,t)e^{i(\alpha x+\beta z)} \ + \ c.c., \tag{2.7}$$

$$\theta(\vec{x},t) = \tilde{\theta}(y,t)e^{i(\alpha x+\beta z)} \ + \ c.c., \tag{2.8}$$

$$p(\vec{x},t) = \tilde{p}(y,t)e^{i(\alpha x+\beta z)} \ + \ c.c.,. \tag{2.9}$$

where α, β are the streamwise and spanwise wavenumber, respectively and *c.c.* stands for the complex conjugate of the preceding expression. The perturbation equations (2.4)-(2.6) then read:

$$i\alpha\tilde{u} + \frac{\partial\tilde{v}}{\partial y} + i\beta\tilde{w} = 0, \tag{2.10}$$

$$\left(\frac{\partial}{\partial t} + i\alpha RePrU_0\right)\tilde{u} + RePr\tilde{v}\frac{dU_0}{dy} = -i\alpha\tilde{p} + Pr\left(\frac{\partial^2}{\partial y^2} - k^2\right)\tilde{u}, \tag{2.11}$$

$$\left(\frac{\partial}{\partial t} + i\alpha RePrU_0\right)\tilde{v} = -\frac{\partial\tilde{p}}{\partial y} + Ra_{h/2}Pr\tilde{\theta} + Pr\left(\frac{\partial^2}{\partial y^2} - k^2\right)\tilde{v}, \tag{2.12}$$

$$\left(\frac{\partial}{\partial t} + i\alpha RePrU_0\right)\tilde{w} = -i\beta\tilde{p} + Pr\left(\frac{\partial^2}{\partial y^2} - k^2\right)\tilde{w}, \tag{2.13}$$

---

[1] Note that * on physical properties, fluid dynamical and physical variables, like kinematic viscosity, thermal expansion, velocity etc. denote temperature-independent quantities, unless otherwise stated.

$$\left(\frac{\partial}{\partial t} + i\alpha RePrU_0\right)\tilde{\theta} + \tilde{v}\frac{d\Theta_0}{dy} = \left(\frac{\partial^2}{\partial y^2} - k^2\right)\tilde{\theta}, \tag{2.14}$$

where $k^2 = \alpha^2 + \beta^2$ and the boundary conditions are $\vec{\tilde{u}}(\pm 1) = 0$ and $\tilde{\theta}(\pm 1) = 0$. If the advective time scale $\frac{h/2}{U_{max}}$ and velocity scale U_{max} are used instead of the thermal diffusive time scale $\frac{(h/2)^2}{\kappa^*}$ and velocity scale $\frac{\kappa^*}{h/2}$, these equations become

$$i\alpha\breve{u} + \frac{\partial\breve{v}}{\partial y} + i\beta\breve{w} = 0, \tag{2.15}$$

$$\left(\frac{\partial}{\partial t_{Re}} + i\alpha U_0\right)\breve{u} + \breve{v}\frac{dU_0}{dy} = -i\alpha\breve{p} + \frac{1}{Re}\left(\frac{\partial^2}{\partial y^2} - k^2\right)\breve{u}, \tag{2.16}$$

$$\left(\frac{\partial}{\partial t_{Re}} + i\alpha U_0\right)\breve{v} = -\frac{\partial\breve{p}}{\partial y} + \frac{Gr}{Re^2}\tilde{\theta} + \frac{1}{Re}\left(\frac{\partial^2}{\partial y^2} - k^2\right)\breve{v}, \tag{2.17}$$

$$\left(\frac{\partial}{\partial t_{Re}} + i\alpha U_0\right)\breve{w} = -i\beta\breve{p} + \frac{1}{Re}\left(\frac{\partial^2}{\partial y^2} - k^2\right)\breve{w}, \tag{2.18}$$

$$\left(\frac{\partial}{\partial t_{Re}} + i\alpha U_0\right)\tilde{\theta} + \breve{v}\frac{d\Theta_0}{dy} = \frac{1}{RePr}\left(\frac{\partial^2}{\partial y^2} - k^2\right)\tilde{\theta}, \tag{2.19}$$

where $Gr = Ra_{h/2}/Pr$ is the Grashof number, t_{Re} is the advective time scale $\frac{h/2}{U_{max}}$, $\vec{\breve{u}}$ and $\breve{p}$ are the new non-dimensional wall-normal velocity vector and scalar pressure. They are related to t, $\vec{\tilde{u}}$ and $\tilde{p}$ as

$$t_{Re} = t(RePr), \tag{2.20}$$

$$\vec{\breve{u}} = \vec{\tilde{u}}\left(\frac{1}{RePr}\right), \tag{2.21}$$

$$\breve{p} = \tilde{p}\left(\frac{1}{RePr}\right)^2. \tag{2.22}$$

The state variables obey homogeneous Dirichlet boundary conditions.

The systems (2.10)-(2.14) and (2.15)-(2.19) are the same but for the non-dimensionalization of velocity, pressure and temperature variables. This is due to the presence of two independent time scales in the base flow: (1) the base flow velocity that provides the advective time scale and (2) thermal conduction due to the presence of a cross-stream temperature gradient that provides the thermal diffusion time scale. Equations (2.10)-(2.14) and (2.15)-(2.19) are similar to the linearized Oberbeck-Boussinesq equations except for the terms involving $U_0(y)$ and are equivalent to the linearized Navier-Stokes equations except for the linear temperature equation and the buoyancy term due to $\tilde{\theta}$ in (2.12) and (2.17). At $Re = 0$, the former system (2.10)-(2.14) smoothly reduces to the set of disturbance equations of the pure conduction problem (a static fluid layer subjected to a temperature gradient in the wall-normal direction) whereas the latter system (2.15)-(2.19) is singular in this limit. When $Ra = 0$, however, both formulations reduce to the linearized Navier-Stokes equations about a parallel shear flow. The Squire transformation [80] (see section 2.3) is readily inferred from the former system whereas it is not directly evident from the latter system. When $Re >> 1$ the latter formulation is more meaningful and, as shown in chapter 4, useful scaling laws can be derived based on this normalization. For convenience, only the former normalization and equations (2.10)-(2.14) are considered in the following chapters, unless otherwise mentioned.

Note that both formulations do not assume exponential behavior in time for the state variables. The so-called modal temporal problem, however, considers disturbances that grow or decay exponentially. It is legitimate to look for such solutions because the coefficients in the linear operator (2.10)-(2.14) are independent of time t. The success of the modal analysis depends on finding a complete set of exponentially decaying (or growing) solutions, namely, normal modes, to represent the development of an arbitrary initial disturbance. If the variables $\tilde{\vec{u}}(y,t)$ and $\tilde{\theta}(y,t)$ in equations (2.7) and (2.8) are taken as

$$\tilde{\vec{u}}(y,t) \quad = \hat{\vec{u}}(y)e^{-i\omega t}, \tag{2.23}$$

$$\tilde{\theta}(y,t) \quad = \hat{\theta}(y)e^{-i\omega t}, \tag{2.24}$$

$$\tilde{p}(y,t) \quad = \hat{p}(y)e^{-i\omega t}, \tag{2.25}$$

the system (2.10)-(2.14), along with the boundary conditions, defines a generalized eigenvalue problem for the complex frequency ω at given (α, β), Re, Ra and Pr. Following the classical parallel shear flow analysis, equations (2.10)-(2.14) may be rewritten in terms of reduced variables, namely, the wall-normal velocity $\hat{v}(y)$, wall-normal vorticity $\hat{\eta}(y)$ and temperature perturbations $\hat{\theta}(y)$, leading to the system

$$\begin{aligned}\left[(-i\omega + i\alpha RePrU_0)\left(D^2 - k^2\right) - i\alpha RePr\frac{d^2U_0}{dy^2}\right]\hat{v} = Pr\left(D^2 - k^2\right)^2\hat{v} \\ -k^2 Ra_{h/2}Pr\hat{\theta},\end{aligned} \tag{2.26}$$

$$(-i\omega + i\alpha RePrU_0)\,\hat{\eta} + i\beta RePr\frac{dU_0}{dy}\hat{v} = Pr\left(D^2 - k^2\right)\hat{\eta}, \tag{2.27}$$

$$(-i\omega + i\alpha RePrU_0)\,\hat{\theta} + \frac{d\Theta_0}{dy}\hat{v} = \left(D^2 - k^2\right)\hat{\theta}, \tag{2.28}$$

where $D = \frac{d}{dy}$ and the boundary conditions are $\hat{v}(\pm 1) = 0$, $D\hat{v}(\pm 1) = 0$, $\hat{\eta}(\pm 1) = 0$ and $\hat{\theta}(\pm 1) = 0$. Equation (2.26) is the Orr-Sommerfeld equation forced by buoyancy. The classical Squire equation (2.27) is simply retained for shear flows in Boussinesq fluids because buoyancy acts normal to the wall and it cannot directly induce wall-normal vorticity. Equation (2.28) is the linearised temperature equation which is of an advection-diffusion nature similar to the one in the linear stability of pure conduction in Boussinesq fluids.

2.3 Squire's transformation

It is shown in this section that the problem defined by the system (2.10)-(2.14) for any arbitrary perturbation with $\alpha \neq 0$, $\beta \neq 0$ (say, an oblique mode), is equivalent to that for a spanwise-uniform mode ($\beta_{2D} = 0$) at a different Reynolds number.

Consider equations (2.10)-(2.14) for a normal mode at α_{2D}, $\beta_{2D} = 0$ and Reynolds number Re_{2D}

$$i\alpha_{2D}\tilde{u}_{2D} + \frac{\partial \tilde{v}}{\partial y} = 0, \tag{2.29}$$

$$\left(\frac{\partial}{\partial t} + i\alpha_{2D} Re_{2D} Pr U_0\right)\tilde{u}_{2D} + Re_{2D} Pr \tilde{v}\frac{dU_0}{dy} = -i\alpha_{2D}\tilde{p} + Pr\left(\frac{\partial^2}{\partial y^2} - \alpha_{2D}^2\right)\tilde{u}_{2D} \tag{2.30}$$

$$\left(\frac{\partial}{\partial t} + i\alpha_{2D} Re_{2D} Pr U_0\right)\tilde{v} = -\frac{\partial \tilde{p}}{\partial y} + Ra_{h/2} Pr \tilde{\theta} + Pr\left(\frac{\partial^2}{\partial y^2} - \alpha_{2D}^2\right)\tilde{v}, \tag{2.31}$$

$$\left(\frac{\partial}{\partial t} + i\alpha_{2D} Re_{2D} Pr U_0\right)\tilde{\theta} + \tilde{v}\frac{d\Theta_0}{dy} = \left(\frac{\partial^2}{\partial y^2} - \alpha_{2D}^2\right)\tilde{\theta}, \tag{2.32}$$

where the subscripts $2D$ refer to variables of the spanwise-uniform Fourier mode $\vec{\tilde{u}}_{2D}(y,t) = [\tilde{u}_{2D}, \tilde{v}, 0]^T$ and $\tilde{\theta}(y,t)$. By comparing this system with equations (2.10)-(2.14) for any $\alpha \neq 0$, $\beta \neq 0$, we note that they have the same solutions if

$$i\alpha_{2D}\tilde{u}_{2D} \quad = i\alpha\tilde{u} + i\beta\tilde{w}, \tag{2.33}$$

$$\alpha_{2D} \quad = \sqrt{\alpha^2 + \beta^2}, \tag{2.34}$$

$$\alpha_{2D} Re_{2D} \quad = \alpha Re. \tag{2.35}$$

Note that $Re_{2D} < Re$ and hence, *at a fixed Ra and Pr, for every three-dimensional Fourier mode in RBP and RBC flow, there exists a two-dimensional Fourier mode ($\beta = 0$), at a smaller Reynolds number* given by the transformation (2.33)-(2.35). This transformation is similar to the Squire transformation in pure shear flows[80]. Note, however, that the time variable t remains invariant under the transformation. This result has similar implications regarding on the linear stability analysis of *RBP* and *RBC* flows as discussed in chapter 3.

2.4 Adjoint equations and the norm

The adjoint of the linear operator (2.26)-(2.28) is now derived. Consider the family of norms that represent a measure of the growth of perturbations,

$$E\left(t;\gamma\right) = \int_{\mathtt{V}} \left[\frac{1}{2}\left(|u|^2 + |v|^2 + |w|^2\right) + \frac{1}{2}\gamma^2 |\theta|^2\right] d\mathtt{V}, \tag{2.36}$$

where the weight γ between the kinetic energy and the temperature perturbations is left arbitrary. Note that $E\left(t;\gamma\right)$ belongs to a class of norms commonly used in the literature; in particular, in [74] and [5], $\gamma = 1$ and $\gamma = \sqrt{\left|Ra_{h/2}\right| Pr}$, respectively. For a discussion on the choice of the norm the reader is referred section 4.1.1. It is convenient to rewrite the state vector as $\boldsymbol{q} = \left[\tilde{v}, \tilde{\theta}_*, \tilde{\eta}\right]^T$, where $\tilde{\theta}_* = \gamma\tilde{\theta}$. The direct equations (2.26)-(2.28) can then be written in the matrix form

$$\left(\mathbf{L}_{OB} + \frac{\partial}{\partial t}\mathbf{B}_{OB}\right)\boldsymbol{q} = 0, \tag{2.37}$$

where

$$\begin{aligned}
\mathbf{L}_{OB} &= \begin{bmatrix} Pr.L_{OS} & -k^2\frac{Ra_{h/2}Pr}{\gamma} & 0 \\ -\gamma\left(-\frac{d\Theta_0}{dy}\right) & L_{LHE} & 0 \\ i\beta\left(RePr\right)\frac{dU_0}{dy} & 0 & Pr.L_{SQ} \end{bmatrix}, \\
\mathbf{B}_{OB} &= \begin{bmatrix} k^2 - D^2 & 0 & 0 \\ 0 & 1 & 0 \\ 0 & 0 & 1 \end{bmatrix}.
\end{aligned}$$

The Orr-Sommerfeld and Squire operators, L_{OS} and L_{SQ}, respectively, are defined as

$$\begin{aligned}
L_{OS} = i\alpha ReU_0\left(k^2 - D^2\right) + i\alpha Re\frac{d^2U_0}{dy^2} \\
+ \left(k^2 - D^2\right)^2,
\end{aligned} \tag{2.38}$$

$$L_{SQ} = i\alpha ReU_0 + \left(k^2 - D^2\right), \tag{2.39}$$

and L_{LHE} (here, the subscript LHE refers to Linearized Heat Equation) is the advection-diffusion operator governing the evolution of the rescaled temperature perturbation:

$$L_{LHE} = i\alpha RePrU_0 + \left(k^2 - D^2\right). \tag{2.40}$$

Homogeneous boundary conditions on the state vector $\boldsymbol{q}$ are enforced, as for the reduced variables in (2.26), (2.27) & (2.28). In the case of unstable thermal stratification $\frac{d\Theta_0}{dy} = -1$ and for stable stratification $\frac{d\Theta_0}{dy} = 1$. The adjoint of the linear operator, say $\mathbf{L}_{OB}^A$, is defined as

$$\langle\langle\mathbf{L}_{OB}\boldsymbol{q},\ \boldsymbol{q}_A\rangle\rangle = \langle\langle\boldsymbol{q},\ \mathbf{L}_{OB}^A\boldsymbol{q}_A\rangle\rangle, \tag{2.41}$$

where the angle brackets represent the scalar product

$$\langle\langle\boldsymbol{q}_1,\ \boldsymbol{q}_2\rangle\rangle = \int_{-1}^{1}\boldsymbol{q}_2^H\mathbf{M}\boldsymbol{q}_1 dy, \tag{2.42}$$

and $\mathbf{M} = \operatorname{diag}\left(1, k^2, 1\right)$. The choice of this weight matrix will become evident by the end of the section where the biorthogonality condition is derived.

Using integration by parts and the boundary conditions on the state vector, the adjoint equations are derived to be

$$\left(\mathbf{L}_{OB}^A + \frac{\partial}{\partial t}\mathbf{B}_{OB}\right)\boldsymbol{q}_A = 0, \tag{2.43}$$

$$\mathbf{L}_{OB}^{A} = \begin{bmatrix} Pr.L_{OS}^{A} & -k^2\gamma\left(-\frac{d\Theta_0}{dy}\right) & -i\beta\left(RePr\right)\frac{dU_0}{dy} \\ -\frac{Ra_{h/2}Pr}{\gamma} & L_{LHE}^{A} & 0 \\ 0 & 0 & Pr.L_{SQ}^{A} \end{bmatrix},$$

where L_{OS}^{A}, L_{SQ}^{A} and L_{LHE}^{A} are the classical adjoint-Orr-Sommerfeld operator [75], adjoint-Squire operator [75], and the adjoint of the advection-diffusion operator appearing in the linearised temperature equation, respectively:

$$L_{OS}^{A} = -i\alpha ReU_0\left(k^2 - D^2\right) + 2i\alpha Re\frac{dU_0}{dy}D + \left(k^2 - D^2\right)^2, \tag{2.44}$$

$$L_{SQ}^{A} = -i\alpha ReU_0 + \left(k^2 - D^2\right), \tag{2.45}$$

$$L_{LHE}^{A} = -i\alpha RePr.U_0 + \left(k^2 - D^2\right). \tag{2.46}$$

Note that $\mathbf{B}_{OB}$ is a self-adjoint operator and the adjoint state vector $\boldsymbol{q}_A$ obeys homogeneous boundary conditions similar to the direct state vector $\boldsymbol{q}$.

Let $\boldsymbol{q}_n$ and $\boldsymbol{q}_{Am}$ be any normalized direct and adjoint eigenvectors, respectively, where n and m are indices, such that $\langle\langle \boldsymbol{q}_n,\ \boldsymbol{q}_n\rangle\rangle = \langle\langle \boldsymbol{q}_{Am},\ \boldsymbol{q}_{Am}\rangle\rangle = 1$. To find the bi-orthogonality condition, consider the product of the direct operator (2.37) applied to $\boldsymbol{q}_n$ with $\boldsymbol{q}_{Am}$,

$$\langle\langle \left(\mathbf{L}_{OB} - i\omega_n \mathbf{B}_{OB}\right)\boldsymbol{q}_n,\ \boldsymbol{q}_{Am}\rangle\rangle = 0,$$

which upon using the definition of the adjoint (2.41) gives

$$\langle\langle \boldsymbol{q}_n,\ \left(\mathbf{L}_{OB}^{A} + i\omega_n^{*}\mathbf{B}_{OB}\right)\boldsymbol{q}_{Am}\rangle\rangle = 0,$$

where * denotes complex conjugate. Since $\boldsymbol{q}_{Am}$ is an adjoint eigenvector, it satisfies the eigenfunction formulation of the adjoint operator (2.43). Thus, the above equation can be simplified to

$$-i\left(\omega_n - \omega_{(m)}\right)\langle\langle \boldsymbol{q}_n,\ \mathbf{B}_{OB}\boldsymbol{q}_{Am}\rangle\rangle = 0,$$

which gives the bi-orthogonality condition between any direct eigenvector $\boldsymbol{q}_n$ and any adjoint eigenvector $\boldsymbol{q}_{Am}$ in the form

$$\langle\langle \boldsymbol{q}_n,\ \mathbf{B}_{OB}\boldsymbol{q}_{Am}\rangle\rangle = 2k^2\delta_{nm}, \tag{2.47}$$

or, equivalently,

$$\langle \boldsymbol{q}_n,\ \boldsymbol{q}_{Am}\rangle_{\gamma} = \delta_{nm}, \tag{2.48}$$

where δ_{nm} is the Kronecker delta and the new scalar product

$$\langle \boldsymbol{q}_1,\ \boldsymbol{q}_2\rangle_{\gamma} = \int_{-1}^{1}\left[\frac{1}{2}\left(\hat{v}_1\hat{v}_2^{*} + \frac{1}{k^2}\left(D\hat{v}_1 D\hat{v}_2^{*} + \hat{\eta}_1\hat{\eta}_2^{*}\right)\right) + \frac{1}{2}\gamma^2\hat{\theta}_1\hat{\theta}_2^{*}\right]dy \tag{2.49}$$

has been introduced (here, $*$ denotes complex conjugate). The corresponding norm is given by

$$\|\boldsymbol{q}\|_{\gamma}^{2} = \int_{-1}^{1}\left[\frac{1}{2}\left(|\hat{v}|^2 + \frac{1}{k^2}\left(|D\hat{v}|^2 + |\hat{\eta}|^2\right)\right) + \frac{1}{2}\gamma^2\left|\hat{\theta}\right|^2\right]dy, \tag{2.50}$$

which is precisely the norm $E\left(t;\gamma\right)$ defined in terms of primitive variables in equation (2.36) but expressed here in reduced variables (see [75] for a similar derivation).

Chapter 3

Modal Stability Analysis

"Eternity is a very long time (.., especially towards the end.)"

– Woody Allen.

3.1 Formulation

In modal stability analysis small disturbances are resolved into normal modes (2.23)-(2.24), which may be treated separately because each mode satisfies the linear system (2.26)-(2.28):

$$\left[\left(-i\omega + i\alpha RePrU_0\right)\left(D^2-k^2\right) - i\alpha RePr\frac{d^2U_0}{dy^2}\right]\hat{v} = Pr\left(D^2-k^2\right)^2\hat{v} - k^2 Ra_{h/2}Pr\hat{\theta}, \tag{3.1}$$

$$\left(-i\omega + i\alpha RePrU_0\right)\hat{\eta} + i\beta RePr\frac{dU_0}{dy}\hat{v} = Pr\left(D^2-k^2\right)\hat{\eta}, \tag{3.2}$$

$$\left(-i\omega + i\alpha RePrU_0\right)\hat{\theta} + \frac{d\Theta_0}{dy}\hat{v} = \left(D^2-k^2\right)\hat{\theta}, \tag{3.3}$$

where $D = \frac{d}{dy}$. Along with the homogeneous boundary conditions $\hat{v}(\pm 1) = 0$, $D\hat{v}(\pm 1) = 0$, $\hat{\eta}(\pm 1) = 0$ and $\hat{\theta}(\pm 1) = 0$, this forms an eigenvalue problem in ω, the complex frequency of the normal mode. The problem can be restated in terms of a dispersion relation involving ω, the streamwise wavenumber α, the spanwise wavenumber β and the control parameters Re, Ra, Pr, of the form

$$\mathcal{D}\left(\omega, \alpha, \beta; Re, Ra, Pr\right) = 0. \tag{3.4}$$

A normal mode depends on time exponentially with a complex exponent. The imaginary part of the complex frequency, say ω_i, determines if the mode grows or decays exponentially in time. If $\omega_i > 0$, then the corresponding disturbance will be amplified, growing exponentially with time until it is so large that the non-linear interactions between the eigenmodes become significant. If $\omega_i = 0$ the mode is said to be neutrally stable, and if

$\omega_i < 0$ *asymptotically stable* or *stable* because it remains small for all time. An infinitesimal disturbance in a base flow, however, will excite all modes, so that if $\omega_i > 0$ for at least one mode then the flow is *unstable*. Whereas, if $\omega_i < 0$ for all of a complete set of modes then the flow is said to be *exponentially stable*. A mode is *marginally stable* if $\omega_i = 0$ for critical values of the control parameters (here, Re, Ra and Pr) on which the complex frequency ω depends but $\omega_i > 0$ for some neighboring values of the parameters. The objective of the method of normal modes is to solve the dispersion relation (3.4) at various control parameter values in search of marginally stable modes.

3.2 Squire's Theorem in RBP and RBC flows

As seen in section 2.3, the Squire transformation holds for the system (3.1)-(3.3). At a fixed Ra and Pr, for every oblique mode for $\alpha \neq 0$ and β there exists a spanwise-uniform normal mode $\beta_{2D} = 0$ with the same complex frequency at a smaller Reynolds number Re_{2D} given by (2.33)-(2.35). The Squire equation has no explicit forcing due to buoyancy. The standard result that Squire modes are always damped [80] holds also at all α, β, Re, Ra and Pr. Thus, *for any marginally stable oblique mode at a Reynolds number Re there exists a spanwise-uniform mode at a smaller Reynolds number* Re_{2D} *and the same Rayleigh and Prandtl numbers.* In order to find the stability diagram at a fixed Ra and Pr, it is sufficient to consider only two-dimensional eigenmodes ($\beta = 0$ or $\alpha = 0$):

$$\mathcal{D}\left(\omega, \alpha = 0, \beta; Re, Ra, Pr\right) = 0, \tag{3.5}$$

and

$$\mathcal{D}\left(\omega, \alpha_{2D}, \beta_{2D} = 0; Re_{2D}, Ra, Pr\right) = 0, \tag{3.6}$$

where the former dispersion relation corresponds to streamwise-uniform eigenmodes and the latter to spanwise-uniform eigenmodes.

3.3 Numerical Technique

3.3.1 Chebyshev discretization of the governing equations

A spectral method using Chebyshev polynomials is used to discretize equations (3.1)-(3.3) along the inhomogeneous y-direction. The method is highly accurate and easy to implement in RBP and RBC flows.

The eigenfunctions $\hat{v}(y)$, $\hat{\theta}(y)$ and $\hat{\eta}(y)$ are expanded in a Chebyshev series

$$\hat{v}(y) = \sum_{j=0}^{j=N-1} a_j \Phi_j(y), \tag{3.7}$$

$$\hat{\theta}(y) = \sum_{j=0}^{j=N-1} b_j \Phi_j(y), \tag{3.8}$$

$$\hat{\eta}(y) = \sum_{j=0}^{j=N-1} c_j \Phi_j(y), \tag{3.9}$$

where a_j, b_j and c_j are complex coefficients of Chebyshev polynomials $\Phi_j(y) = \cos(j\cos^{-1} y)$ and N is the number of Gauss-Lobatto collocation points $y_n = cos(n\pi/(N-1))$ in the wall-normal direction. The second and fourth derivatives of the eigenfunctions are derived by differentiating with respect to y the Chebyshev polynomials in the series. Substituting the resulting series into (3.1)-(3.3), one obtains a discretized system which should be satisfied at each Gauss-Lobatto collocation point. For example, in the case of the Orr-Sommerfeld equation with the buoyancy term (3.1), the disretized system reads

$$\begin{aligned}\left(i\alpha RePrU_0(y_n)k^2 - i\alpha RePrU_0''(y_n) - k^4\right)\sum_{j=0}^{j=N-1} a_j\Phi_j(y_n)\\ +k^2 Ra_{h/2}Pr\sum_{j=0}^{j=N-1} b_j\Phi_j(y_n)\\ +\left(i\alpha RePrU_0(y_n) + 2k^2\right)\sum_{j=0}^{j=N-1} a_j\Phi_j''(y_n) - \sum_{j=0}^{j=N-1} a_j\Phi_j''''(y_n)\\ = i\omega\left(\sum_{j=0}^{j=N-1} a_j\Phi_j''(y_n) - k^2\sum_{j=0}^{j=N-1} a_j\Phi_j(y_n)\right),\end{aligned} \tag{3.10}$$

which should be satisfied at each Gauss-Lobatto point y_n and thus, gives rise to a system of N-equations. Here $'$ represents derivatives with respect to y. The boundary conditions become

$$\hat{v}(\pm 1) = \sum_{j=0}^{j=N-1} a_j\Phi_j(\pm 1) = 0, \tag{3.11}$$

$$D\hat{v}(\pm 1) = \sum_{j=0}^{j=N-1} a_j\Phi_j'(\pm 1) = 0, \tag{3.12}$$

$$\hat{\theta}(\pm 1) = \sum_{j=0}^{j=N-1} b_j\Phi_j(\pm 1) = 0, \tag{3.13}$$

$$\hat{\eta}(\pm 1) = \sum_{j=0}^{j=N-1} c_j\Phi_j(\pm 1) = 0. \tag{3.14}$$

Thus, the generalized eigenvalue problem for the complex frequency of the continuous state eigenfunction $\hat{\mathbf{q}} = [\hat{v}(y), \hat{\theta}(y), \hat{\eta}(y)]^T$ reduces to a discrete system

$$\mathcal{L}_{OB}\{\phi\} = i\omega\mathcal{B}_{OB}\{\phi\}, \tag{3.15}$$

where $\{\phi\}$ is

$$\{\phi\} = \begin{bmatrix} a_0 \\ \vdots \\ a_{N-1} \\ b_0 \\ \vdots \\ b_{N-1} \\ c_0 \\ \vdots \\ c_{N-1} \end{bmatrix}, \tag{3.16}$$

and $\mathcal{L}_{OB}$, $\mathcal{B}_{OB}$ are each $3N \times 3N$ matrices: they are the discretized version of the operators (2.37) containing the coefficients of the unknown complex coefficients a_j, b_j and c_j, so that

$$\mathcal{L}_{OB} = \begin{bmatrix} \mathcal{L}_{OS} & \mathcal{L}_{OSOB} & 0 \\ \mathcal{L}_{OBOS} & \mathcal{L}_{LHE} & 0 \\ \mathcal{L}_{OSSQ} & 0 & \mathcal{L}_{SQ} \end{bmatrix} \tag{3.17}$$

$$\mathcal{B}_{OB} = \begin{bmatrix} \mathcal{B}_{OS} & 0 & 0 \\ 0 & \mathbf{I} & 0 \\ 0 & 0 & \mathbf{I} \end{bmatrix}. \tag{3.18}$$

Here, each element in $\mathcal{L}_{OB}$ and $\mathcal{B}_{OB}$ is a matrix of order N ($\mathbf{I}$ and 0 are the identity and zero matrix, respectively). The boundary conditions are applied at the first and the last (also the second and the last-but-one, for $\hat{v}(y)$) row of each of the discretized operators in $\mathcal{L}_{OB}$ and $\mathcal{B}_{OB}$. For example, after applying the boundary conditions on the wall-normal velocity $\hat{v}(y)$, the operators $\mathcal{L}_{OS}$ and $\mathcal{B}_{OS}$ read

$$\mathcal{L}_{OS} = \begin{bmatrix} s_0\Phi_0(1) & \dots & s_0\Phi_{N-1}(1) \\ s_0\Phi_0'(1) & \dots & s_0\Phi_{N-1}'(1) \\ \dots & \mathcal{L}_{OS}^{(N-2)\times(N-2)} & \dots \\ s_0\Phi_0'(-1) & \dots & s_0\Phi_{N-1}'(-1) \\ s_0\Phi_0(-1) & \dots & s_0\Phi_{N-1}(-1) \end{bmatrix}, \tag{3.19}$$

$$\mathcal{B}_{OS} = \begin{bmatrix} \Phi_0(1) & \dots & \Phi_{N-1}(1) \\ \Phi_0'(1) & \dots & \Phi_{N-1}'(1) \\ \dots & \mathcal{B}_{OS}^{(N-2)\times(N-2)} & \dots \\ \Phi_0'(-1) & \dots & \Phi_{N-1}'(-1) \\ \Phi_0(-1) & \dots & \Phi_{N-1}(-1) \end{bmatrix}, \tag{3.20}$$

where s_0 is a complex constant. The eigenmodes corresponding to the eigenvalue s_0 do not satisfy the boundary conditions and by specifying a proper complex value for s_0, they can be mapped to a specific location on the complex ω-plane. Thus, the generalized eigenvalue problem can now be solved using a standard package, for example, the *eig* function in MATLAB.

3.3.2 Validation

The above spectral collocation method based on Chebyshev polynomials over Gauss-Lobatto collocation points was implemented in MATLAB to compute the stability characteristics. The computational accuracy depends primarily on the number of polynomial expansion functions N. When $N \geq 60$, the eigenvalues computed for the cases $Re = 0$ and $Ra = 0$, were observed to match up to eight digits those given in the classical textbooks [18, 75]. The values of the critical Rayleigh numbers in RBP flow for small non-zero Reynolds numbers are shown in table 3.1. The critical Rayleigh numbers correspond to transverse $2D$ rolls ($\alpha \neq 0, \beta = 0$) which are the least unstable spanwise-uniform eigenmodes at a given Reynolds number in RBP flow. The first column displays the results in Müller's [61] analytical findings pertaining to very small Reynolds numbers $Re << 1$; the values in the next column are borrowed from the numerical computations of Fujimura & Kelly [25] and the critical Rayleigh numbers computed with the above discretization technique are presented in the third column. Our results agree with Muller's computations for very small Reynolds numbers but deviate when $Re > 5$. They, however, match up to 5 significant digits of those from the more accurate and recent results of Fujimura & Kelly [25].

Re	Müller [61]	Fujimura et. al. [25]	present
1	1710.1	1710.1	1710.1
2	1717.2	1717.2	1717.2
3	1728.9	1728.9	1728.9
4	1745.4	1745.5	1745.5
5	1766.5	1766.7	1766.7
6	1792.4	1792.8	1792.8
7	1822.9	1823.8	1823.8
8	1858.2	1859.6	1859.6
9	1898.1	1900.3	1900.3
10	1942.7	1946.1	1946.1
20	2647.8	2695.4	2695.4

Table 3.1: Comparison of the critical Rayleigh numbers for transverse $2D$ rolls (spanwise-uniform mode) in RBP when $Pr = 1$ ($N = 100$).

Note that all marginal stability results given in the present chapter are based on computations with $N = 100$ (or $N = 120$).

3.4 Modal stability characteristics

3.4.1 Road to the stability diagram

Modal stability characteristics of RBP and RBC are well-established [27, 26, 47]. At the beginning of the present work, it was, however, judged to be important to revisit and review the computed growth rates, eigenfunctions, etc. of the dominant disturbances in the system. In order to completely understand the stability characteristics of exponential instabilities and to take away valuable ideas, if any, to the non-modal stability analysis, an unbiased investigation was performed in the entire Rayleigh and Reynolds number space. A summary of results from such an analysis is presented in this section. Here, however, the discussion is restricted to the stability features of RBP and RBC flows that have not appeared in the literature before.

Growth Rates

Figure 3.1 shows typical plots of the maximum growth rate [2] of streamwise-independent ($\alpha = 0$) modes as a function of spanwise wavenumber β at various Rayleigh numbers ($- - --$ $Ra = 1856$, —— $Ra = 1707.78$, and $- \cdot - \cdot -$ $Ra = 1536$) for arbitrary Reynolds numbers (see discussion below). The maximum growth rate exhibits a single maximum and decreases rapidly for large β. As the Rayleigh number increases, this maximum value increases and reaches zero at $Ra = 1707.78$. When $Ra = 1856$ there is a band of spanwise wavenumbers for which the growth rate is positive. Thus, there is an infinite set of streamwise-uniform disturbances that grow exponentially at Rayleigh numbers larger than 1707.78 which is, hence, the critical Rayleigh number of the system. Note that, when $\alpha = 0$, the system of equations (3.1)-(3.3), along with the boundary conditions, is identical to the governing equations for disturbances in a static heat-conducting fluid layer between rigid walls. The equations are independent of Reynolds number, with the exception of Squire's equation (3.2). Since the Squire equation cannot support exponentially growing modes, plot 3.1 is independent of Reynolds number and base flow velocity profile. Thus, the dominant streamwise-uniform eigenmode in RBP and RBC flow at all Re is the classical Rayleigh-Bénard mode. It has, however, a non-zero streamwise velocity component when $Re > 0$ due to the presence of the forcing term $i\beta U_0'(RePr)\hat{v}$ in the Squire equation.

Now consider figure 3.2 where the maximum growth rate ω_i^{max} of spanwise-uniform modes ($\beta = 0$) is displayed as a function of streamwise wavenumber α at $Re = 3510$, $Ra = 4.85 \times 10^7$ and $Pr = 1$ in RBP flow. The spanwise-uniform modes are distinctly identified based on their respective phase speed, eigenfunction shape, etc. For example, in figure 3.2, the growth rate curve shows three distinct peaks corresponding to various sets of wavenumbers: 1. Transverse Rolls (TR), 2. Tollmien-Schlichting waves (TS), and W-mode (W stands for "weird", because it "weirdly" resembles the classical Rayleigh-Bénard mode with very large wavelengths). By convention, spanwise-uniform disturbances that exist as $Re \to 0$ and that propogate at some constant wave velocity related to the average base flow velocity $U_0(y)$ are termed as transverse rolls [27, 26, 13, 11, 47]. They correspond to the two-dimensional solution that evolve continuously from RB rolls at $Re = 0$. These are typical characteristics of the temporal growth rate in RBP flow at large Rayleigh and Reynolds numbers ($Re < 5772$, the value beyond which TS waves are unstable for $Ra \geq 0$). As shown in the figure, the largest growth rate corresponds to the so-called Transverse Rolls at large wavenumbers, followed by Tollmien-Schlichting waves at wavenumbers $\alpha \approx 0.1 - 1.25$ and finally, W-modes at very small wavenumbers. In the same way, figure 3.3 displays ω_i^{max} as a function of streamwise wavenumber α at a smaller Reynolds number $Re = 90$ and Rayleigh number $Ra = 31329$. Again, the growth rate is not monotonic with α and shows three peaks (at least 2 very distinct peaks) corresponding to the same set of eigenmodes: the TR mode with largest growth rate, TS waves with the second largest growth rate and, finally, W-modes. It is seen that TS waves still exist and that they are unstable at Reynolds numbers as low as $Re = 90$, but for a very large Rayleigh number. Upon comparing with figure 3.2, it can

---

[2] It refers to the growth rate of the dominant (spanwise-uniform/streamwise-uniform) eigenmode at some given streamwise and spanwise wavenumbers

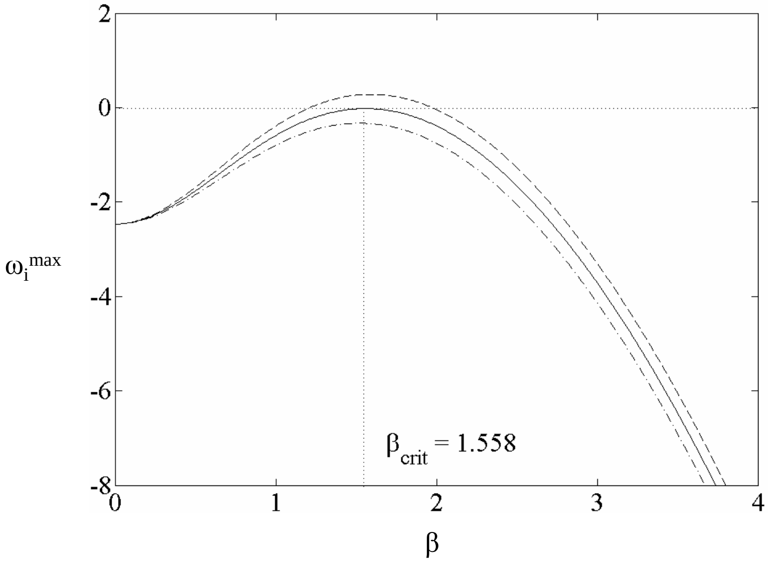

Figure 3.1: Growth rate ω_i^{max} of the dominant streamwise-uniform ($\alpha = 0$) eigenmode in Rayleigh-Bénard-Poiseuille/Couette flow at various Rayleigh numbers: $- - - -$ $Ra = 1856$, —— $Ra = 1707.78$, and $- \cdot - \cdot -$ $Ra = 1536$ when $Pr = 1$ for all Reynolds numbers (see discussion in the text)

be noted that the set of wavenumbers for which ω_i^{max} is positive has decreased. Thus, at a given Rayleigh number, the range of unstable streamwise wavenumbers decreases as the Reynolds number is decreased. As mentioned before, the spanwise-uniform modes displayed in figures 3.2 and 3.3 are identified based on their respective phase speed, eigenfunction shape, etc. At low Reynolds numbers ($Re < 100$), however, it is all the more difficult to distinguish between these eigenmodes. It was, nevertheless, observed that at very low Reynolds numbers $Re < 60$, ω_i^{max} displays a single maximum as a function of α, similarly to streamwise-uniform modes as a function of β.

In the same way, figure 3.4 presents a typical plot of the maximum growth rate ω_i^{max} as a function of streamwise wavenumber α in RBC flow at large Rayleigh and Reynolds numbers. At least two different modes corresponding to large and small wavenumbers can be identified in this control parameter range: Stationary Modes SM and Non-Stationary Modes NSM (here, the names stationary/non-stationary refer to symmetry-preserving or symmetry-breaking eigenmodes that have therefore a zero/non-zero phase speed, respectively). SM's are the fastest growing spanwise-uniform eigenmodes in RBC flow. NSM's appear typically at large Reynolds numbers. Their phase speed, as explained below (see figure 3.8), increases with Reynolds number and approaches asymptotically the maximum velocity of the base flow at very large Reynolds numbers. They, however, have negligibly small phase speeds at $Re \approx 90$ and disappear at smaller Reynolds numbers $Re < 50$.

Critical wavenumber and phase speed

In modal stability analyses, it is customary to determine the wavenumber and phase speed of marginally stable modes. The critical phase speed and wavenumber of various

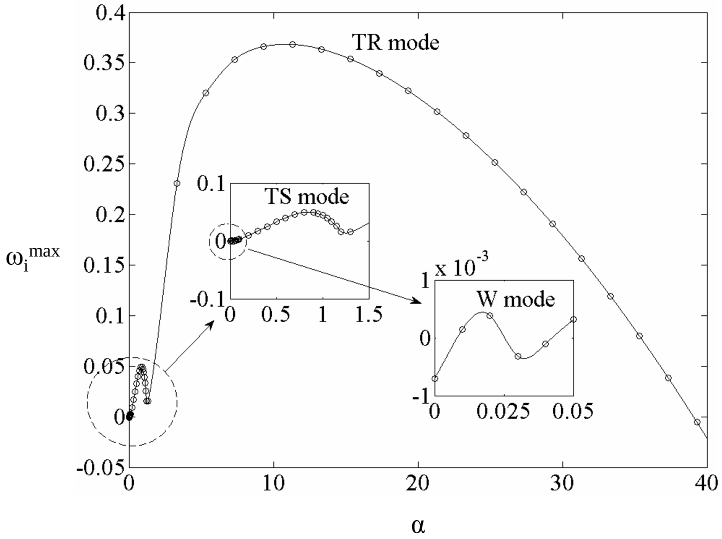

Figure 3.2: Growth rate ω_i^{max} of the dominant spanwise-uniform ($\beta = 0$) eigenmode ω_i^{max} in RBP flow: $Re = 3510$, $Ra = 4.85 \times 10^7$ and $Pr = 1$

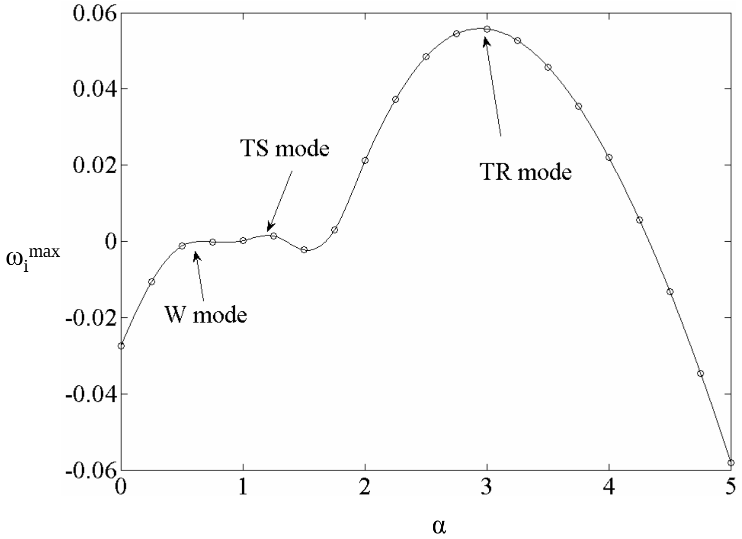

Figure 3.3: Growth rate ω_i^{max} of the dominant spanwise-uniform ($\beta = 0$) eigenmode ω_i^{max} in RBP flow: $Re = 90$, $Ra = 31329$ and $Pr = 1$.

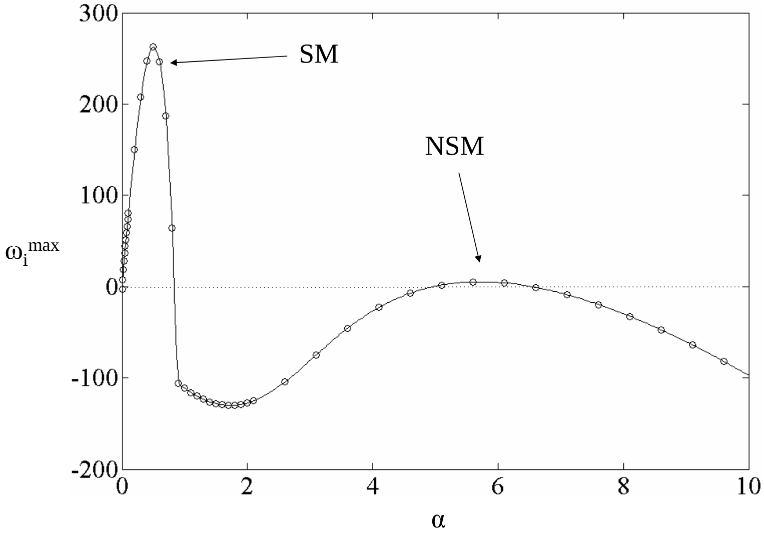

Figure 3.4: Growth rate ω_i^{max} of the dominant spanwise-uniform ($\beta = 0$) eigenmode ω_i^{max} in RBC flow: $Re = 3000$, $Ra = 1.64 \times 10^8$ and $Pr = 1$.

dominant spanwise-uniform eigenmodes in RBP flow are shown in figures 3.5 and 3.6, respectively. Here, the phase speed has been scaled with respect to the maximum base flow velocity U_{max}. The symbols correspond to different eigenmodes: □ - transverse rolls, ∘ - Tollmien-Schlichting waves and ◁ - W-modes. Observe that at all $Re > 100$, the phase speed and wavenumber of these eigenmodes are very different from each other. The phase speed of transverse rolls increases with Re, and it approaches asymptotically the value $c_r = 1$, while the phase speed of TS waves decreases with Reynolds number and W-modes have the same phase speed at all Reynolds numbers. The critical wavenumber of transverse rolls increase with Re while that of W-modes decreases with Re. Note that, for $Re > 0$, in the log-log plot 3.6, the critical spanwise wavenumber varies linearly with Reynolds number, irrespective of the spanwise-uniform mode. Thus, there exist scaling laws that relate α_{crit} and Re, namely, (1) for TR's: $\alpha_{crit} \propto Re^{1/3}$ and (2) for W-modes: $\alpha_{crit} \propto Re^{-1}$.

For RBC flows, figures 3.8 and 3.7 display the critical phase speed and wavenumber of various dominant spanwise-uniform eigenmodes, respectively. The symbols correspond to different eigenmodes: □ - Non-stationary modes and ∘ - Stationary modes. Similarly to the case of RBP flow, it can be observed that the phase speed and wavenumbers of these eigenmodes are distinct at all $Re > 100$. The critical phase speed of non-stationary modes increases with Re. The critical wavenumber of non-stationary modes increases as $\alpha_{crit} \propto Re^{1/2}$ while that of W-modes decreases as $\alpha_{crit} \propto Re^{-1}$.

Eigenfunctions of spanwise-uniform modes

A few energy transfer mechanisms in spanwise-uniform modes are discussed in this section. A qualitative understanding of why such disturbances are stabilized when $Re > 0$ is thereby obtained.

An equation for the mean kinetic energy of spanwise-uniform disturbances ($\beta = 0$) can be obtained by taking the scalar product of equation (2.5) with $\vec{u}$ and averaging

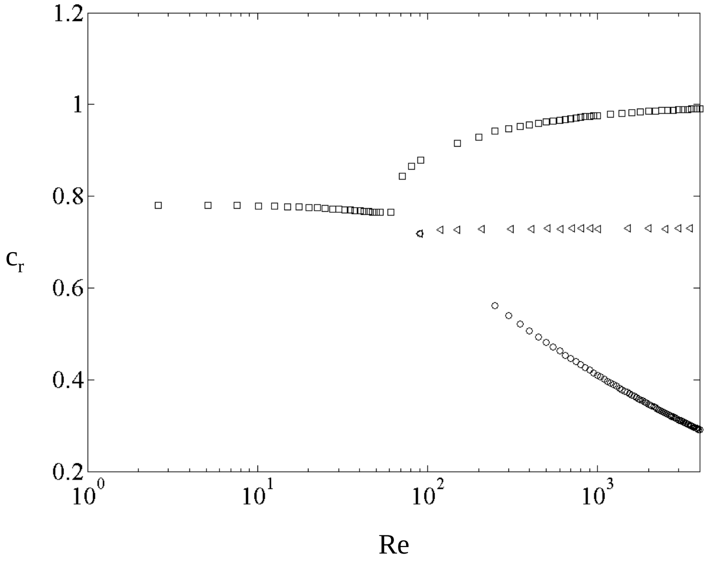

Figure 3.5: Rayleigh-Bénard-Poiseuille flow: Critical phase speed $c_r = \omega_r/\alpha$ versus Reynolds number of the first few dominant spanwise-uniform eigenmodes ($\beta = 0$); □ - transverse rolls, ○ - Tollmien-Schlichting waves and ◁ - W-modes

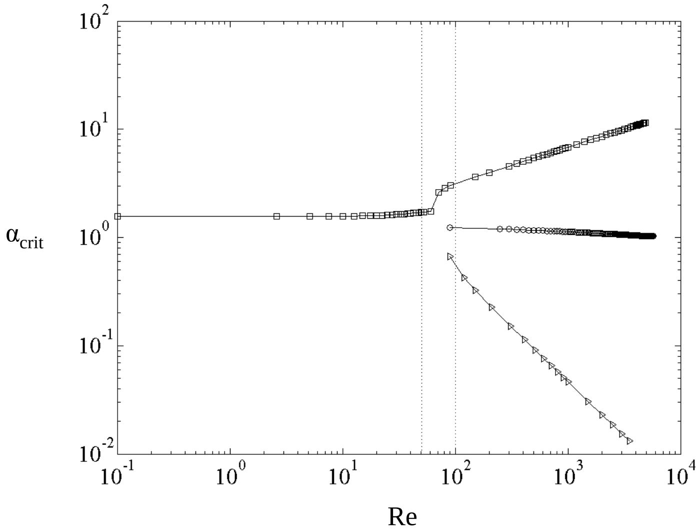

Figure 3.6: Rayleigh-Bénard-Poiseuille flow: Critical wavenumber α_{crit} versus Reynolds number of the first few dominant spanwise-uniform eigenmodes ($\beta = 0$); □ - transverse rolls, ○ - Tollmien-Schlichting waves and ◁ - W-modes

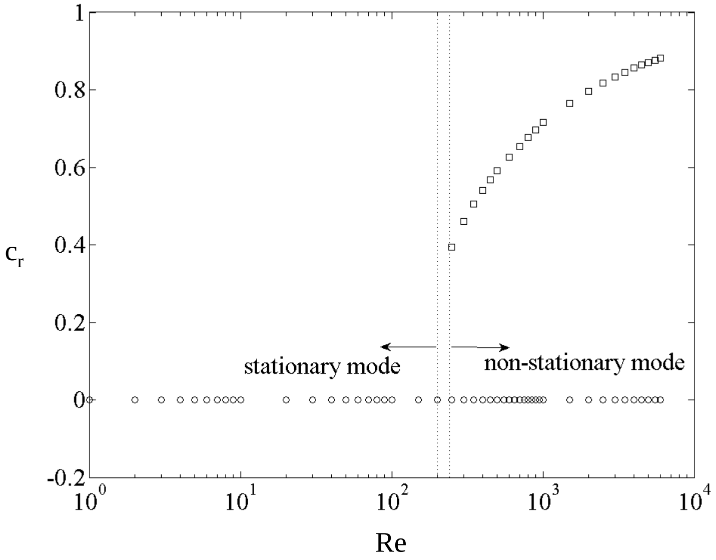

Figure 3.7: Rayleigh-Bénard-Couette flow: Critical phase speed c_r versus Reynolds number of the first few dominant spanwise-uniform eigenmodes ($\beta = 0$); □ - Non-stationary modes, and ○ - Stationary modes

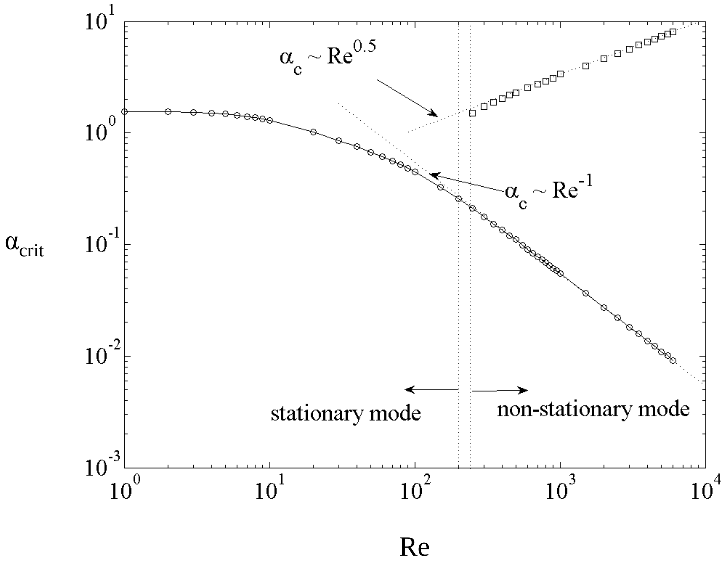

Figure 3.8: Rayleigh-Bénard-Couette flow: Critical wavenumber α_{crit} versus Reynolds number of the first few dominant spanwise-uniform eigenmodes ($\beta = 0$); □ - Non-stationary modes, and ○ - Stationary modes

over a wavelength $2\pi/\alpha$, across the width of the channel and over a unit distance in the spanwise direction while keeping in mind that the flow is homogeneous in x and z. In such a manner, terms involving $\frac{\partial}{\partial x}$ disappear because of periodic boundary conditions. Let $\langle \cdots \rangle_{avg}$ represent an average. The rate of change of the mean kinetic energy of such a disturbance is then

$$\frac{1}{2}\frac{d}{dt}\left\langle u^2+v^2\right\rangle_{avg} = RePr\left\langle -uv\frac{dU_0}{dy}\right\rangle_{avg} + RaPr\left\langle \theta v\right\rangle_{avg} - Pr\left\langle \left(\frac{\partial v}{\partial x}-\frac{\partial u}{\partial y}\right)^2\right\rangle_{avg}, \tag{3.21}$$

where the first term denotes the transfer of energy between the base flow and the disturbance via the Reynolds stress, the second represents the conversion of buoyant energy into kinetic energy of the disturbance and the last term corresponds to viscous dissipation. Note that, in the case of spanwise-uniform modes, $w = 0$. In plane Couette flow and Poiseuille flow, $\frac{dU_0}{dy} = 1$ and $\frac{dU_0}{dy} = -2y$, respectively.

Plots of the perturbation velocity vector field and temperature contours of a stationary mode and non-stationary mode in RBC are presented in figures 3.9a and 3.9b, respectively. The control parameters $Re = 1000$, $Ra = 6.343 \times 10^6$ and $Ra = 1.807 \times 10^7$ correspond to their respective critical condition i.e., when such a disturbance is marginally stable. The red and blue zones in the temperature field denote warm and cool cores, respectively. Observe that the presence of shear has led to a tilt in both streamlines and temperature contours, but more so in temperature contours. The region of maximum updraft and maximum downdraft are not directly above the center of warm and cool cores, respectively. In the case of $Re = 0$, the temperature contours and the cells of such vortical vector fields would be straight, with the region of maximum updraft being located directly above the center of the warm core and the region of downdraft being directly above the cool core. The latter arrangement tends to maximize the release of potential energy into kinetic energy of perturbations via the term coupling buoyancy and wall-normal velocity in the energy equation (3.21). In the former arrangement ($Re \neq 0$), however, the ascending motion just to the left of the maximum updraft is advecting upward the relatively cool fluid of the adjoining region as well as the warm fluid, due to the tilt. Thus, the conversion of buoyant energy into kinetic energy is not efficient in both stationary and non-stationary modes compared to the classical Rayleigh-Bénard convection. It is also observed that the streamwise velocity u and wall-normal velocity v have the same sign in most of the ascending and descending regions due to the tilt of the vortical structures. The average $\left\langle uv\frac{dU_0}{dy}\right\rangle_{avg}$ is therefore positive and hence, the energy is being transferred from the disturbance to the base flow, implying that the Reynolds stress acts to stabilize the base flow. For such reasons,*the Rayleigh number at which RBC flow becomes unstable to spanwise-uniform disturbances is much larger compared to the case with* $Re = 0$ *and also compared to that of streamwise-uniform disturbances which are not affected by the shear in the wall-normal direction.*

Similarly, in the case of RBP flow, the velocity vector plots and temperature contours of spanwise-uniform disturbances show that such disturbances are also stabilized by Reynolds stresses when $Re > 0$ (see figure 3.10). Note that, in plane Poiseuille flow, the shear changes sign across the center of the channel and correspondingly the product $\langle uv\rangle_{avg}$ changes sign from positive to negative as one crosses from the bottom of the channel to the top. Also, the temperature contours exhibit the tilt that was discussed

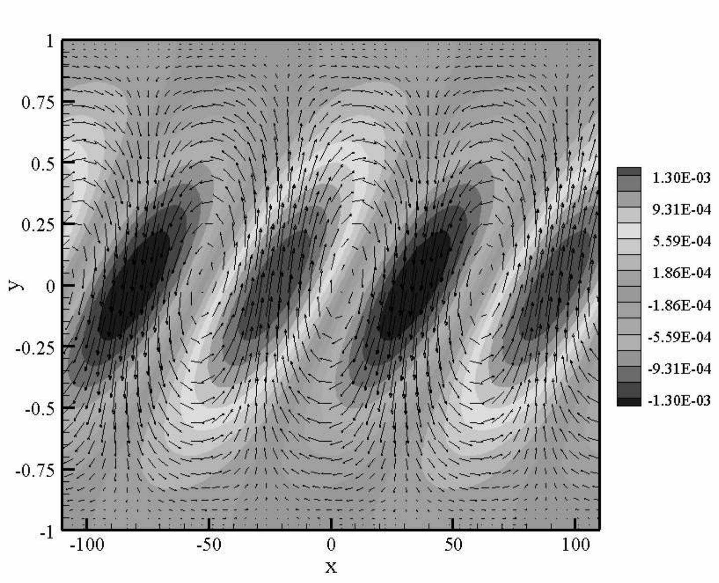

(a) Stationary mode

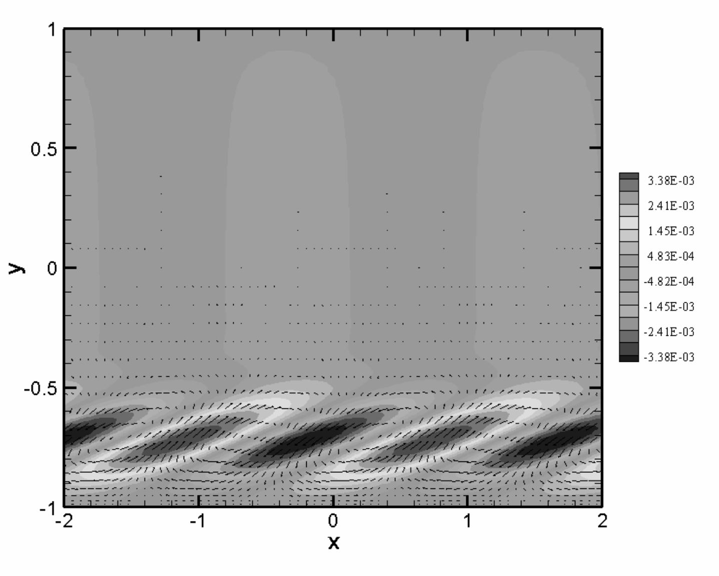

(a) Non-stationary mode

Figure 3.9: Rayleigh-Bénard-Couette flow: Velocity vector plots and temperature contours of spanwise-uniform perturbations ($\beta = 0$) at $Re = 1000$: (a) stationary mode ($\alpha = 0.05472$) and (b) non-stationary mode ($\alpha = 3.375$) when $Ra = 6.343 \times 10^6$ and $Ra = 1.807 \times 10^7$, respectively.

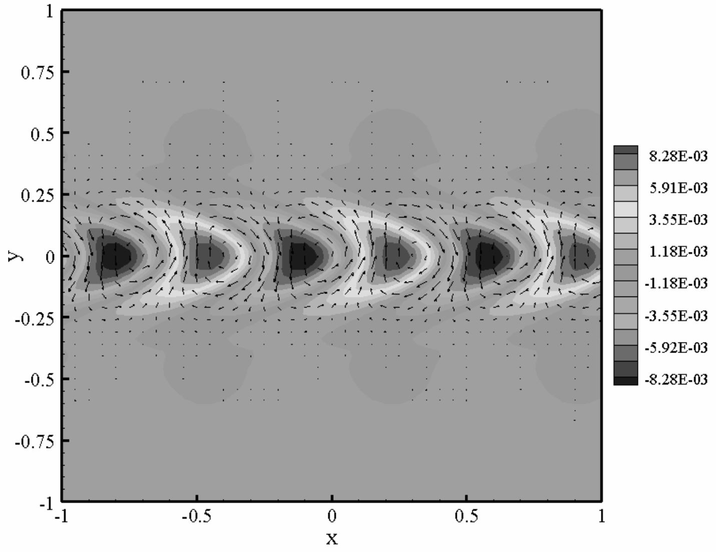

Figure 3.10: Rayleigh-Bénard-Poiseuille flow: Velocity vector plots and temperature contours of transverse rolls ($\alpha = 11$, $\beta = 0$) at $Re = 3510$ and $Ra = 4.8 \times 10^7$.

above. This implies again that buoyant energy is not efficiently transfered into kinetic energy when $Re \neq 0$. Thus, *the Rayleigh number at which RBP flow becomes unstable to spanwise-uniform disturbances is much larger compared to the case with* $Re = 0$ *and also compared to that of streamwise-uniform disturbances which are not affected by shear in the wall-normal direction.*

3.4.2 Dominant modal instability

The results of the modal stability analysis in RBP and RBC flows were recovered by numerical computation and the leading eigenmodes are discussed in this section.

Figure 3.11 depicts the stability diagram of RBP flow when $Pr = 1$. It shows the neutral curves corresponding to the Reynolds number and Rayleigh number at which a given eigenmode, streamwise-uniform ($\alpha = 0$) or spanwise-uniform ($\beta = 0$), is marginally stable ($\omega_i = 0$, where ω_i is the imaginary part of ω). Note that, as discussed in section 3.4.1, a streamwise-uniform mode becomes unstable at Ra_c^{RB}, independent of Reynolds number and Prandtl number, since in that case all the U_0-dependent terms drop-out from equations (2.26) and (2.28). Equations (2.26) and (2.28) then reduce to the linearized disturbance governing equations of a static heat-conducting Boussinesq fluid. The $\hat{\theta}$ and $\hat{v}$ eigenfunctions of the least stable eigenmode (RB) are then identical to those in the no-through flow case ($Re = 0$). Note, however, the presence of $\hat{\eta}$ perturbations governed by the Squire equation (2.27) corresponding to the tilting of the base flow vorticity by the $\hat{v}$ component as in the lift-up mechanism. Also, two distinct spanwise-uniform modes, namely, Transverse Rolls (TR), and Tollmien-Schlichting waves (TS) are presented in the stability diagram. For reasons presented in section 3.4.1, they occur at a critical

Rayleigh number which increases monotonically with Reynolds number. The so-called Oblique-Rolls (OR) are three-dimensional disturbances whose critical Reynolds number can be obtained from that of transverse rolls, through the Squire transformation (2.33)-(2.35). In figure 3.11, the marginal stability curve of one such oblique roll has also been displayed. Here, the selected OR corresponds to $\alpha/\beta = 9.95$. At a given Rayleigh number, the Reynolds number at which these modes become marginally unstable is larger than that of a TR. Note that, this is simply the consequence of Squire's theorem.

All spanwise-uniform modes except for the TS mode become unstable at some $Ra > Ra_c^{RB}$ for all non-zero Reynolds numbers. When $Ra = 0$, the TS mode becomes marginally stable at $Re = Re_c^{TS}$ and for all non-zero Rayleigh numbers below Ra_c^{RB} its critical Reynolds number decreases, however very slowly and monotonically [27, 25].

These plots suggest that there is only a weak coupling between buoyancy and shear flow stability characteristics. Nevertheless, the TS mode appears to become unstable at Reynolds numbers as low as $Re = 100$, but always at $Ra > Ra_c^{RB}$ which confirms that unstable stratification is favorable to TS instability.

For RBC flow, the marginal stability diagram is shown in figure 3.12. For the same reasons discussed in the case of RBP, the least stable eigenmode (RB) at all Reynolds numbers is a streamwise-uniform convection roll *with non-zero streamwise velocity* due to the presence of shear (lift-up mechanism). The critical Rayleigh number at which this eigenmode becomes unstable is always independent of Re and Pr. In figure 3.12, several spanwise-uniform eigenmodes: stationary mode (SM), non-stationary mode (NSM), and an oblique stationary mode (OSM) are also presented. As in RBP flow, they become marginally stable at $Ra > Ra_c^{RB}$ for all non-zero Re[27, 25] and the critical Rayleigh number of both SM and NSM increases monotonically with Reynolds number. Thus, the stability diagram remains essentially similar to the case of RBP flow. For all Reynolds numbers, however, the dominant linear instability is RBI in the presence of shear.

Thus, for Rayleigh-Bénard-Poiseuille flow, the stability boundary consists of two parts [26]. One part of the boundary is formed by the streamwise-uniform Rayleigh-Bénard mode (RB) at a constant Rayleigh number equal to Ra_c^{RB} while the other part is due to Tollmien-Schlichting waves occurring at $Re \approx Re_c^{TS}$. In the case of Rayleigh-Bénard-Couette flow, the second part of the boundary (TS waves) is absent [27]. The hatched regions in figures 3.11 & 3.12 represent the domain where RBP and RBC flows, respectively, do not show any exponential instability.

In the case of spanwise-uniform neutral modes, a few scalings laws are evident from the lines of constant slope in figures 3.11 and 3.12. It seems that this remark has not been made in previous studies. In the case of RBP flow, it is observed that, if Ra_c refers to any critical Rayleigh number, it is proportional to $Re^{4/3}$ for TR. While both SM and NSM in RBC flow obey the scaling law $Ra_c \propto Re^{1/2}$.

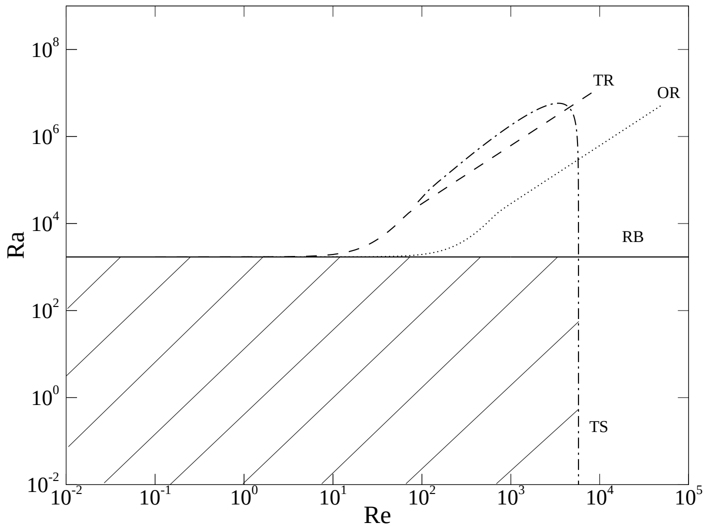

Figure 3.11: Marginal Stability Diagram of Rayleigh-Bénard-Poiseuille flow for $Pr = 1$: (———) streamwise-uniform ($\alpha = 0$) Rayleigh-Bénard convection rolls (RB), (− − −) Transverse Rolls (TR), (· − · − ·) Tollmien-Schlichting (TS) waves and (· · · · ·) Oblique Rolls (OR), $\alpha/\beta = 9.95$. The flow is linearly stable in the hatched rectangular region formed by the lines corresponding to the onset of the RB and TS modes at the lower left of the plot.

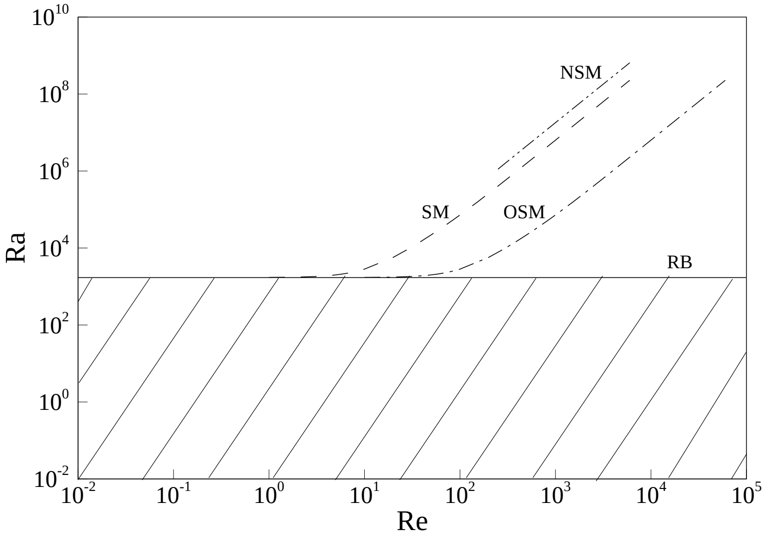

Figure 3.12: Marginal Stability Diagram of Rayleigh-Bénard-Couette for $Pr = 1$: (——) streamwise-uniform ($\alpha = 0$) Rayleigh-Bénard convection Rolls (RB), (−−−) Stationary spanwise-uniform mode (SM), (− · · −) Non-stationary spanwise-uniform mode (NSM), (· − · − ·) Oblique stationary spanwise-uniform mode (OSM): $\alpha/\beta = 9.95$. The flow is linearly stable everywhere in the hatched region below the continuous line corresponding to the onset of the RB mode.

Chapter 4

Non-modal Stability Analysis

"...it is only the details of how he lived and how he died that distinguish one man from another."

– Ernest Hemingway.

4.1 Road to Santiago

In this section, the various methods used to compute optimal growth characteristics are introduced. First, it is, however, imperative to discuss the measure which is used in the analysis.

4.1.1 Choice of an appropriate norm

The transient growth characteristics are obtained by solving equations (2.10)-(2.14), or equivalently (2.37), for an initial disturbance field that would give rise to the maximum possible growth $\boldsymbol{q}_{opt}(t_0)$. This disturbance is called the optimal initial condition [75]. It is necessary to define the optimal growth

$$G_{\mathcal{E}}(t) = \max_{\forall \boldsymbol{q}(t_0) \neq \boldsymbol{0}} \left[\frac{\mathcal{E}_{out}(t)}{\mathcal{E}_{in}(t_0)} \right], \tag{4.1}$$

where $\mathcal{E}_{out}(t)$ is an output measure corresponding to a relevant input measure $\mathcal{E}_{in}(t_0)$ and, in general, they may not be the same.

It is meaningful to study the growth in disturbance kinetic energy when the temperature field is initially undisturbed. This would denote a flow field wherein the average noise intensity in the base flow velocity field is much larger compared to the average temperature noise intensity. Note that, however, both the noise intensity fields should be negligibly small compared to the base flow for a linear stability analysis to be valid. Such a norm could be used to identify if there are any transient growth mechanisms due to wall-normal thermal stratification whereby the growth of disturbance kinetic energy is larger or smaller than that in the case of pure shear flows. For such transient growth studies, the growth function can be defined as

$$G_{K.E.}(t) = \left\{ \max_{\forall \boldsymbol{q}(t_0) \neq \boldsymbol{0}} \left[\frac{E_{K.E.}(t)}{E_{K.E.}(t_0)} \right] : \theta_0 = 0 \right\}. \tag{4.2}$$

It is also possible to find other measures that could be appropriate for the study of transient growth in RBP and RBC flow. For example, the class of norms $E(t;\gamma)$ for any $\gamma > 0$ is a positive measure whereby the non-linear terms in the perturbation kinetic energy are energy-conserving. There are many choices of relevant measures of the state vector $\boldsymbol{q} = \left[\tilde{v}, \tilde{\theta}, \tilde{\eta}\right]^T$ from the norm $E\left(t;\gamma\right)$ used to derive the adjoint equations in section 2.4: for example, if $\gamma = 1$,

$$E\left(t;1\right) = \int_{\mathtt{V}} \left[\frac{1}{2}\left(|u|^2 + |v|^2 + |w|^2\right) + \frac{1}{2}|\theta|^2\right] d\mathtt{V}, \tag{4.3}$$

which was used in the recent computations by Sameen et al. [74] and if $\gamma = \sqrt{|Ra_{h/2}|\,Pr}$,

$$E\left(t;\sqrt{|Ra_{h/2}|\,Pr}\right) = \int_{\mathtt{V}} \left[\frac{1}{2}\left(|u|^2 + |v|^2 + |w|^2\right) + \frac{1}{2}|Ra_{h/2}|\,Pr\,|\theta|^2\right] d\mathtt{V}, \tag{4.4}$$

used by Biau and Bottaro [5] in their spatial transient growth calculations. Note that the norm (4.3) does not have any physical relevance for all Rayleigh number and Reynolds numbers. The first bracketed term, however, in both norms (4.3) and (4.4) is the disturbance kinetic energy. For the case of a fluid layer heated from above (stable stratification) the term $\frac{1}{2}|Ra_{h/2}|\,Pr|\hat{\theta}|^2$ in norm (4.4) is the non-dimensional potential energy of the disturbance. This term, however, loses its significance as the disturbance potential energy in the case of a flow with unstable thermal stratification (when $Ra > 0$). This norm is identical to the total energy of the perturbations in a Boussinesq fluid in the presence of stable thermal stratification. This property is independent of Prandtl number. Also, it reduces to the kinetic energy of the perturbations when $Ra = 0$. Taking $\gamma = \sqrt{|Ra_{h/2}|\,Pr}$, the direct equations (2.37) and the adjoint equations (2.43) become identical when $Re = 0$ i.e., the linear operator of the Rayleigh-Bénard-Poiseuille/Couette problem is then self-adjoint under this specific norm [10]. It is also the measure under which the principle of exchange of stability holds for the case of pure conduction across a static fluid between rigid plates [10, 45, 18]. Nevertheless, there is no unique physically meaningful norm that can quantify the entire state vector [74]. Also, it is relatively simple to set up a code for norms of the form $E(t;\gamma)$. For such reasons, a measure of perturbation growth of the form

$$E(t) = \int_{-1}^{1} \frac{1}{2}\left[|\hat{v}|^2 + \frac{1}{k^2}\left(|D\hat{v}|^2 + |\hat{\eta}|^2\right) + |Ra_{h/2}|\,Pr\left|\hat{\theta}\right|^2\right] dy, \tag{4.5}$$

is considered for the transient growth analysis. It will later be shown that (see section 4.3.7) the optimal growth mechanisms are similar for the entire class of norms $E(t;\gamma)$.

4.1.2 Computational method

The growth function, thus, becomes

$$G(t) = \max_{\forall \boldsymbol{q}(t_0) \neq \boldsymbol{0}} \left[\frac{E(t)}{E(t_0)}\right], \tag{4.6}$$

referred to as the optimal transient growth [75, 76], i.e. the maximum possible growth at some time t over all possible non-zero initial conditions. Since different wave vectors are not linearly coupled, $G(t)$ may be considered as a function of α and β as well as the control parameters Re, Ra and Pr. It is convenient to define the quantities

$$G_{max}\left(\alpha,\beta;Re,Ra,Pr\right)=\max_{\forall t\geq 0} G\left(t,\alpha,\beta;Re,Ra,Pr\right), \tag{4.7}$$

$$S\left(Re,Ra,Pr\right)=\sup_{\alpha,\beta}\ G_{max}\left(\alpha,\beta;Re,Ra,Pr\right), \tag{4.8}$$

where G_{max} is commonly known as the maximum optimal transient growth. Let t_{max} be the time taken to attain the growth G_{max} and $(\alpha_{opt},\beta_{opt})$ be the wavenumbers corresponding to the overall optimal growth $S\left(Re,Ra,Pr\right)$.

To compute $G(t)$ the continuous linear operator, i.e. the system of equations (2.26), (2.27) and (2.28), is discretized using Chebyshev spectral functions in the same way as for the numerical computations in the modal stability analysis. The optimal growth $G(t)$ is then related to the norm of the matrix exponential of the discretized linear operator (gain matrix). Various methods of computing the matrix exponential are discussed in this section.

The domain being finite in the eigenfunction direction y, the DiPrima-Habetler theorem [17] applies and the spectrum of the system (2.37) is discrete and complete [36]. Thus, the state vector $\boldsymbol{q}$ can be obtained by an eigenfunction expansion

$$\boldsymbol{q}=\Psi\Lambda\Psi^{-1}\boldsymbol{q}_0, \tag{4.9}$$

where $\boldsymbol{q}_0$ is the initial state vector, Ψ is the eigenfunction matrix and Λ is the exponential of a diagonal matrix consisting of the eigenvalues of the system (2.37). Thus, the growth function reads

$$\begin{aligned} G(t) &= \max_{\forall \boldsymbol{q}(t_0)\neq \boldsymbol{0}} \frac{\left\|\boldsymbol{q}\right\|^2}{\left\|\boldsymbol{q}_0\right\|^2}, \\ &= \max_{\forall \boldsymbol{q}(t_0)\neq \boldsymbol{0}} \frac{\left\|\Psi\Lambda\Psi^{-1}\boldsymbol{q}_0\right\|^2}{\left\|\boldsymbol{q}_0\right\|^2}, \\ &= \left\|\Psi\Lambda\Psi^{-1}\right\|^2, \end{aligned} \tag{4.10}$$

where $\left\|\ldots\right\|^2$ denotes the norm (2.50) when $\gamma=\sqrt{\left|Ra_{h/2}\right| Pr}$. The norm of the matrix $\Psi\Lambda\Psi^{-1}$ with respect to the scalar product (2.49) can be rewritten in terms of the L_2 norm. The weight matrix in the scalar product (2.49) is $\mathbf{M}\ \mathbf{B}_{OB}$. It is positive definite with respect to the same scalar product and hence, there exists a Cholesky decomposition $\mathbf{M}\ \mathbf{B}_{OB}=\mathcal{M}^H\mathcal{M}$. The gain (4.10) may therefore be expressed as

$$\begin{aligned} G(t) &= \max_{\forall \boldsymbol{q}(t_0)\neq \boldsymbol{0}} \frac{\left\|\mathcal{M}\Psi\Lambda\Psi^{-1}\boldsymbol{q}_0\right\|_2^2}{\left\|\mathcal{M}\boldsymbol{q}_0\right\|_2^2}, \\ &= \left\|\mathcal{M}\left(\Psi\Lambda\Psi^{-1}\right)\mathcal{M}^{-1}\right\|_2^2, \end{aligned} \tag{4.11}$$

which is given by the singular value of the matrix $\mathcal{M}\left(\Psi\Lambda\Psi^{-1}\right)\mathcal{M}^{-1}$. A direct singular value decomposition [16] of this matrix would give $\mathcal{U}\Sigma\mathcal{V}^*$ where $\mathcal{U}$, $\mathcal{V}^*$ (* denotes the conjugate transpose) are complex unitary matrices and Σ is a diagonal matrix with nonnegative real numbers, known as singular values, on the diagonal. The optimal initial condition corresponding to optimal growth is then simply the column vector in $\mathcal{V}$

corresponding to the maximum singular value. Thus, computing the non-modal stability characteristics consists of two steps: (1) solve the generalized eigenvalue problem (3.1)-(3.3) and (2) use the spectrum and the eigenfunctions of the operator to compute the singular values of the eigen-decomposition of the exponential of the operator. It involves decomposition of two $3N \times 3N$ matrices in discretized spectral space. In fact, the state vector at any time can be approximated as the sum of the first M dominant eigenfunctions; hence $\boldsymbol{q}_0 = \Psi_M \mathcal{C}_0$ and $\boldsymbol{q} = \Psi_M \mathcal{C} = \Psi_M \Lambda_M \mathcal{C}_0$, where Ψ_M is a matrix of size $3N \times M$ whose M columns are the leading M eigenfunctions, Λ_M is the diagonal matrix of order M containing the first M leading eigenvalues, $\mathcal{C}$ and $\mathcal{C}_0$ are column matrices of complex constants given by the projection of the state vector on each eigenfunction direction. The optimal growth problem can now be restated as follow: maximize $\|\Psi_M \mathcal{C}\|_\gamma^2 = (\Psi_M \mathcal{C})^H \mathcal{W} (\Psi_M \mathcal{C})$ so that $\|\Psi_M \mathcal{C}_0\|_\gamma^2 = (\Psi_M \mathcal{C}_0)^H \mathcal{W} (\Psi_M \mathcal{C}_0) = 1$, where $\mathcal{W}$ is an appropriate positive-definite weight matrix that accounts for integration along the Gauss-Lobatto points and the weight matrix involved in the energy scalar product (2.49). In other words, the Lagrange functional of the optimization problem reads

$$\begin{aligned} \mathcal{P}(\mathcal{C}_0) &= \mathcal{C}^H (\Psi_M^H \mathcal{W} \Psi_M) \mathcal{C} + \sigma \left(1 - \mathcal{C}_0^H (\Psi_M^H \mathcal{W} \Psi_M) \mathcal{C}_0\right), \\ &= \mathcal{C}_0^H \mathcal{G} \mathcal{C}_0 + \sigma \left(1 - \mathcal{C}_0^H \mathcal{G}_0 \mathcal{C}_0\right), \end{aligned} \tag{4.12}$$

where $\mathcal{G} = \Psi_M^H (\Lambda_M^H \mathcal{W} \Lambda_M) \Psi_M$, $\mathcal{G}_0 = \Psi_M^H \mathcal{W} \Psi_M$, each being of order M and σ is a Lagrange multiplier. Thus, the optimal gain is given by the maximum eigenvalue of the generalized eigenvalue problem $\mathcal{G}\mathcal{C}_0 = \sigma \mathcal{G}_0 \mathcal{C}_0$. In this case, the second step in computing optimal perturbations involves only a matrix of order $M \leq N$ and usually M is much less than N i.e. only a few dominant eigenfunctions are required. The computational accuracy, however, depends on N, the number of Chebyshev polynomials required to represent the state vector in the wall-normal direction and M, the number of eigenfunctions (which are already discretized in the wall-normal direction) required to construct the optimal disturbances accurately.

If one decides to use the norm (4.2), the weight matrix $\mathcal{W}$ becomes singular. The Lagrange problem can, however, be restated by restricting the space of initial conditions $\boldsymbol{q}_0 = [\hat{v}(y), \hat{\theta}(y), \hat{\eta}(y)]^T$ to a subspace of initial conditions consisiting of vectors of the form $\boldsymbol{q}_0^{\theta_0=0} = [\hat{v}(y), 0, \hat{\eta}(y)]^T$ with zero temperature perturbations. Consider such an initial condition that is expressed as a sum of eigenfunctions Ψ_M with components $\mathcal{C}_0^{\theta_0=0}$, i.e. $\boldsymbol{q}_0^{\theta_0=0} = \Psi_M \mathcal{C}_0^{\theta_0=0}$. An orthogonal basis for such a subspace of initial conditions is then the null space of the matrix $\mathcal{W}_1 \Psi_M$. Here, $\mathcal{W}_1 = \mathrm{diag}(\mathrm{Z}(2N), \mathrm{I}(N))$, where $\mathrm{Z}(2N)$ is a zero matrix of order $2N$ and $\mathrm{I}(N)$ is an identity matrix of order N. If $\mathcal{V}$ forms the basis of the null space of $\mathcal{W}_1 \Psi_M$

$$\mathcal{C}_0^{\theta_0=0} = \mathcal{V} \mathcal{Y}_0, \tag{4.13}$$

where $\mathcal{Y}_0$ is a column vector whose elements are components of $\mathcal{C}_0^{\theta_0=0}$ along the orthogonal basis $\mathcal{V}$. Thus, the Lagrange functional (4.12) reads

$$\mathcal{P}(\mathcal{C}_0) = \mathcal{Y}_0^H \left(\mathcal{V}^H \mathcal{G} \mathcal{V}\right) \mathcal{Y}_0 + \sigma \left(1 - \mathcal{Y}_0^H \left(\mathcal{V} \mathcal{G}_0 \mathcal{V}\right) \mathcal{Y}_0\right) \tag{4.14}$$

Note that the size of the basis matrix $\mathcal{V}$ is $M \times K$, where $K < M \leq N$ and hence, the matrices $\mathcal{V}^H \mathcal{G} \mathcal{V}$ and $\mathcal{V}^H \mathcal{G}_0 \mathcal{V}$ are of order K. In this case, however, the computation of optimal perturbations involves three steps: (1) solve the generalized eigenvalue problem (3.1)-(3.3), (2) evaluate the null space of $\mathcal{W}_1 \Psi_M$ using singular value decomposition [16] and (3) solve the Lagrangian problem (4.14) through the generalized eigenvalue problem $\left(\mathcal{V}^H\mathcal{G}\mathcal{V}\right)\mathcal{Y}_0 = \sigma\left(\mathcal{V}^H\mathcal{G}_0\mathcal{V}\right)\mathcal{Y}_0$.

It was, however, observed that the null space method used to restrict the initial conditions to a subspace was not efficient. If the number of eigenfunctions M is increased, the eigenfunction expansion becomes more accurate. In the case of the problem (4.12), optimal growth computations converged for a relatively small value $M \approx 60$. The problem (4.14) involving null space computation required a very large $M \approx N$ and eventually, the orthogonal basis computed via singular value decomposition included spurious modes that do not satisfy the homogeneous boundary conditions. The optimal initial conditions obtained through this null space formulation did not satisfy the boundary conditions. Interestingly, however, the non-modal stability results for the case $Ra = 0$, namely, optimal growth, optimal initial condition (except for boundary points) at any time t were seen to agree with existing results. In the case $Ra \neq 0$, the optimal transient growth converged for large M and the results matched with the case of the norm (4.4). However, optimal initial conditions did not obey the boundary conditions and the first few boundary points (2 or 3) showed oscillations of an order of magnitude less than the maximum of the state vector.

The method of power iteration [51] seemed to be one way to get around the problem of restricting the initial conditions while it could also serve as a faster means to compute singular values. Here, the norm of the matrix exponential, say $\mathcal{P}$, is computed by iterative multiplication $q_{n+1} = \frac{\mathcal{P}q_n}{\|\mathcal{P}q_n\|}$. Such an iteration will converge, at large n, to the eigenvector corresponding to the eigenvalue of maximum absolute value. Let $\mathcal{A} = \mathcal{M}\left(\Psi\Lambda\Psi^{-1}\right)\mathcal{M}^{-1}$, then

$$\begin{aligned} G(t) &= \left\|\mathcal{M}\left(\Psi\Lambda\Psi^{-1}\right)\mathcal{M}^{-1}\right\|_2^2 \\ &= \left\{\max(\sigma) : (\mathcal{A}^H\mathcal{A})\chi = \sigma\chi\right\}, \end{aligned} \tag{4.15}$$

where $\mathcal{A}^H$ is the conjugate-transpose of the matrix $\mathcal{A}$, and χ is a $3N$ dimensional vector. Note that the eigenvalues of the matrix $\mathcal{A}^H\mathcal{A}$ are real and positive. Thus, to find the optimal growth using the method of power iteration, one typically follows two steps: (1) solve the generalized eigenvalue problem (3.1)-(3.3) and (2) use the spectrum and the eigenfunctions of the operator to compute the singular values of the eigen-decomposition of the exponential of the operator via the iterative multiplication

$$\chi_{k+1} = \frac{(\mathcal{A}^H\mathcal{A})\chi_n}{\|(\mathcal{A}^H\mathcal{A})\chi_n\|}, \tag{4.16}$$

starting from an initial non-zero random vector χ_0, until the ratio $\frac{\|(\mathcal{A}^H\mathcal{A})\chi_{n+1}\|}{\|\chi_{n+1}\|}$ has converged to a constant value. This constant is the maximum singular value of the matrix $\mathcal{A}^H\mathcal{A}$. Here, the elements in the vector χ_n are not the components along eigenfunction directions. But they represent the state vector at each Gauss-Lobatto collocation point. Hence, the initial condition can be restricted to a subspace by simply setting the elements corresponding to temperature perturbations to zero at each iteration. Note, however, that the eigen-decomposition also includes the spurious modes corresponding to a growth rate given by the imaginary part of s_0, say $s_{o,i}$ in the expression (3.18). If $s_{o,i}$ is large and negative, such modes would not affect the result of the optimal growth computation at sufficiently large time $\mathcal{O}(1/s_{o,i})$.

The accuracy of both methods depends on the number N of Chebyshev expansion functions and the precision of the first method also depends on the number of eigenmodes

M considered in the construction of the gain matrix. Thus, when using the former, it must be ensured that all the dominant eigenmodes are taken into account. Note that, in both methods, the direct equations in Fourier space were first discretized using Chebyshev polynomials; the eigenvalue decomposition was then performed on these direct equations and the adjoint operator was introduced only indirectly when the conjugate-transpose operation was used along with appropriate weight matrices to account for the integration along the Gauss-Lobatto points and for the positive-definite weight involved in the scalar product (2.49). As an alternative, one could have discretized both the direct and adjoint equations using Chebyshev polynomials, followed by the eigenvalue decomposition of the two matrices. Eventually, the exponential of the direct and adjoint matrices (expressed in terms of the direct and adjoint eigenfunctions, respectively) could have been used to compute the norm (4.10) or (4.11) via a forward-backward type method: forward in time through the exponential of the direct operator and backward in time through the exponential of the adjoint operator. This method is similar to power iteration wherein $(\mathcal{A}^H\mathcal{A})\chi_k$ is split into two steps. In the iteration (4.16), however, the discretized adjoint equations are not used. The aforementioned forward-backward type method had also been explored at the same time as the method of power iteration was coded in MATLAB. The author did not succeed in writing a bug-free code for the forward-backward type method.

4.1.3 Validation

The computations were successfully validated against those available in Reddy et al.[72] and Schmid and Henningson[75]. It was observed that $M \approx 60$ is sufficient to compute $G(t)$ up to 5 significant digits over all control parameter values (see figure 4.1). Cross-validations were performed between the two methods, namely, Singular Value Decomposition method and Power Iteration method, as a consistency check. In the following sections, only the results from the method of power iteration for the norm (4.4) are presented ($N = 100$).

4.2 Results: Non-modal stability analysis

4.2.1 Effect of varying Rayleigh number at constant Reynolds number

Figures 4.2 and 4.4 show the contour level curves of $\log G_{max}$ and t_{max}, respectively, with respect to streamwise and spanwise wavenumbers at different Rayleigh numbers $Ra = 0$, $Ra = 500$, $Ra = 1500$, and $Ra = 1700$ for the same Reynolds number $Re = 1000$. In the case when $Ra = 0$ (pure shear flow), the plot (figure 4.2a) reproduces the results of Reddy et. al. [72] wherein $S = 196$, $\alpha_{opt} = 0$, $\beta_{opt} = 2.04$ and $t_{max} = 76$. This corresponds to the classical lift-up mechanism [21, 53] resulting from the interaction between Orr-Sommerfeld and Squire modes due to the presence of the forcing term $-i\beta ReU'$ in the Squire equation [72, 75]. The contour levels along the α-axis ($\beta = 0$) correspond to the lowest values of G_{max}, indicating that the spanwise-uniform disturbances which grow via the Orr-mechanism [65] are only sub-dominant compared to oblique and streamwise-uniform disturbances for all Reynolds numbers [6, 72, 75].

The contours of $\log G_{max}$ are remarkably similar for all Ra and the effect of unstable stratification only moderately increases the maximum optimal growth. This

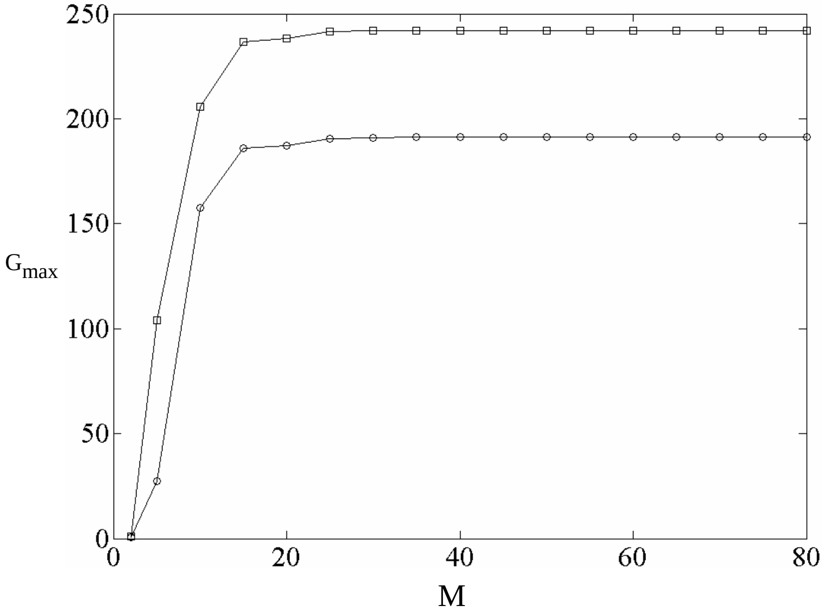

Figure 4.1: Convergence of the computed value of G_{max} with respect to the number of eigenmodes M considered for computations of transient growth: $Re = 1000$, $Pr = 1$ and ○ $Ra = 0$, □ $Ra = 500$ ($\alpha = 0$, $\beta = 1.8$).

variation is evident near the β-axis, for streamwise-uniform perturbations and some oblique perturbations which are nearly uniform in the direction of the base flow (say, nearly-streamwise-uniform disturbances: $0 \leq \alpha < 0.25$). In figures 4.2a-d, the gray bars indicate that the overall optimal growth increases from $S = 196$ at $Ra = 0$ to $S = 369.15$ at $Ra = 1700$. The growth $S(1000, Ra, 1)$ is, thus, of the same order of magnitude for all Rayleigh numbers even at the onset of streamwise-uniform convection rolls when $Ra \approx Ra_c^{RB}$ (figure 4.2d). The optimal wavenumber β_{opt} of streamwise-uniform disturbances decreases with the increase in Rayleigh number. The maximum growth via the Orr-mechanism (for $\beta = 0$) is not affected by the cross-stream temperature gradient, which is contrary to the observations of Sameen and Govindarajan [74]. Thus, *the global optimal perturbations* $S(Re, Ra, Pr = 1)$ *are always in the form of streamwise-uniform disturbances for all* Ra with an optimal spanwise wavenumber β_{opt} varying from 2.04 to 1.558 as Ra approaches Ra_c^{RB} (Note that the wavenumber of the most unstable RB mode is 1.558).

The geometry of the G_{max} contours remains similar for all Ra and Re. Figure 4.4 indicates that there is a marked difference in the contour geometry of t_{max} with increasing Rayleigh number. When $Ra = 0$ (figure 4.4a), the maximum of t_{max} lies on the β-axis and large values of t_{max} occur around this point which is seen by the white contour levels close to that axis. The time taken to attain the growth corresponding to $S(Re, Ra, Pr)$ is 76 and it is larger than that for any G_{max} along the α-axis. This implies that the Orr-mechanism is sustained only for a small time compared to the lift-up mechanism. For $Ra \neq 0$ the plots (figure 4.4b-d) display a small region of white contour levels near the β-axis and the maximum of t_{max} increases from 76 for $Ra = 0$ to 366 for $Ra = 1700$. It can be concluded that the influence of unstable stratification is limited to streamwise-uniform and nearly-streamwise-uniform perturbations (similarly to the contours of G_{max}) and the transient growth of these disturbances is sustained over a much longer time than for any other disturbances. The equivalent of the Orr-mechanism in Boussinesq fluids is sustained only over a shorter period of time (as in the case $Ra = 0$).

These observations are more evident in figure 4.6 wherein G_{max} and t_{max} are displayed for streamwise-uniform disturbances of various spanwise wavenumbers. Here, the results are for RBP flow and different symbols indicate different Rayleigh numbers. Except for a range of spanwise wavenumbers between 1 and 5, the curves are all identical. This shows that the effect of Rayleigh number in RBP is restricted only to a small range of spanwise wavenumbers.

The dashed lines in each of the G_{max} and t_{max} contour plots correspond to iso-lines of the growth $G_{max} = \frac{2}{3}S$ and $t_{max} = \frac{2}{3}T_{max}$, respectively, where T_{max} is the global maximum of all t_{max} in the α-β plane. The size of the region enclosed by this dashed line constantly decreases with increasing Rayleigh number as it approaches Ra_c^{RB} and this is even more evident in the t_{max} - contour plots. *The presence of a temperature gradient thus sharpens the selection of global optimal perturbations.*

The equivalent plots for RBC flow are presented in figures 4.3 & 4.5. They are qualitatively similar to figures 4.2 & 4.4, respectively, except that the growth S corresponds to a nearly-streamwise-uniform disturbance with $\alpha_{opt} << 1$ (Note: at large Reynolds numbers, in plane Couette flow [75] without a cross-stream temperature gradient, $\alpha_{opt} = \frac{35}{Re}$). As the Rayleigh number increases, however, α_{opt} approaches zero. In comparison with RBP, there is a more marked increase in G_{max} and t_{max} with Ra. As in RBP, this is primarily limited to streamwise-uniform and nearly-streamwise-uniform disturbances.

Thus, it is likely that lift-up remains the most dominant mechanism of transient growth and that the Orr-mechansism is negligibly affected by the presence of unstable stratification. The effect of Prandtl number will be discussed in section 4.3.6 but it may already be mentioned that this conclusion holds for all Prandtl numbers too.

4.2.2 Effect of varying Reynolds number at constant Rayleigh number

In wall-bounded shear flows without stratification the optimal transient growth of streamwise-uniform perturbations scales as Re^2 at large Reynolds numbers [31, 6, 72]. This scaling is related to the presence of the large off-diagonal term in the linear operator (2.37): the coupling term $-i\beta Re$ due to the basic flow shear appearing in the Squire equation for the wall-normal vorticity. Physically, this transient growth is due to the presence of a non-zero initial wall-normal velocity perturbation in the form of streamwise-uniform vortices that feed the wall-normal vorticity (associated to the streamwise velocity) by the tilting of base flow vorticity through the so-called lift-up mechanism [21, 53] for all $t \geq 0$. The influence of buoyancy on this scaling law is considered in this section and in section 4.3.3.

In figure 4.7 the optimal transient growth of streamwise-uniform disturbances is displayed at $Ra = 0$ and $Re = 5000$ and also, at $Ra = 1500$ for different Reynolds numbers when $Pr = 1$. The optimal transient growth and the optimization time are scaled as G_{opt}/Re^2 and t_{Re}/Re, respectively, where t_{Re} is the advective time scale scaled with respect to U_{max}. It is related to the non-dimensional time t in equations (2.4), (2.5)

(a)

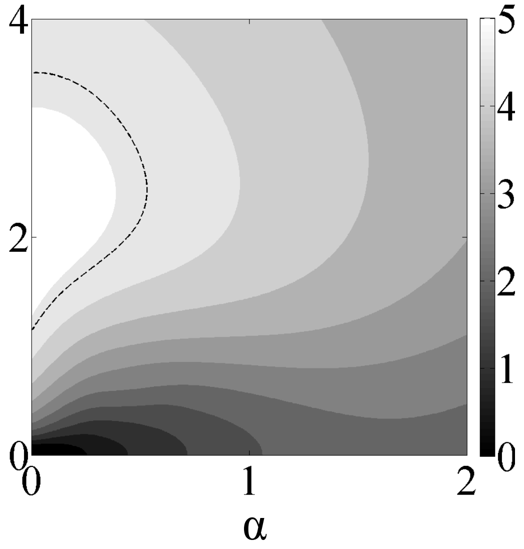

(b)

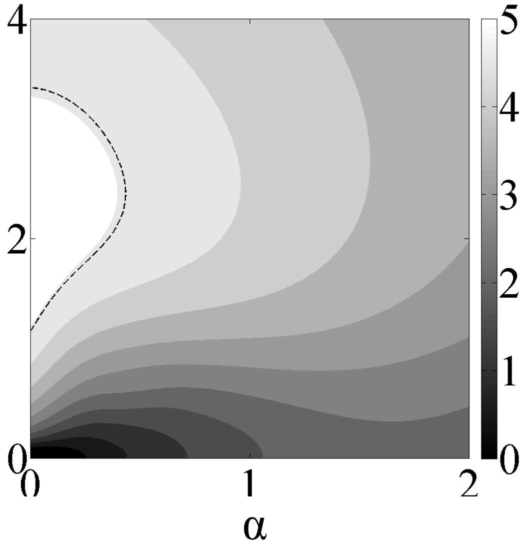

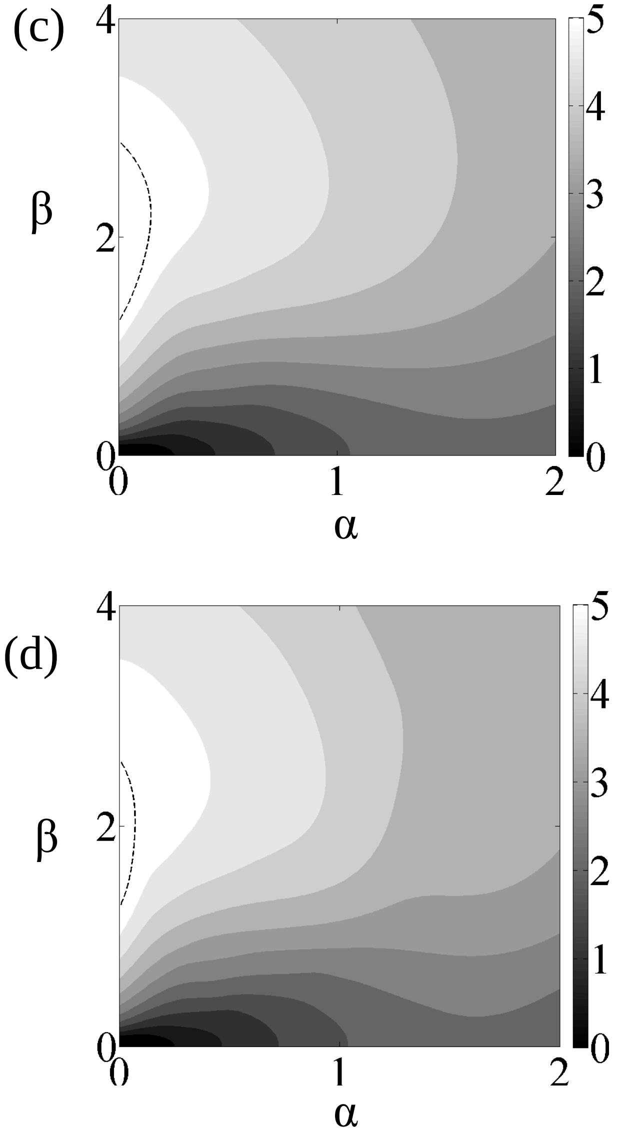

Figure 4.2: Contour plot of $\log G_{max}$ for RBP at $Re = 1000$, $Pr = 1$, and $(a)Ra = 0$, $(b)Ra = 500$, $(c)Ra = 1500$ and $(d)Ra = 1700$. The dashed lines correspond to iso-lines of the growth $G_{max} = \frac{2}{3}S$.

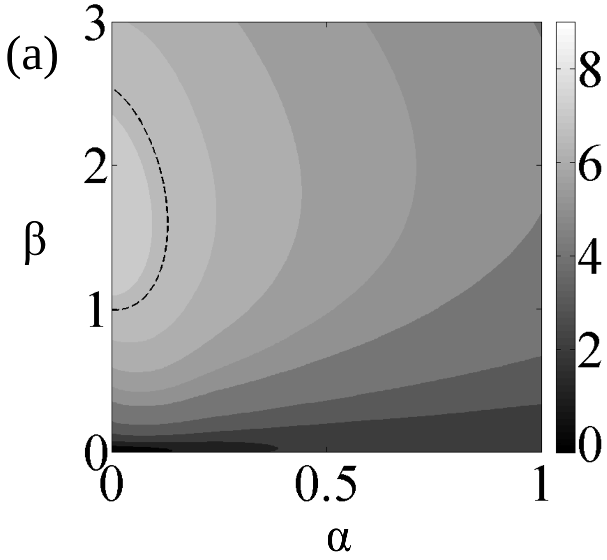
(a)
β
α
0
1
2
3
0
0.5
1
0
2
4
6
8

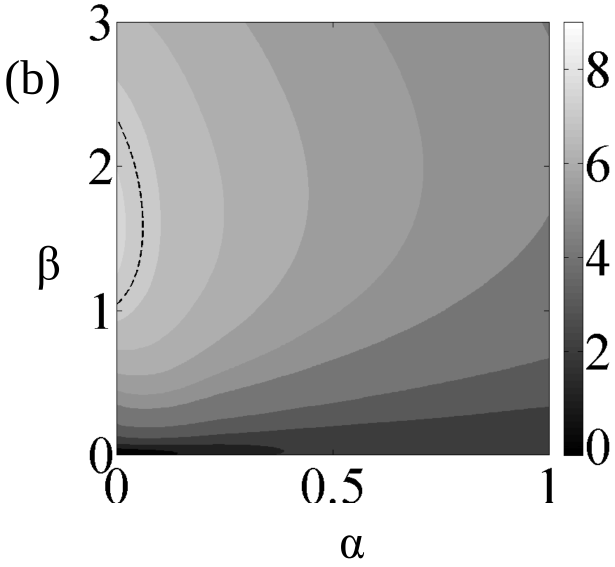
(b)
β
α
0
1
2
3
0
0.5
1
0
2
4
6
8

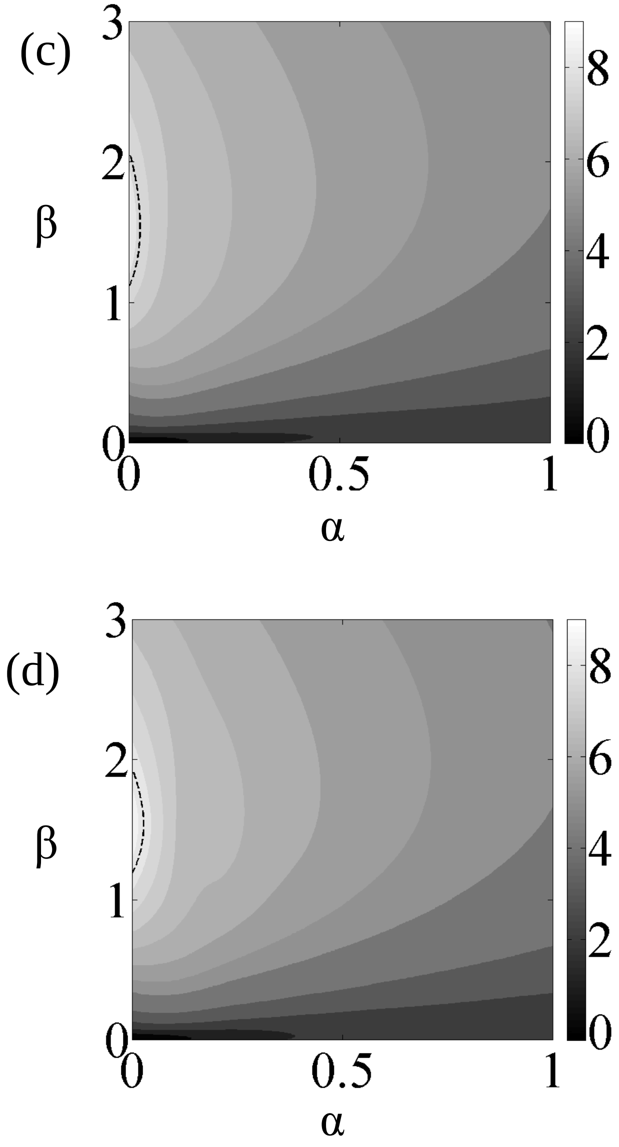

Figure 4.3: Contour plot of $\log G_{max}$ for RBC at $Re = 1000$, $Pr = 1$, and $(a)Ra = 0$, $(b)Ra = 500$, $(c)Ra = 1500$ and $(d)Ra = 1700$. The dashed lines correspond to iso-lines of the growth $G_{max} = \frac{2}{3}S$.

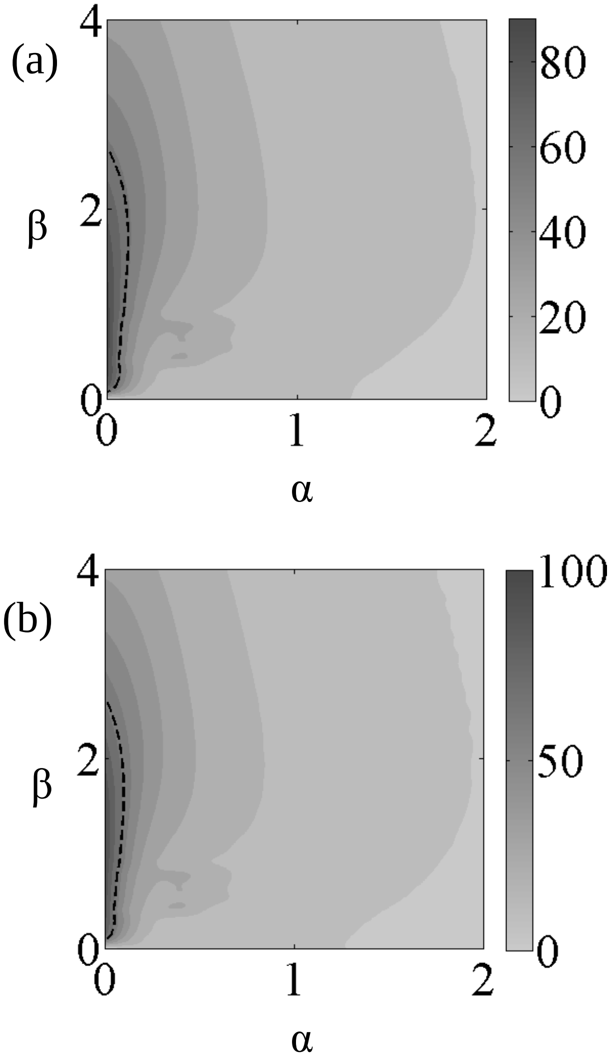
(a)
4
2
0
β
0
1
2
α
80
60
40
20
0
(b)
4
2
0
β
0
1
2
α
100
50
0

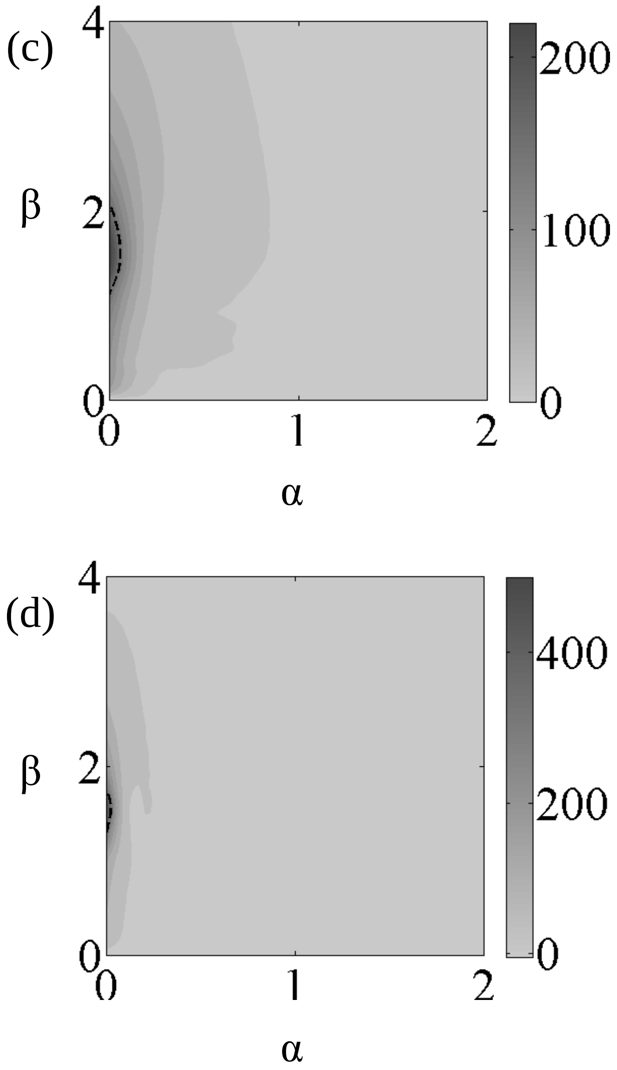

Figure 4.4: Contour plot of t_{max} for RBP at $Re = 1000$, $Pr = 1$, and $(a) Ra = 0$, $(b) Ra = 500$, $(c) Ra = 1500$ and $(d) Ra = 1700$. The dashed lines correspond to iso-lines of $t_{max} = \frac{2}{3} T_{max}$, where T_{max} is the global maximum of all t_{max} in the α-β plane.

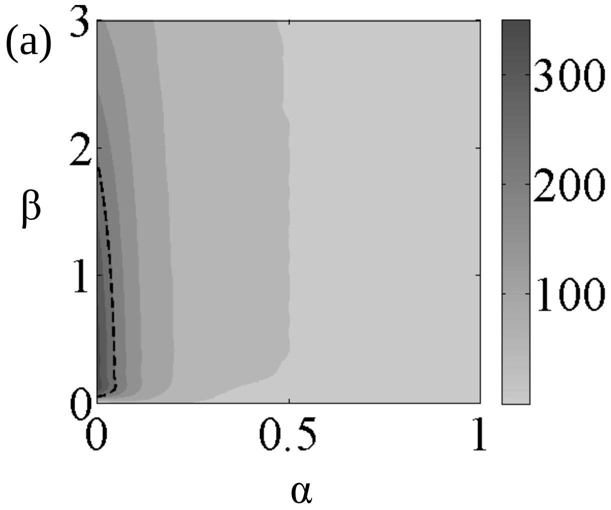
(a)
3
2
1
0
β
0
0.5
1
α
300
200
100

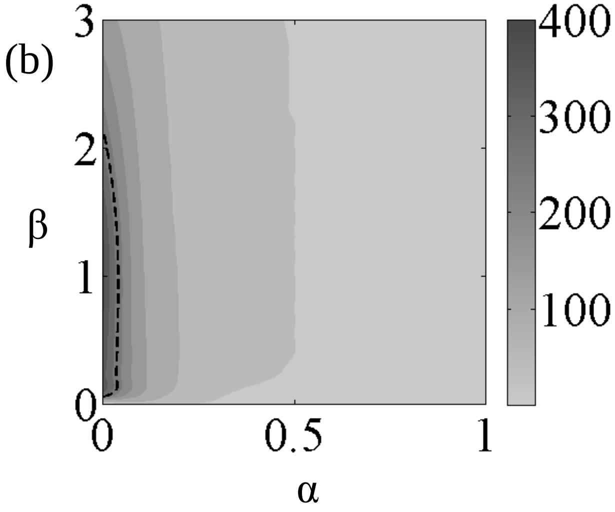
(b)
3
2
1
0
β
0
0.5
1
α
400
300
200
100

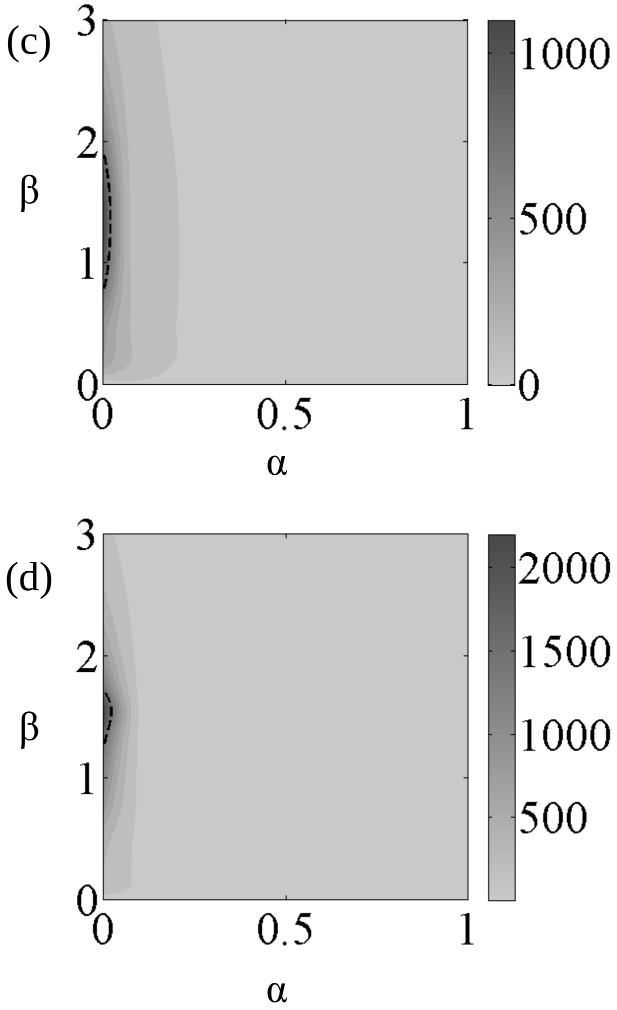

Figure 4.5: Contour plot of t_{max} for RBC at $Re = 1000$, $Pr = 1$, and $(a)Ra = 0$, $(b)Ra = 500$, $(c)Ra = 1500$ and $(d)Ra = 1700$. The dashed lines correspond to iso-lines of $t_{max} = \frac{2}{3}T_{max}$, where T_{max} is the global maximum of all t_{max} in the α-β plane.

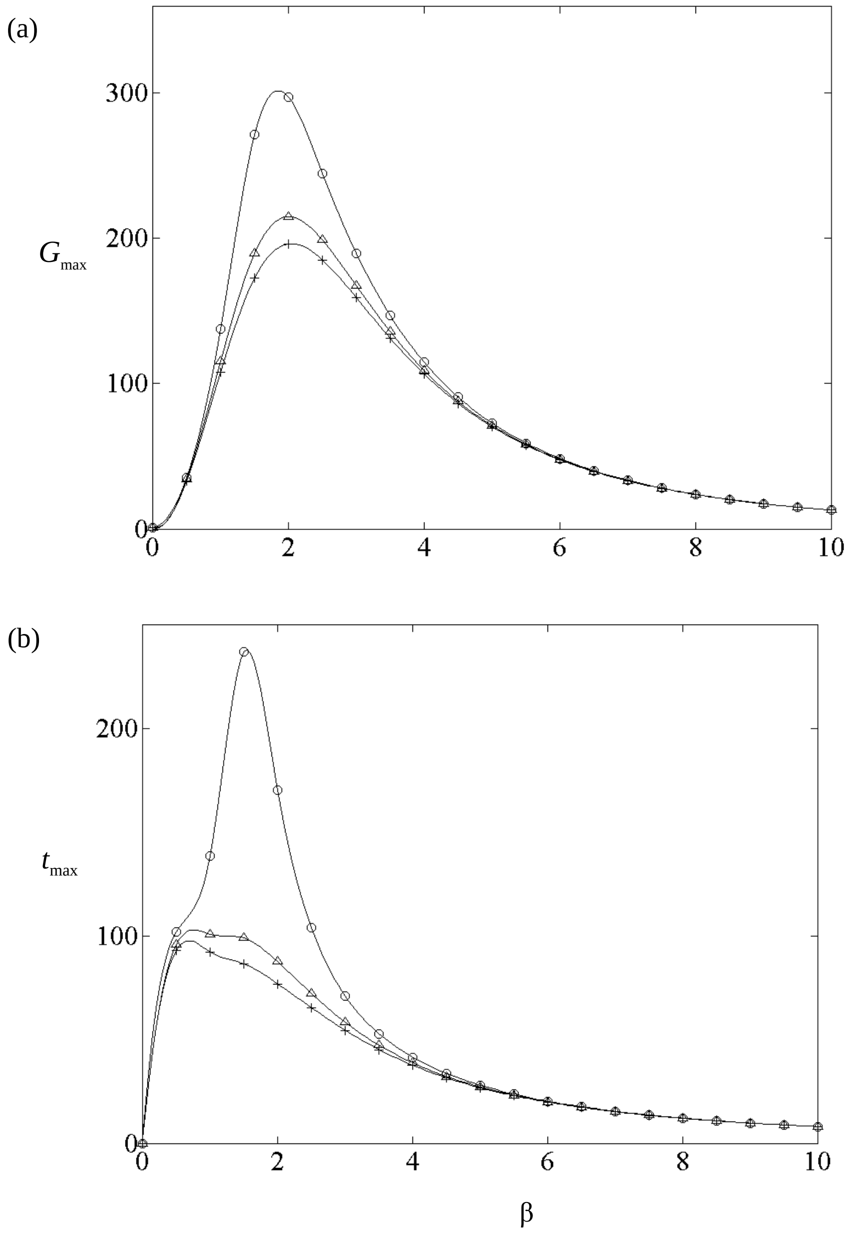

Figure 4.6: Effect of Rayleigh number on (a) G_{max} and (b) t_{max} in RBP for streamwise-uniform disturbances of various spanwise wavenumbers β at $Re = 1000$, $Pr = 1$, and $+Ra = 0$, $\triangle Ra = 500$ and $\circ Ra = 1500$.

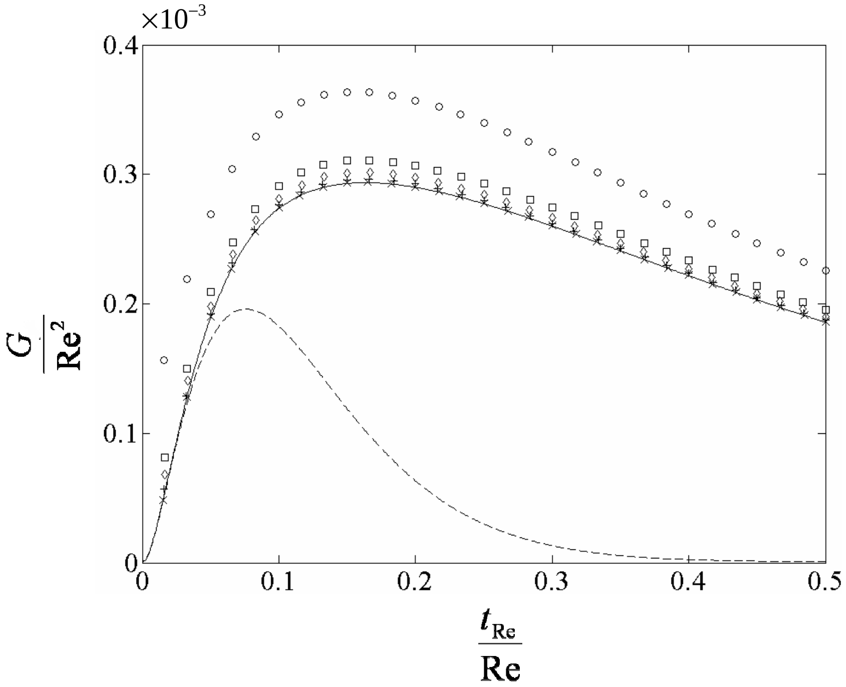

Figure 4.7: Optimal growth curves at various Reynolds numbers for streamwise-uniform disturbances in RBP at $Ra = 1500$ ($\alpha = 0$, $\beta = 2.04$): —— $Re = 5000$, $\times$ $Re = 1000$, $+$ $Re = 500$, $\diamond$ $Re = 300$, $\Box$ $Re = 200$, $\circ$ $Re = 100$ and $---$ $Ra = 0$, $Re = 5000$

& (2.6) by the relation

$$t_{Re} = \frac{U_{max}}{h/2} t^* = (RePr)\, t, \tag{4.17}$$

where t^* denotes the dimensional time variable. As the Reynolds number increases all the symbols collapse on a single continuous curve, thereby confirming that the large Reynolds number scaling law of pure shear flows, i.e.

$$\frac{G}{Re^2} = f\left(\frac{t_{Re}}{Re}\right), \tag{4.18}$$

remains valid even when buoyancy is destabilizing the flow. The scaling law fairly predicts the optimal gain even at Reynolds numbers as low as 200. Biau and Bottaro [5] presented the same scaling law in their analysis of transient growth in the spatial framework for plane channel flow under the action of stable thermal stratification and, here, a similar result is observed in the temporal framework for an unstable temperature gradient in RBP flows. The scaling law is also valid for RBC flow as seen in figure 4.8. Similar observations can be made for supercritical Rayleigh numbers $Ra > Ra_c^{RB}$. Figure 4.9 displays G_{max}/Re^2 against t_{Re}/Re for various Reynolds numbers (different symbols) at a supercritical Rayleigh number $Ra = 1800$. The continuous line corresponds to $Re = 5000$ and the symbols collapse onto this curve for large Reynolds numbers which indicates that the scaling law (4.18) holds for $Ra > Ra_c^{RB}$ as well. Figure 4.9 corresponds to the case of RBC flow. It still holds for RBP flows (results not presented

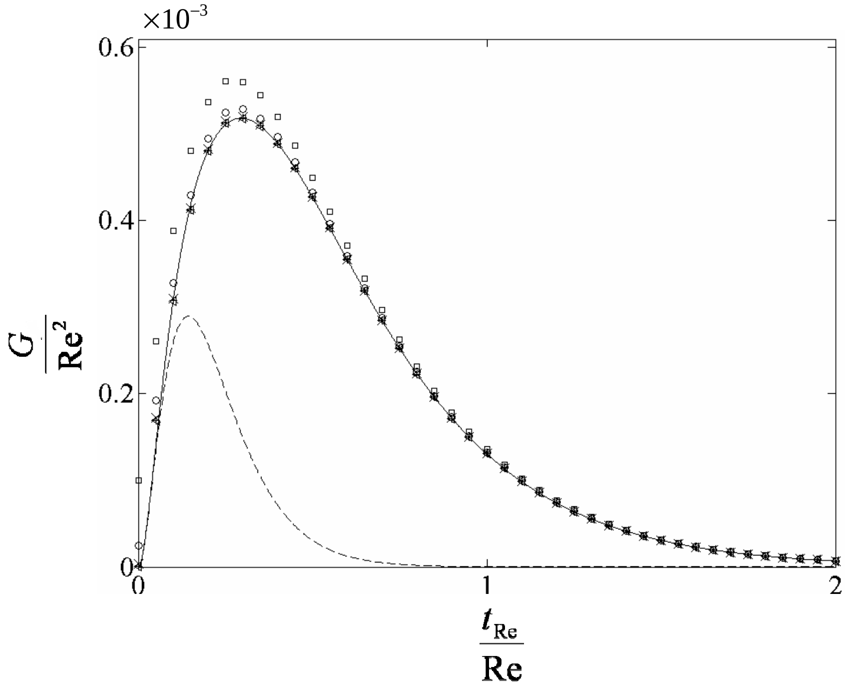

Figure 4.8: Optimal growth curves at various Reynolds numbers for streamwise-uniform disturbances in RBC at $Ra = 1000$ ($\alpha = 0$, $\beta = 1.558$): —— $Re = 5000$, $\triangleleft$ $Re = 3000$, $+$ $Re = 2000$, $\times$ $Re = 1000$, $\circ$ $Re = 400$, $\square$ $Re = 200$ and $---$ $Ra = 0$, $Re = 5000$

here). Thus, *optimal transient growth of streamwise-uniform disturbances in RBP and RBC flow at large Reynolds numbers under both stable and unstable temperature gradient retains the classical scaling law of the lift-up mechanism in pure shear flows at all Rayleigh numbers.*

The short-time transient growth, once rescaled as shown in figures 4.7 & 4.8, is remarkably independent of Re and Ra. The corresponding maximum optimal transient growth and the time at which it occurs depend only weakly on Rayleigh number. This suggests that the short-time transient growth is predominantly an inviscid process, as further examined in section 4.3.1.

4.2.3 Domain of Transient Growth

A state is said to be monotonically stable if the perturbation energy, for any perturbation, decays monotonically to zero [75]. Along the same line of thought, it is appropriate to look for Rayleigh and Reynolds numbers at which RBP/RBC flow does not exhibit transient growth. In terms of the growth function $G(t)$, it is the domain in the Re-Ra plane where $G(t)$ is less than unity for all α, β and $t > 0$.

For RBP and RBC flow, the contours of the global maximum optimal transient growth S in the stable region of the Re-Ra plane are displayed in figures 4.10 and 4.11, respectively. The hatched region in both plots represents the domain of no-transient-growth. At $Re = 0$, the flow is monotonically stable for all Rayleigh numbers up to Ra_c^{RB} where the Rayleigh-Bénard instability occurs, a feature which is consistent with

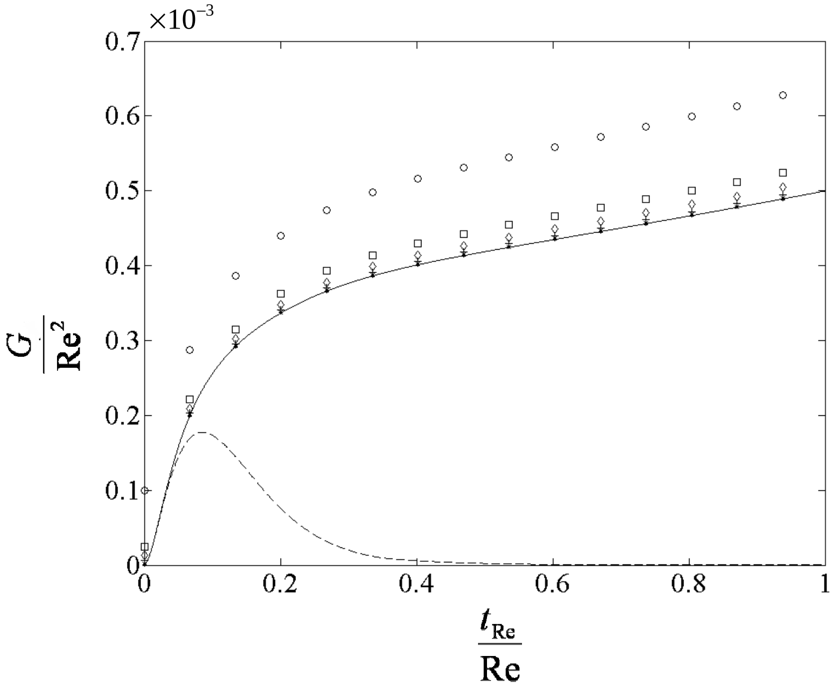

Figure 4.9: Same as figure 4.8 at a supercritical Rayleigh number $Ra = 1800$

the classical results [10] for the present choice of norm (4.5). Hence, the thick line meets the Ra-axis at $Ra = Ra_c^{RB}$ and the Re-axis at the critical Reynolds numbers, 49.6 and 20.7 for plane Poiseuille and plane Couette flow, respectively. These numbers match with the critical Reynolds number for monotonic decay of the kinetic energy as computed by Joseph [45]. The iso-contours at large Reynolds numbers are nearly vertical (figures 4.10 & 4.11) for both RBP and RBC flows indicating that the effect of unstable stratification on the overall optimal transient growth S is negligible.

4.3 Transient growth of streamwise-uniform disturbances in RBP and RBC flows

4.3.1 Lift-up Mechanism in the presence of temperature perturbations

In order to understand the transient dynamics of streamwise-uniform disturbances, the low-order model discussed by Schmid and Henningson[75] is extended to include temperature effects and buoyancy. Consider the following model of the linear operator (2.37) with 3 degrees of freedom

$$\frac{d}{dt}\begin{bmatrix}\check{v}\\ \check{\theta}\\ \check{\eta}\end{bmatrix} = \begin{bmatrix} -bPr & \sqrt{Ra_{h/2}Pr} & 0\\ \sqrt{Ra_{h/2}Pr} & -b & 0\\ RePr & 0 & -aPr\end{bmatrix}\begin{bmatrix}\check{v}\\ \check{\theta}\\ \check{\eta}\end{bmatrix}, \tag{4.19}$$

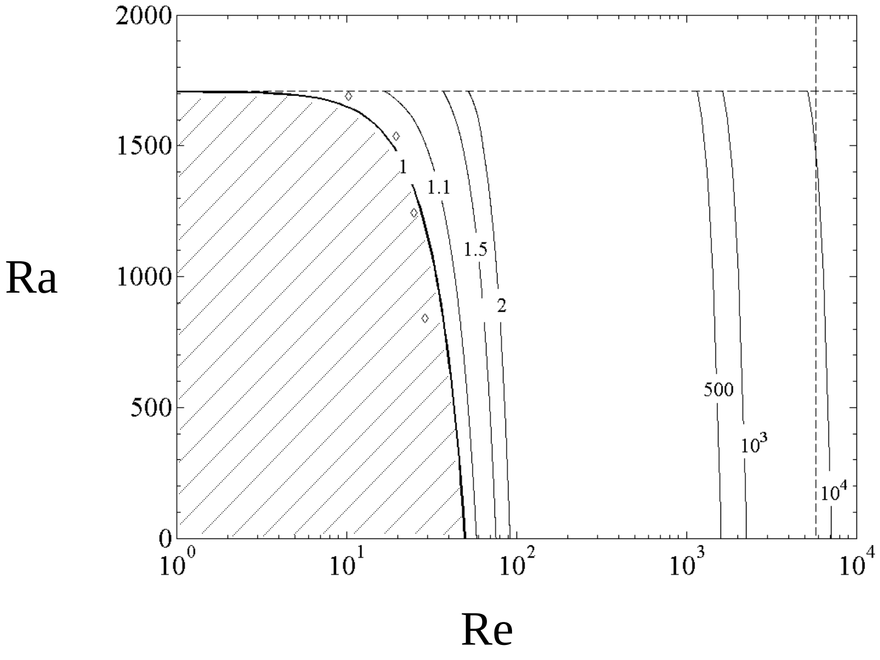

Figure 4.10: Contours of global maximum transient growth S in Rayleigh-Bénard-Poiseuille flow ($Pr = 1$). For any Ra and Re in the hatched region that is bounded by the thick line and the axes, $S = 1$ wherein the flow is monotonically stable. The symbols denote the numerical results of Shuhlze and Carmi (1976).

where the amplitudes of the field $\check{v}$, $\check{\theta}$ and $\check{\eta}$ are time-dependent only. The coefficients a, b are positive and they are related to the eigenvalues of the linear operator. When $Ra_{h/2} = 0$, $\check{v}(t)$ is decoupled from $\check{\theta}(t)$ and the matrix is analogous to the 2D vector model presented in Schmid and Henningson[75] to illustrate the nature of the lift-up mechanism in pure shear flows. The off-diagonal term $\sqrt{Ra_{h/2}Pr}$ makes the operator self-adjoint at $Re = 0$ so that the state vector $\left[\check{v}(t), \check{\theta}(t), \check{\eta}(t)\right]^T$ does not exhibit any transient growth. On comparing the dispersion relation of the model with that of the linearised disturbance equations for pure conduction of a static fluid with free-slip boundary conditions, it can be seen that b^2 plays the role of the critical Rayleigh number characterizing the linear stability of pure conduction in Boussinesq fluids[3]. Thus, the resulting operator (4.19) is stable for all $a > 0$ and $Ra_{h/2} < b^2$.

Such a model is hypothesized on the basis of the following observations. There is no explicit temperature term $\tilde{\theta}(y,t)$ in the governing equation (2.37) for the wall-normal vorticity $\tilde{\eta}(y,t)$. The only forcing term in this equation is due to the wall-normal velocity $\tilde{v}(y,t)$ and it is $\mathcal{O}(RePr)$ if β is of order unity. Bearing in mind that $\gamma = \sqrt{\mathcal{O}(Ra_{h/2}Pr)}$, the coupling between $\tilde{v}(y,t)$ and $\tilde{\theta}(y,t)$ appears as terms $\mathcal{O}(Ra_{h/2}Pr)^{1/2}$in their respective evolution equations. When β is of order unity, the dissipation term in the equation for $\tilde{\theta}(y,t)$ is only $\mathcal{O}(1)$ but it is $\mathcal{O}(Pr)$ in the equations of both $\tilde{v}(y,t)$ and $\tilde{\eta}(y,t)$. When $\alpha = 0$ the operators L_{OS} and L_{LHE} are normal and their spectrum

---

[3] alternatively, one could have used three arbitrary constants, say, a, b, c; with c in the diagonal term of the $\check{\theta}$ equation, thereby relating the critical Rayleigh number to b and c

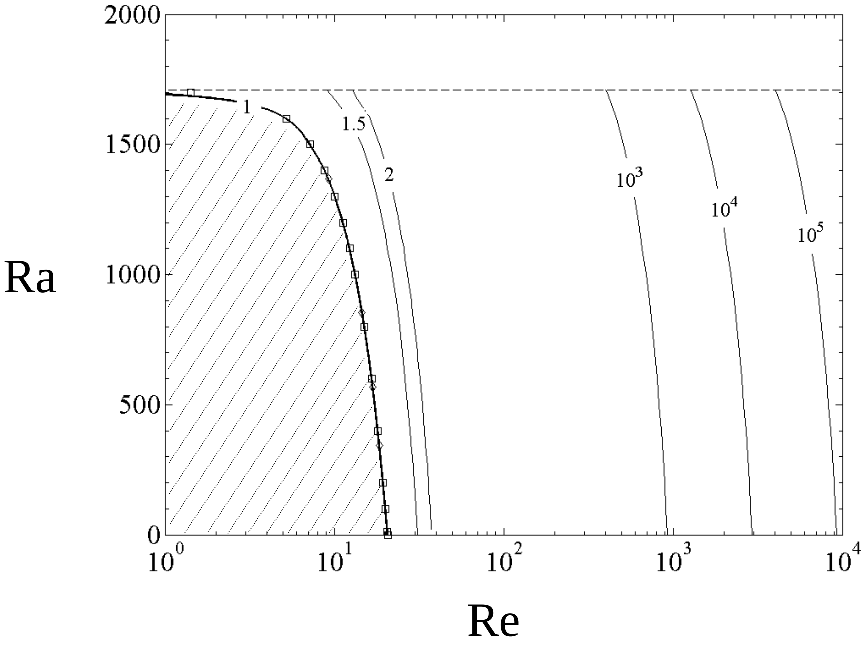

Figure 4.11: Same as in figure 4.10 but for Rayleigh-Bénard-Couette flow. The symbols □ and ◇ denote the theoretical results of Joseph (1966) and the numerical results of Shuhlze and Carmi (1976).

depends only on Ra and Pr with an unstable Rayleigh-Bénard convection roll appearing at $Ra = Ra_c^{RB}$, independently of the Reynolds and Prandtl numbers. The reduced model (4.19), therefore, appears to be a good representation of the evolution equation of streamwise-uniform disturbances.

The behavior at small time t can be obtained by expanding the solution of system (4.19) about $t = 0$. One easily obtains:

$$\begin{aligned} \begin{bmatrix} \check{v}(t) \\ \check{\theta}(t) \\ \check{\eta}(t) \end{bmatrix} &= \begin{bmatrix} \check{v}_0 \\ \check{\theta}_0 \\ \check{\eta}_0 \end{bmatrix} + \begin{bmatrix} -b\check{v}_0 + \sqrt{Ra_{h/2}Pr}\ \check{\theta}_0 \\ \sqrt{Ra_{h/2}Pr}\ \check{v}_0 - b\check{\theta}_0 \\ RePr\ \check{v}_0 - aPr\ \check{\eta}_0 \end{bmatrix} t \\ &+ \begin{bmatrix} (b^2Pr + RaPr)\check{v}_0 - b(1+Pr)\sqrt{Ra_{h/2}Pr}\ \check{\theta}_0 \\ -b(1+Pr)\sqrt{Ra_{h/2}Pr}\ \check{v}_0 + (b^2 + RaPr)\check{\theta}_0 \\ -(b+a)RePr\ \check{v}_0 + a^2\check{\eta}_0 + RePr\sqrt{RaPr}\ \check{\theta}_0 \end{bmatrix} t^2 + O(t^3), \end{aligned} \quad (4.20)$$

where $\left[\check{v}_0, \check{\theta}_0, \check{\eta}_0\right]^T$ is the initial condition. In (4.20), the largest contribution comes from the term proportional to $RePr$ in the expression for $\check{\eta}(t)$. It arises from the off-diagonal term in the model (4.19) and so $\check{\eta}(t)$ will display algebraic growth in the presence of a non-zero initial condition on $\check{v}(t)$. This is identical to the classical algebraic growth for $t \sim O(\frac{1}{Re})$ of wall-normal vorticity [75] due to the lift-up mechanism in pure shear flows. Therefore, the growth of the disturbances will be led by $\check{\eta}$, which manifests itself through the appearance of low and high speed streaks. The effect of the initial perturbation temperature field $\check{\theta}_0$ is felt only in the terms $\mathcal{O}\left(t^2\right)$ because $\check{\theta}$ does not directly force $\check{\eta}$. It affects, however, the decay rate of $\check{v}(t)$ which in turn forces $\check{\eta}$ through the lift-up mechanism. The t^2 term in system (4.20) is $\mathcal{O}(RePr\sqrt{Ra_{h/2}Pr})$ and becomes increasingly important at large Rayleigh numbers. Thus, the small-time expansion (4.20) suggests that *the influence of buoyancy on the short-time energy growth of streamwise-uniform disturbances in parallel shear flows is only secondary compared to the classical lift-up mechanism.* The initial energy growth, therefore, scales as Re^2 at large Reynolds numbers.

4.3.2 Short-time dynamics

It is shown that the short-time evolution of streamwise perturbation velocity is linear in time and is independent of Rayleigh and Prandtl numbers at very large Reynolds numbers. The arguments presented here are similar to those in Ellingsen et al [21].

If the advective time scale (as in eqn. (4.17)) and advective velocity scale had been used, instead of the time scale and velocity scale based on the thermal conductivity, the governing equations of amplitudes of the Fourier modes in RBP and RBC flows are given by expressions (2.15)-(2.19) as derived in section 2.2. Consider now the physical variables $\vec{u}_{Re} = \frac{1}{RePr}\vec{u}$ and $p_{Re} = \frac{1}{(RePr)^2}p$. The expressions (2.15)-(2.19) in physical space then become

$$\nabla \cdot \vec{u}_{Re} \quad = 0, \tag{4.21}$$

$$\left(\frac{\partial}{\partial t_{Re}} + U_0\frac{\partial}{\partial x}\right)\vec{u}_{Re} + v_{Re}\frac{dU_0}{dy}\vec{e}_x = -\nabla p_{Re} + \frac{Gr}{Re^2}\theta\vec{e}_y + \frac{1}{Re}\nabla^2\vec{u}_{Re}, \tag{4.22}$$

$$\left(\frac{\partial}{\partial t_{Re}} + U_0\frac{\partial}{\partial x}\right)\theta + v_{Re}\frac{d\Theta_0}{dy} \quad = \tfrac{1}{RePr}\nabla^2\theta. \tag{4.23}$$

If $\psi_{Re}(y, z; t)$ represents the stream function in the horizontal y-z plane then

$$v_{Re} = -\frac{\partial \psi_{Re}}{\partial z} \text{ and } w_{Re} = \frac{\partial \psi_{Re}}{\partial y}. \tag{4.24}$$

The governing equation of the streamwise velocity component written in terms of the stream function is then

$$\frac{\partial}{\partial t_{Re}}\nabla_h^2\psi_{Re} = -\frac{Gr}{Re^2}\frac{\partial\theta}{\partial z} + \frac{1}{Re}\nabla_h^4\psi_{Re}, \tag{4.25}$$

where $\nabla_h^2 = \frac{\partial^2}{\partial y^2} + \frac{\partial^2}{\partial z^2}$. When $Re >> 1$, the R.H.S. of eqn. (4.25) becomes negligibly small $\mathcal{O}(1/Re)$. Thus, in an inviscid flow (or equivalently for $t_{Re} << Re$) ψ_{Re} is independent of time. This implies that the rescaled wall-normal velocity v_{Re} and spanwise velocity w_{Re} are constant for all $t_{Re} << Re$. The streamwise velocity grows linearly with time. Also, v_{Re} and w_{Re} do not depend on any control parameters, namely, Reynolds number, Rayleigh number and Prandtl number. Hence, *at short times, the linear growth in streamwise velocity is directly related to the classical lift-up mechanism as in pure shear flows.*

4.3.3 Reynolds number scaling for $G_{max}(\alpha, \beta; Re, Ra, Pr)$

It is possible to estimate the behavior of $G_{max}(\alpha, \beta; Re, Ra, Pr)$ at $\alpha = 0$ (or small αRe) at a fixed Rayleigh and Prandtl number by employing the method followed by Gustavsson [31] and Reddy et. al. [72]. The following analysis is similar to that previously known for pure shear flows[72, 75, 54]. If the wall-normal vorticity in the Squire equation is rescaled as $\bar{\eta} = \hat{\eta}/\beta Re$, equations (2.26), (2.27) & (2.28) then depend on only two parameters, namely, $k^2 = \alpha^2 + \beta^2$ and αRe at a fixed Rayleigh number and Prandtl number. The norm (4.5) of the perturbations in the new variables $\left[\hat{v}, \hat{\theta}, \bar{\eta}\right]^T$ can then be expressed as

$$E(t) = \int_{-1}^{1} \left(|\hat{v}|^2 + \frac{1}{k^2} |D\hat{v}|^2 + |Ra_{h/2}|\, Pr \left|\hat{\theta}\right|^2 \right) dy + \frac{1}{2} \frac{\beta^2}{k^2} Re^2 \int_{-1}^{1} |\bar{\eta}|^2 dy. \tag{4.26}$$

The first bracketed term, defined as $E_{(\hat{v},\hat{\theta})}(t)$, is the contribution to the energy from the wall-normal velocity $\hat{v}$ and temperature $\hat{\theta}$ only and the second integral, defined as $E_{(\hat{\eta})}(t)$, is the contribution from the wall-normal vorticity $\hat{\eta}$ alone. When $\alpha = 0$, the evolution equations (2.12) & (2.14) for the wall-normal velocity and the temperature perturbations are independent of Reynolds number and they are identical to the linearised Oberbeck-Boussinesq equations in the linear stability analysis of pure conduction in Boussinesq fluids. If $L_{(\hat{v},\hat{\theta})}$ denotes this coupled linear operator, then $\left[\tilde{v}(y,t), \tilde{\theta}(y,t)\right]^T = \exp\{-\mathrm{i}L_{(\hat{v},\hat{\theta})}t\} \left[\tilde{v}(y,0), \tilde{\theta}(y,0)\right]^T$. Since the operator is normal for the present choice of norm $E_{(\hat{v},\hat{\theta})}$ issued from the norm (4.5) and since its spectrum lies in the lower half-plane for all k, the Hille-Yosida theorem [72] implies that $E_{(\hat{v},\hat{\theta})}(t) \leq E_{(\hat{v},\hat{\theta})}(0)$. Furthermore, the wall-normal vorticity is governed by the Squire operator L_{SQ} which is forced by $\hat{v}$ but not by $\hat{\theta}$ in (2.37). If the initial wall-normal velocity were zero, $E_{(\hat{\eta})}(t)$ would decrease monotonically given that the Squire equation is simply a diffusion equation. The definition of the growth function (4.6) gives

$$G_{max} = \max_{\forall \boldsymbol{q}(t_0) \neq \boldsymbol{0}, t \geq 0} \left[\frac{E_{(\hat{v},\hat{\theta})}(\bar{t}) + Re^2 E_{(\hat{\eta})}(\bar{t})}{E_{(\hat{v},\hat{\theta})}(0) + Re^2 E_{(\hat{\eta})}(0)} \right], \tag{4.27}$$

and at large Reynolds numbers, in order to achieve a large transient growth, the initial perturbation should be chosen so that most of the initial energy is in the velocity and temperature perturbations:

$$E_{(\hat{v},\hat{\theta})}(0) >> Re^2 E_{(\hat{\eta})}(0). \tag{4.28}$$

Since, $E_{(\hat{v},\hat{\theta})}(t)$ does not grow, it follows that, if $\bar{t} \approx t_{max}$, the time taken to achieve the maximum transient growth G_{max}, the perturbations that experience the maximum growth at large Re satisfy

$$Re^2 E_{(\hat{\eta})}(\bar{t}) >> E_{(\hat{v},\hat{\theta})}(\bar{t}). \tag{4.29}$$

Thus, for $Re >> 1$,

$$G_{max} \approx Re^2 \max_{\forall \boldsymbol{q}(t_0) \neq \boldsymbol{0}, t \geq 0} \left[\frac{E_{(\hat{\eta})}(\bar{t})}{E_{(\hat{v},\hat{\theta})}(0)} \right]. \tag{4.30}$$

The measures $E_{(\hat{v},\hat{\theta})}$ and $E_{(\hat{\eta})}$ are of order unity or less and they depend on the state variables which in turn depend only on the wavenumber $k = \beta$ (since $\alpha = 0$), Ra and Pr. The above expression therefore simply becomes

$$G_{max} \approx Re^2 \zeta(\beta; Ra, Pr), \tag{4.31}$$

where, $\zeta(\beta; Ra, Pr)$ is some function of the spanwise wavenumber β, Ra and Pr. Note that this scaling relation holds both for RBP and RBC flows and becomes more accurate at large Reynolds numbers.

4.3.4 Long-time Optimal Response

The domain being finite in the eigenfunction direction y, the DiPrima-Habetler theorem[17] applies and the spectrum is discrete and complete[36]. The solution of the direct equations (2.37) (and also the adjoint equations (2.43)) may be expanded as

$$\boldsymbol{q}\,(t) = \sum_j c_j \phi_j \exp\left(-i\omega_j t\right), \tag{4.32}$$

where ω_j and ϕ_j are the eigenvalues and eigenfunctions of the linear operator (2.37) and c_j are complex components of $q(t)$ along ϕ_j. If ω_1 is the eigenvalue with the largest imaginary part, it should lead the large time dynamics of $q(t)$:

$$\lim_{t\to\infty} \boldsymbol{q}\,(t) = c_1 \phi_1 \exp\left(-i\omega_1 t\right),$$

and the constant c_1 is given by

$$c_1 = \frac{\langle \boldsymbol{q}\,(t=0)\,,\ \phi_{A1}\rangle_\gamma}{\langle \phi_1,\ \phi_{A1}\rangle_\gamma}, \tag{4.33}$$

where $\boldsymbol{q}\,(t=0)$ is the initial condition and ϕ_{A1} the adjoint eigenfunction associated with ϕ_1. This demonstrates the classical result that the optimal initial perturbation for the large time dynamics is the adjoint of the leading eigenmode.

As noticed already, in the direct equations (2.37) the coupled linear operator for $\hat{v}$ and $\hat{\theta}$ is independent of $\hat{\eta}$ and the Squire equation for $\hat{\eta}$ is forced by the solution of this coupled operator. Hence, in general, the solution to the direct equations can be written in terms of the eigenfunction expansion (4.32), splitting modes in two families, namely, Orr-Sommerfeld-Oberbeck-Boussinesq modes (OSOB modes) and Squire modes (Sq-modes):

$$\begin{bmatrix} \tilde{v}(y,t) \\ \tilde{\theta}(y,t) \\ \tilde{\eta}(y,t) \end{bmatrix} = \sum_j A_j \exp\left(-i\lambda_j t\right) \begin{bmatrix} \hat{v}_j(y) \\ \hat{\theta}_j(y) \\ \hat{\eta}^p_j(y) \end{bmatrix} + \sum_j B_j \exp\left(-i\mu_j t\right) \begin{bmatrix} 0 \\ 0 \\ \hat{\eta}_j(y) \end{bmatrix}, \tag{4.34}$$

where $\{\lambda_j\}$ are the OSOB eigenvalues of the coupled equations (2.26) and (2.27) involving $\hat{v}$ and $\hat{\theta}$ only, $\{\hat{\eta}^p_j\}$ are the forced wall-normal vorticity functions, and $\{\mu_j\}$ are the eigenvalues of the Squire equation. The coefficients $\{A_j\}$ and $\{B_j\}$ are complex constants that can be determined from the initial conditions on the state variables. In the case of the adjoint linear operator (2.43), it is $\hat{\eta}_A$ that forces the adjoint wall-normal velocity and temperature. The adjoint Squire equation is independent of the adjoint wall-normal velocity. Similarly to the expansion (4.34), the solution to the adjoint equations can be written as

$$\begin{bmatrix}\tilde{v}_A(y,t)\\ \tilde{\theta}_A(y,t)\\ \tilde{\eta}_A(y,t)\end{bmatrix} = \sum_j A_{Aj}\exp\left(-i\lambda_j^* t\right)\begin{bmatrix}\hat{v}_{Aj}(y)\\ \hat{\theta}_{Aj}(y)\\ 0\end{bmatrix} + \sum_j B_{Aj}\exp\left(-i\mu_j^* t\right)\begin{bmatrix}\hat{v}^p_{Aj}(y)\\ \hat{\theta}^p_{Aj}(y)\\ \hat{\eta}_{Aj}(y)\end{bmatrix}, \quad (4.35)$$

where * on the eigenvalues denotes the complex conjugate and the vector eigenfunctions in the first sum are the adjoint OSOB modes corresponding to the homogeneous part of the coupled linear operator of the adjoint variables $\hat{v}_A$ and $\hat{\theta}_A$ in equation (2.43). The vector eigenfunctions in the second sum are the adjoint Squire modes, wherein the functions $\{\hat{\eta}_{Aj}\}$ are the eigenfunctions of the adjoint Squire operator and the functions $\{\hat{v}^p_{Aj}\}$ and $\{\hat{\theta}^p_{Aj}\}$ are the corresponding forced wall-normal velocity and temperature functions. The coefficients $\{A_{Aj}\}$ and $\{B_{Aj}\}$ are complex components in the direction of the adjoint eigenmodes. Note that the above eigenfunction formulation is valid only if the eigenvalues $\{\lambda_j\}$ and $\{\mu_j\}$ are distinct which is the case except for a set of parameters of zero measure.

If only streamwise-uniform disturbances ($\alpha = 0$) are considered, the direct and adjoint equations of RBP (or RBC) flow given by (2.37) and (2.43) pertaining to the scalar product (2.49) with $\gamma^2 = |Ra_{h/2}|Pr$ become identical except for the coupling term between wall-normal velocity and wall-normal vorticity. This term is dependent on Reynolds and Prandtl numbers and independent of Rayleigh number. In the direct equations, the wall-normal vorticity is forced by the wall-normal velocity and its dominant streamwise-uniform eigenmode, corresponding to the Rayleigh-Bénard convection roll, has a non-zero streamwise velocity component when $Re \neq 0$ and $Pr \neq 0$. Whereas, in the adjoint equations, it is the wall-normal vorticity term that forces the wall-normal velocity as seen in the eigenfunction expansion shown in (4.35). Hence, the governing equations (2.43) corresponding to adjoint streamwise-uniform OSOB modes $\left[\hat{v}_{Aj}, \hat{\theta}_{Aj}, 0\right]^T$ become identical with those of the pure conduction problem where the least stable eigenmode is, indeed, the Rayleigh-Bénard mode *with zero wall-normal vorticity and therefore zero streamwise velocity.* Since the eigenvalues of the adjoint modes are complex conjugates of those of the corresponding direct modes, for $Ra \neq 0$, the adjoint of the leading eigenmode is the Rayleigh-Bénard mode without its contribution from the wall-normal vorticity, or more precisely, zero streamwise velocity.

Thus, *the Rayleigh-Bénard convection mode without streamwise velocity is the optimal input to obtain the largest long-time response from RBP/RBC flows.* Note that this result is independent of Reynolds number and Prandtl number.

4.3.5 Transient Growth at arbitrary time

Figures 4.12 and 4.13 display semi-log plots of the optimal gain (continuous line) versus time for a fixed Reynolds number at various Rayleigh numbers up to Ra_c^{RB}. All the continuous curves are identical for small time until close to the maximum optimal gain which is larger for large Rayleigh numbers. At later times, however, they separate and decay at a rate which decreases with increasing Ra. The slope of the optimal growth curve at large time corresponds to the exponential decay rate of the least stable eigenmode (RB), thereby providing a justification for the slower decay rate at larger Ra. The y-intercept (t = 0) of the asymptotic straight line defines the extra gain which according to (4.33) may be estimated as $\frac{1}{Re^2}\frac{\|\phi_1\|^2\|\phi_{A1}\|^2}{|\langle\phi_1,\ \phi_{A1}\rangle_\gamma|^2}$ for large times (in figures 4.12

and 4.13, $\gamma = \sqrt{|Ra_{h/2}|\, Pr})$. The dashed curves represent the long-time asymptote as estimated with this extra gain and the slope is obtained from the imaginary part of the dominant eigenvalue (RB-mode). It is observed that the prediction at large times is excellent. At short times, the dashed line represents the prediction from the pure lift-up mechanism wherein the wall-normal velocity forces the wall-normal vorticity. In effect it represents the inviscid optimal growth and it is computed numerically at very large Reynolds numbers up to 10^8 in the case without thermal stratification[4]. It fits remarkably well with the computed short-time optimal gain (continuous curves) for all Ra. *Indeed, the entire optimal growth curve is well approximated by the piecewise continuous curve consisting of a linear branch at short-times that is independent of* Ra *and an exponentially decreasing branch at large times given by* $G \sim Re^2 \left|\exp\left(2\omega_1 t\right)\right|$, *where* ω_1 *is the complex eigenvalue of the* RB*-mode.*

Figure 4.14 compares optimal gain curve versus time (continuous line) with the response to different inputs at $Re = 1000$ and $Ra = 1000$: optimal input corresponding to G_{max} (dot-dashed line) and the classical RB-mode without streamwise velocity which is the adjoint dominant eigenmode. Both responses exhibit transient growth $\mathcal{O}\left(G_{max}\right)$ at $t_{Re} \approx \frac{1}{4} Re$ and eventually decay monotonically. This implies that the adjoint dominant eigenmode is a good approximation to the optimal initial condition at all times. The transient growth mechanism is similar at all times and it is well-approximated by pure Rayleigh-Bénard rolls. Thus, *the dominant optimal growth in the presence of a cross-stream temperature gradient is due to streamwise vortices in the form of Rayleigh-Bénard convection rolls that act in tandem with the inviscid lift-up mechanism to produce large streamwise streaks* $\mathcal{O}(Re)$ *which eventually decay exponentially in time.*

4.3.6 Effect of Prandtl number

The Prandtl number is the property of a fluid that indicates its heat diffusing capacity against its ability to diffuse fluid momentum or vice versa. An increase or decrease in Pr can result in decreased or increased heat diffusion, respectively, at a given viscous momentum diffusion. Hence, it can equivalently delay or advance the appearance of the buoyancy-induced convective motion that is responsible for the increased transient growth in RBP and RBC flows.

It was shown in section 4.2.2, when $Pr = 1$, that the standard large Reynolds number scaling law of streamwise-uniform disturbances in pure shear flows is also satisfied by Boussinesq fluids in the presence of a constant cross-stream temperature gradient for all Rayleigh numbers. The same result has also been verified for various Prandtl numbers. See, for example, in figure 4.15, the computed values of optimal growth as a function of time at different Reynolds numbers. Here, $G(t)$ is rescaled with Re^2 and t is rescaled with Re. Each symbols correspond to various Reynolds numbers ranging from 200 up to 2000. The symbols corresponding to large Reynolds number collapse on the optimal gain curve at $Re = 5000$ (continuous curve). Thus, the Reynolds number scaling of streamwise-uniform disturbances in pure shear flows remains valid even in the presence of destabilizing cross-stream temperature gradient at $Pr = 10^{-2}$.

---

[4] To compute the inviscid optimal growth curves, one can either pose a separate eigenvalue problem without any control parameters (as in section V A of Malik *et al.*[55] for the case of compressible plane Couette flow) or simply increase the Reynolds number and consider the short-time characteristics of the asymptotic large-Reynolds-number growth curve. In the results presented in figures 4.12 and 4.13, the latter approach is used to numerically compute the short time inviscid optimal growth.

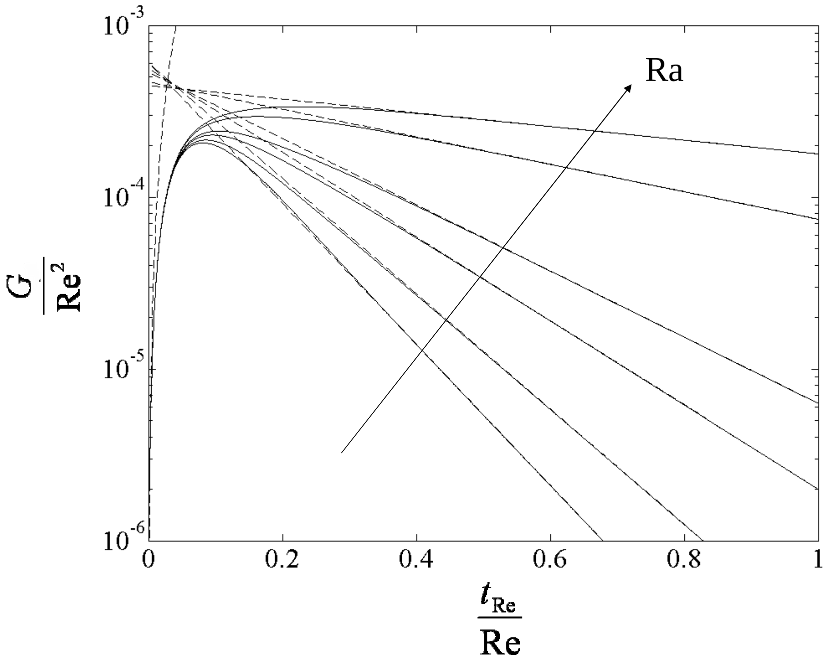

Figure 4.12: *RBP* flow: Comparison between computed optimal gain curve (——) and the asymptotic estimates for short and large times (– – –) at various Rayleigh numbers (from inside to outside: $Ra = 300$, 500, 800, 1000, 1500, 1700) at $Re = 1000$, $Pr = 1$, $\alpha = 0$ and $\beta = 2.04$

In *RBP* flow, the effect of Prandtl number on the transient growth of streamwise-uniform perturbations at a fixed Ra is shown in figure 4.16 where, as previously discussed, the optimal growth G and advective time scale t_{Re} have been scaled with Re^2 and Re, respectively. The different symbols and the continuous line correspond to the optimal growth curves for various Prandtl numbers at large Reynolds numbers (here, $Re = 1000$) when $Ra = 1700$. The dashed curve, which is almost identical with the continuous curve with the least maximum optimal gain ($\circ$ $Pr = 10^2$), represents the case when $Ra = 0$. Transient growth exists for all Prandtl numbers and the maximum optimal transient growth markedly increases with decreasing Prandtl number. As $Pr \to 0$, G_{max}/Re^2 asymptotically reaches a maximum about an order of magnitude larger than for $Ra = 0$. Meanwhile, the time at which it occurs, say t_{Re}^{max}, increases by the same factor. As $Pr \to \infty$ the maximum optimal transient growth G_{max} asymptotically reaches the value for the case without temperature gradient ($Ra = 0$) at the same Re.

These features are more vividly illustrated in figure 4.17 wherein the maximaum optimal gain G_{max} for various Rayleigh numbers has been plotted against Prandtl number at $Re = 1000$ for $\beta = 1.558$. Above $Pr = 1$, all the curves collapse on the curve $Ra = 10^{-3}$ whereas for vanishing Prandtl numbers the curves are well-separated, G_{max} being larger for large Rayleigh numbers. This suggests that, in a Boussinesq fluid of sufficiently large Prandtl number, the temperature gradients have negligible influence on the transient growth of a parallel shear flow.

The effect of Prandtl number on the dominant transient growth mechanism in *RBP*

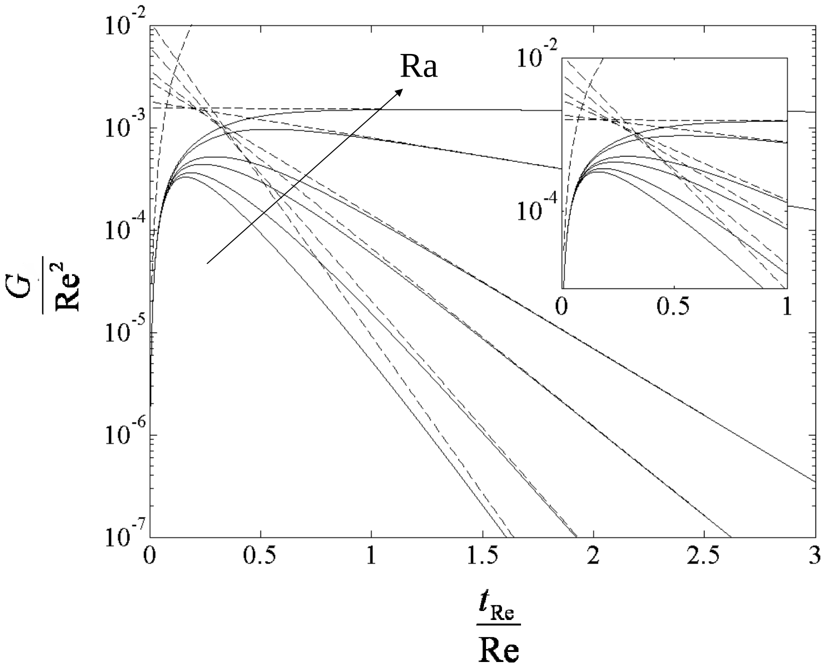

Figure 4.13: *RBC* flow: Comparison between computed optimal gain curve (——) and the asymptotic estimates for short and large times (− − −) at various Rayleigh numbers (from inside to outside: $Ra = 300$, 500, 800, 1000, 1500, 1700) at $Re = 1000$, $Pr = 1$, $\alpha = 0$ and $\beta = 1.558$

flow can be further illustrated by comparing the optimal gain curve with the response to the adjoint of the leading eigenmode input at large and small Prandtl numbers as shown in figure 4.18. Here, the optimal gain curve $G(t)$ is represented by a continuous line when $Pr = 10^{-3}$ and by a dotted line when $Pr = 10^{2}$. The dashed line ($Pr = 10^{-3}$) and dot-dashed line ($Pr = 10^{2}$) represent the time evolution of the energy from the normalized adjoint to the leading eigenmode. This eigenmode is always the Rayleigh-Bénard convection roll irrespective of the Prandtl number. While both responses exhibit transient growth, the maximum growth exhibited by the Rayleigh-Bénard convection roll at $Pr = 10^{2}$ is an order of magnitude less than G_{max} at the same Prandtl number. At $Pr = 10^{-3}$, the response to the Rayleigh-Bénard convection roll is amplified as much as the maximum optimal growth, although it is not the optimal initial condition at t_{max}. Thus, at large Pr, the Rayleigh-Bénard convection roll is not effectively amplified by the lift-up mechanism and vice versa at small Prandtl numbers. In effect, the Prandtl number acts as a coupling agent between buoyancy and shear flow transient growth mechanisms, as shown below.

As explained in section 4.3.5, the leading order transient growth process is due to the inviscid lift-up mechanism acting in tandem with the convective motion to produce large streamwise streaks $\mathcal{O}(Re)$ together with Rayleigh-Bénard rolls. Such streaks and convection rolls ultimately decay exponentially in time. The time scale at which the viscous and thermal dissipative motion can occur is $\mathcal{O}\left(l^2/\nu^*\right)$ and $\mathcal{O}\left(l^2/\kappa^*\right)$, respectively, where l is the characteristic length scale (here, $l = h/2$). Note that the Rayleigh and

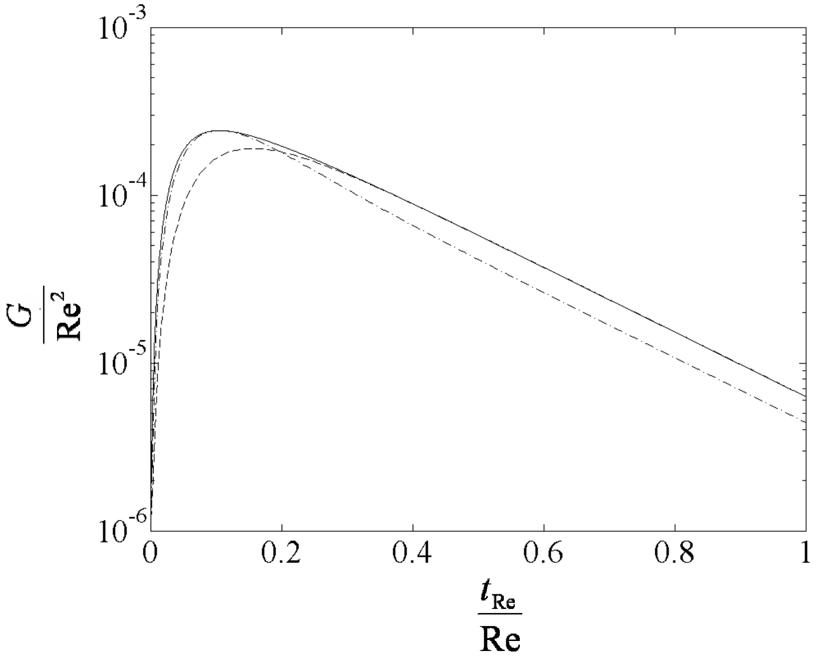

Figure 4.14: Time history of the growth $\frac{\|\boldsymbol{q}\|_{RB}^2}{\|\boldsymbol{q}_0\|_{RB}^2}$ with $\boldsymbol{q}_0$ being the optimal input at each time horizon (——); optimal input corresponding to G_{max} ($\cdot - \cdot - \cdot$) and dominant-adjoint-mode input ($- - -$) at $Re = 1000$, $Ra = 1000$, $Pr = 1$, $\alpha = 0$ and $\beta = 1.558$.

Prandtl number may be written as

$$Ra = \frac{\tau_{\nu^*}\tau_{\kappa^*}}{\tau_b} \text{ and } Pr = \frac{\tau_{\kappa^*}}{\tau_{\nu^*}}, \tag{4.36}$$

where $\tau_b = \sqrt{l/\alpha^* \Delta T g}$ is the buoyancy time scale, $\tau_{\nu^*} = l^2/\nu^*$ is the viscous momentum diffusion time scale and $\tau_{\kappa^*} = l^2/\kappa^*$ is the thermal diffusion time scale. Hence, at a fixed Ra, if $Pr << 1$ ($\tau_{\kappa^*} << \tau_{\nu^*}$), τ_b is much smaller than τ_{ν^*} and vice versa when $Pr >> 1$. At large Pr the presence of any thermal disturbance cannot be communicated swiftly across the channel before viscous dissipation begins to act and therefore, the convective motion can no longer take place before viscous momentum diffusion has invaded the channel. As a result, any convective motion brought-in by the presence of a thermal perturbation cannot effectively complement the production and/or sustenance of streamwise motion. Overall, the effect of large Pr is to hamper the influence of any temperature perturbation on the lift-up mechanism. At low Prandtl numbers, however, any temperature disturbance can be swiftly conveyed across the channel and, since $\tau_b << \tau_{\nu^*}$, a convective motion can be set-up immediately which produces streamwise velocity through the lift-up mechanism.

Viscous forces become active at non-dimensional times $\mathcal{O}(Re)$ for all Pr and hence, in the stable region of the Re-Ra plane, any perturbation should decay at large time. Thus, in spite of the potential enhancement effect of the buoyancy-induced convection, at $t \sim \mathcal{O}(Re)$ any perturbation should eventually decay under the action of viscous forces. Viscous forces and thermal diffusion then lead to the dissipation of the convective

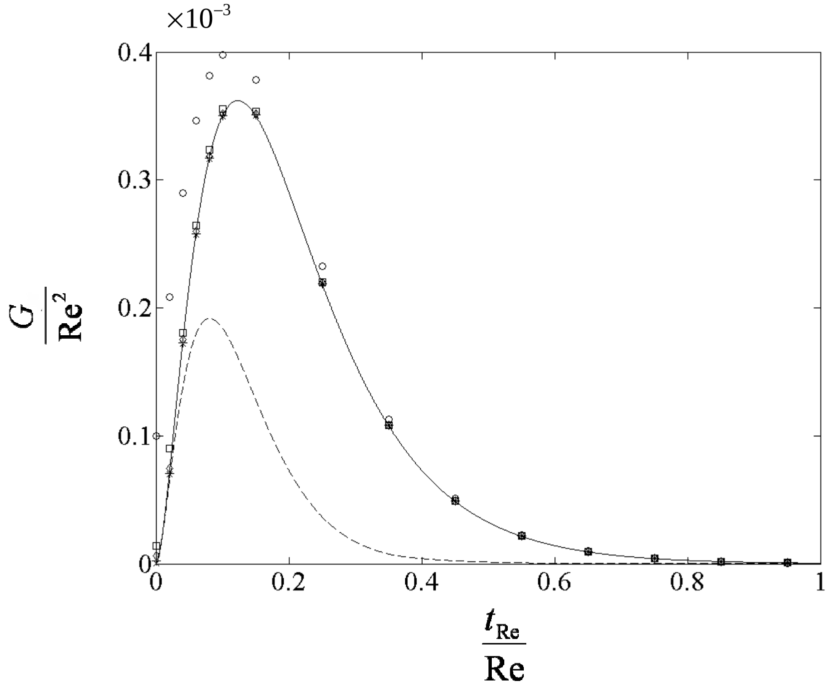

Figure 4.15: Optimal growth at different Reynolds numbers in RBP flow at $Ra = 1000$ and $Pr = 10^{-2}$ ($\alpha = 0$, $\beta = 1.8$): —— $Re = 5000$, × $Re = 2000$, + $Re = 1000$, ⋄ $Re = 500$, □ $Re = 300$, ○ $Re = 100$ and − − − $Ra = 0$, $Re = 5000$

motion. Furthermore, viscous diffusion also dissipates the so-formed streamwise streaks. The reason why t_{Re}^{max} increases only marginally with decreasing Prandtl number is owing to the fact that the increased production of streamwise streaks induced by the coupling between the convective motion and the lift-up mechanism is always overtaken by viscous dissipation at a finite non-dimensional time $t \sim \mathcal{O}(Re)$.

4.3.7 Effect of the norm $\|\boldsymbol{q}\|_\gamma$

In this section the transient growth computations for the class of norms $\gamma \neq \sqrt{|Ra_{h/2}|Pr}$ are considered. Only a few key results are discussed.

Let us consider the case when $\gamma = 1$. Figure 4.19 displays the effect of Rayleigh number on the optimal gain for the norm $\|\boldsymbol{q}\|_{\gamma=1}$. Results are shown for various streamwise wavenumbers at $\beta = 0$ (figure 4.19a) and $\beta = 1$ (figure 4.19b) and various spanwise wavenumbers at $\alpha = 0$ (figure 4.19c) and $\alpha = 1$ (figure 4.19d). The symbols correspond to different Rayleigh numbers (□ $Ra = 0$, ⋄ $Ra = 500$ and ○ $Ra = 1500$). In figures 4.19a and 4.19b these symbols collapse onto a single curve indicating that the Rayleigh number has very little effect on such perturbations. When $\alpha = 0$ and $\alpha = 1$, however, G_{max} is larger at large Rayleigh number for a range of spanwise wavenumbers. On comparing with the results for the case $\gamma = \sqrt{|Ra_{h/2}|Pr}$ (figure 4.2), the maximum optimal gain is larger for $\gamma = 1$. However, as in the case $\gamma = \sqrt{|Ra_{h/2}|Pr}$, the effect of Rayleigh number is primarily limited to streamwise-uniform and nearly-streamwise-uniform disturbances

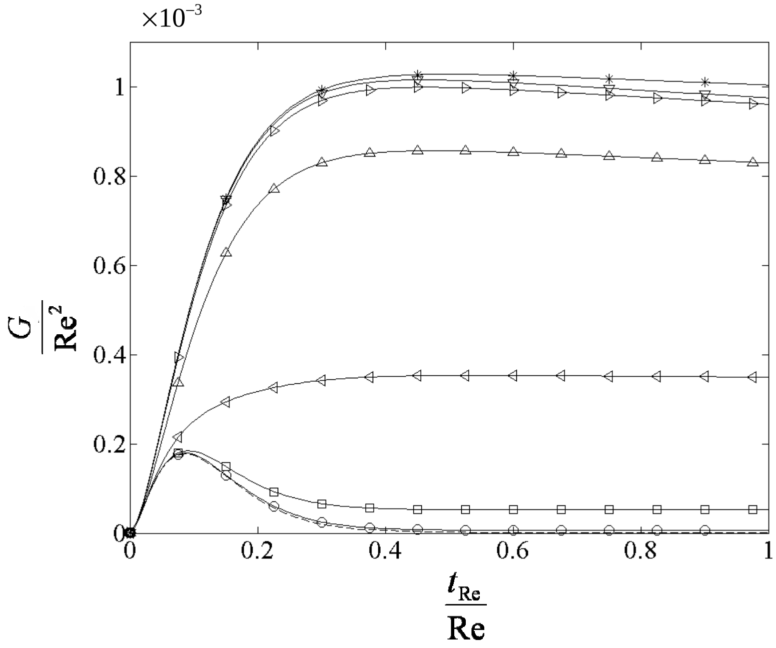

Figure 4.16: Optimal gain at various Prandtl numbers when $Re = 1000$, $\alpha = 0$ and $\beta = 1.558$ for $Ra = 0$ (− − −−) and $Ra = 1700$ (——): ∘ $Pr = 10^2$, □ $Pr = 10$, ◁ $Pr = 1$, △ $Pr = 10^{-1}$, ▷ $Pr = 10^{-2}$, ▽ $Pr = 10^{-3}$ and ∗ $Pr = 10^{-4}$.

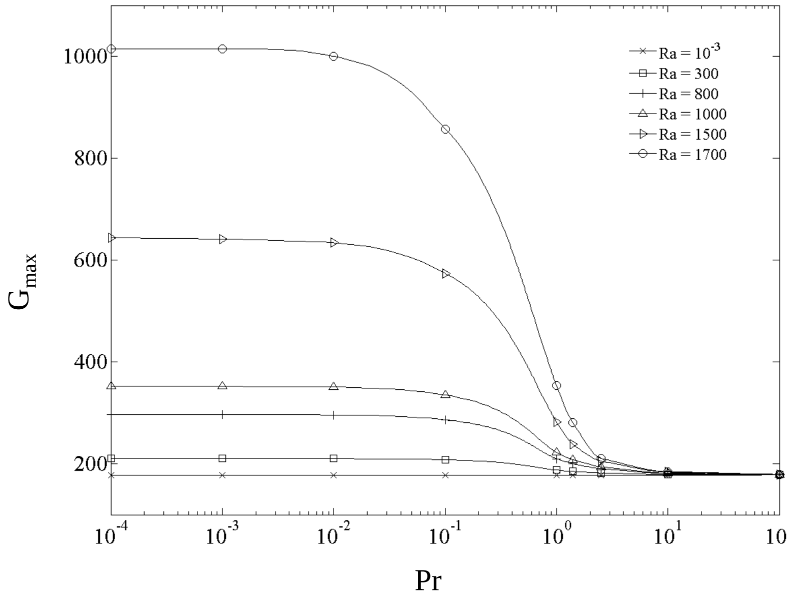

Figure 4.17: Effect of Prandtl number on G_{max} ($Re = 1000$, $\alpha = 0$ and $\beta = 1.558$)

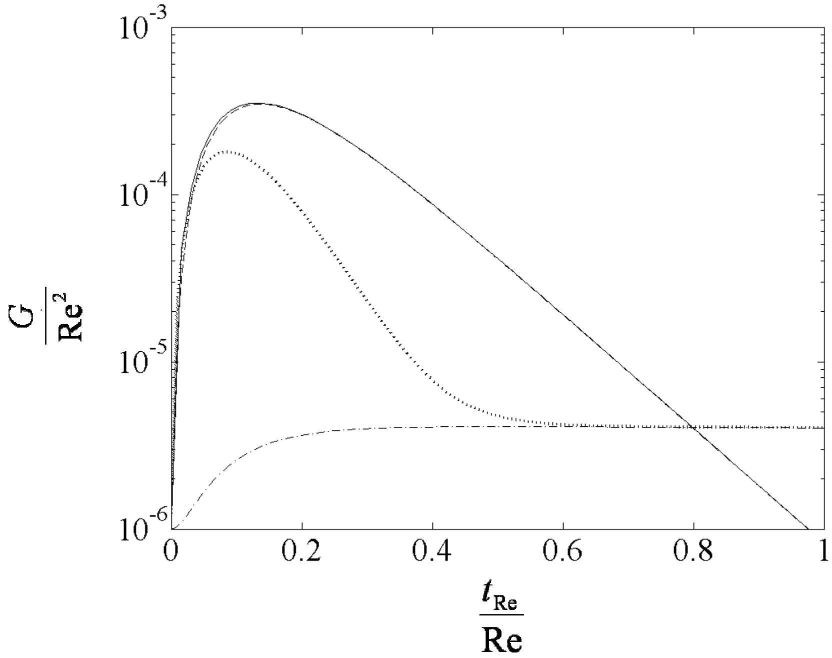

Figure 4.18: Effect of Prandtl number on the optimal gain curves ($Pr = 10^{-3}$ ——; $Pr = 10^2$ ······); Time evolution of the growth of perturbations $\frac{\|\boldsymbol{q}\|^2_{RB}}{\|\boldsymbol{q}_0\|^2_{RB}}$, where $\boldsymbol{q}_0$ is the normalised adjoint of the leading eigenmode ($Pr = 10^{-3}$ − − −; $Pr = 10^2$ − · ·−) at $Re = 1000$, $\alpha = 0$ and $\beta = 2.04$.

only.

Figure 4.20 shows the variations of optimal growth $G(t)$, with $\gamma = 1$, of streamwise-uniform disturbances for different Reynolds numbers ($\times$ $Re = 2000$, $\cdot$ $Re = 1000$, $+$ $Re = 500$, $\triangle$ $Re = 200$, $\circ$ $Re = 100$ and $\square$ $Re = 50$) at $Ra = 1300$ and $Pr = 1$. The continuous line and the dashed line correspond to the case $Re = 5000$ at $Ra = 0$ and $Ra = 1300$, respectively. When compared with the case of zero temperature difference (dashed line) the maximum transient growth is seen to be almost an order of magnitude larger at $Ra = 1300$. The collapse of all the symbols onto a single continuous curve ($Re = 5000$) as the Reynolds number increases, demonstrates that the large Reynolds number scaling holds also for the case $\gamma = 1$. This was observed for various non-zero values of the weight γ (data not shown). A comparison between figure 4.20 and figure 4.7 confirms that the optimal gain is larger when $\gamma = 1$. Note that, when $\gamma = \sqrt{|Ra_{h/2}| Pr}$, the coupled operator governing the wall-normal velocity component $\tilde{v}(y,t)$ and the temperature $\tilde{\theta}(y,t)$ for a streamwise-uniform perturbation ($\alpha = 0$) is normal with respect to the scalar product (2.42). If $Ra < Ra_c^{RB}$, its spectrum lies in the lower half-plane for all wavenumbers and hence, the Hille-Yosida theorem [72] states that the vector $\left[\tilde{v}(y,t), \tilde{\theta}(y,t)\right]^T$ cannot exhibit transient growth. Whereas, for any $\gamma \neq \sqrt{|Ra_{h/2}|\, Pr}$, this operator is no longer normal with respect to the scalar product (2.42). Since the spectrum lies in the lower half-plane for all wavenumbers, the increase in the optimal transient growth $G(t)$ when $\gamma \neq \sqrt{|Ra_{h/2}|\, Pr}$ can only come from the

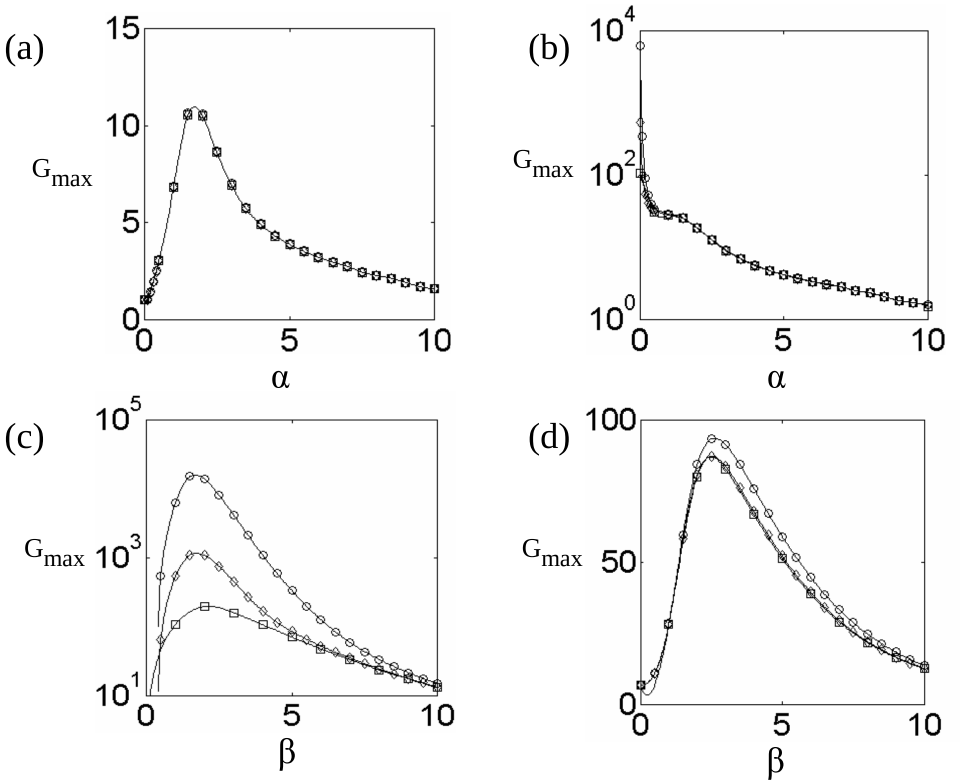

Figure 4.19: Optimal gain computations for the norm $\|\boldsymbol{q}\|_{\gamma}$ with $\gamma = 1$ at $Re = 1000$, $Pr = 1$ and □ $Ra = 0$, ◇ $Ra = 500$, ○ $Ra = 1500$: (a) $\beta = 0$, (b) $\beta = 1$, (c) $\alpha = 0$ and (d) $\alpha = 1$

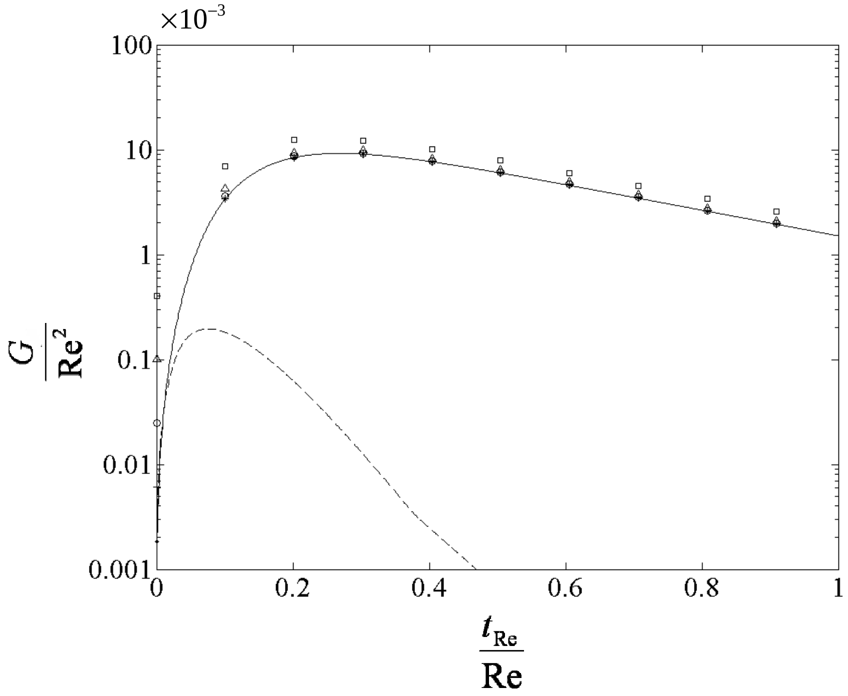

Figure 4.20: Optimal gain in RBP as computed for the norm $\|\boldsymbol{q}\|_\gamma$ for $\gamma = 1$ at $Ra = 1300$ ($\alpha = 0$, $\beta = 2.04$): —— $Re = 5000$, × $Re = 2000$, · $Re = 1000$, + $Re = 500$, △ $Re = 200$, ∘ $Re = 100$, □ $Re = 50$ and − − − $Ra = 0$, $Re = 5000$

non-normal block of system (2.37). Thus, when $\gamma \neq \sqrt{|Ra_{h/2}|\, Pr}$, $G(t)$ can be very large depending on the weight γ and the increase in $G(t)$ is due to the presence of off-diagonal terms corresponding to the forcing of wall-normal velocity by temperature perturbations, and vice versa, that render the governing equations explicitly non-normal.

Using the transformation

$$\begin{bmatrix} \hat{v}_A \\ \hat{\theta}_{*A} \\ \hat{\eta}_A \end{bmatrix} = \begin{bmatrix} 1 & 0 & 0 \\ 0 & \frac{|Ra_{h/2}|Pr}{\gamma} & 0 \\ 0 & 0 & 1 \end{bmatrix} \begin{bmatrix} \hat{v}_A \\ \frac{\gamma \hat{\theta}_{*A}}{|Ra_{h/2}|Pr} \\ \hat{\eta}_A \end{bmatrix}, \tag{4.37}$$

the adjoint system (2.43) for streamwise-uniform perturbations becomes

$$\begin{aligned} - i\omega^* \begin{bmatrix} -D_\beta^2 & 0 & 0 \\ 0 & 1 & 0 \\ 0 & 0 & 1 \end{bmatrix} \begin{bmatrix} \hat{v}_A \\ \frac{\gamma \hat{\theta}_{*A}}{|Ra_{h/2}|Pr} \\ \hat{\eta}_A \end{bmatrix} & \\ = \begin{bmatrix} Pr D_\beta^4 & -\beta^2 \left|Ra_{h/2}\right| Pr & -i\beta \left(RePr\right) \frac{dU_0}{dy} \\ -1 & -D_\beta^2 & 0 \\ 0 & 0 & -Pr D_\beta^2 \end{bmatrix} & \begin{bmatrix} \hat{v}_A \\ \frac{\gamma \hat{\theta}_{*A}}{|Ra_{h/2}|Pr} \\ \hat{\eta}_A \end{bmatrix}, \end{aligned} \tag{4.38}$$

where $D_\beta^2 = D^2 - \beta^2$. Thus, if $\boldsymbol{q}_{(RB)} = \left[\hat{v}_{(RB)}, \hat{\theta}_{(RB)}, 0\right]^T$ denotes the leading Rayleigh-

Bénard mode of the pure conduction problem, the adjoint of the leading eigenmode, for any arbitrary norm $\|\boldsymbol{q}\|_\gamma$, is given by

$$\boldsymbol{q}^{(\gamma)}_{A(1)} = \begin{bmatrix} \hat{v}_{(RB)} \\ \frac{1}{\gamma_0^2}\hat{\theta}_{(RB)} \\ 0 \end{bmatrix}, \text{ where } \gamma_0 = \frac{\gamma}{\sqrt{|Ra_{h/2}|\, Pr}}. \tag{4.39}$$

The dominant adjoint velocity and temperature eigenfunctions are seen to be identical to the Rayleigh-Bénard mode except for a multiplicative constant γ_0 in the temperature eigenfunction. Note that γ_0 depends on the type of norm through γ and it is equal to unity for the norm $\|\boldsymbol{q}\|_{RB}$ which makes the governing equations self-adjoint at $Re = 0$.

The response of RBP flow to various inputs at $Re = 1000$, $Ra = 1300$ and $Pr = 1$ is shown in figure 4.21. The continuous line denotes the optimal gain curve, the dashed line denotes the evolution of the optimal streamwise-uniform perturbation which grows up to G_{max}, the dot-dashed line denotes the response to the adjoint of the leading eigenmode (4.39) and the dotted line denotes the response to the Raleigh-Bénard mode of the pure conduction problem. Here, $G(t)$ has been computed based on the norm $\|\boldsymbol{q}\|_\gamma$ with $\gamma = 1$. All the initial conditions display transient growth and the dominant-adjoint-mode is amplified as much as the optimal input. Again, the adjoint of the leading eigenmode is a good approximation to the optimal initial condition. Note that the same conclusion was reached in section 4.3.5 where the norm $\|\boldsymbol{q}\|_{RB}$ was selected to compute the optimal response. This has also been verified for several values of γ (not presented here).

Thus, in general, *the dominant optimal transient growth mechanism, irrespective of the selected norm* $\|\boldsymbol{q}\|_\gamma$*, consists of two processes. The short-time optimal is due to the convective vortex motion, in the form of a "modified" Rayleigh-Bénard mode given by* (4.39)*, which acts in tandem with the inviscid lift-up mechanism, thereby resulting in large streamwise velocity streaks.* The long-time optimal simply consists of the transiently amplified Rayleigh-Bénard convection roll. It either decays or grows in time depending on the magnitude of Ra.

4.4 Conclusion

The effect of unstable thermal stratification on the linear stability properties of plane Poiseuille flow and plane Couette flow has been summarized for a wide range of Reynolds numbers Re and Rayleigh numbers Ra. The scaling laws for spanwise-uniform modes governing the dependence of the critical Rayleigh number and critical wavenumber on the corresponding critical Reynolds number have been obtained.

It was demonstrated that these flows are susceptible to large and sustained transient growth for a wide range of Reynolds and Rayleigh numbers at all Prandtl numbers. It was observed that unstable stratification, in RBP and RBC flows, increases the maximum optimal transient growth and maintains such a growth over a longer period of time. The maximum optimal transient growth G_{max} and the corresponding time at which it occurs t_{max} remain of the same order of magnitude as in the case of pure shear flows. In particular, the increase in G_{max} is more effective for streamwise-uniform disturbances. Unlike the computations by Sameen et. al. [74], spanwise-uniform disturbances were never observed to be the dominant optimal behavior in RBP flow at any Rayleigh or Prandtl number. The optimal spanwise wavenumber varies between the value for pure

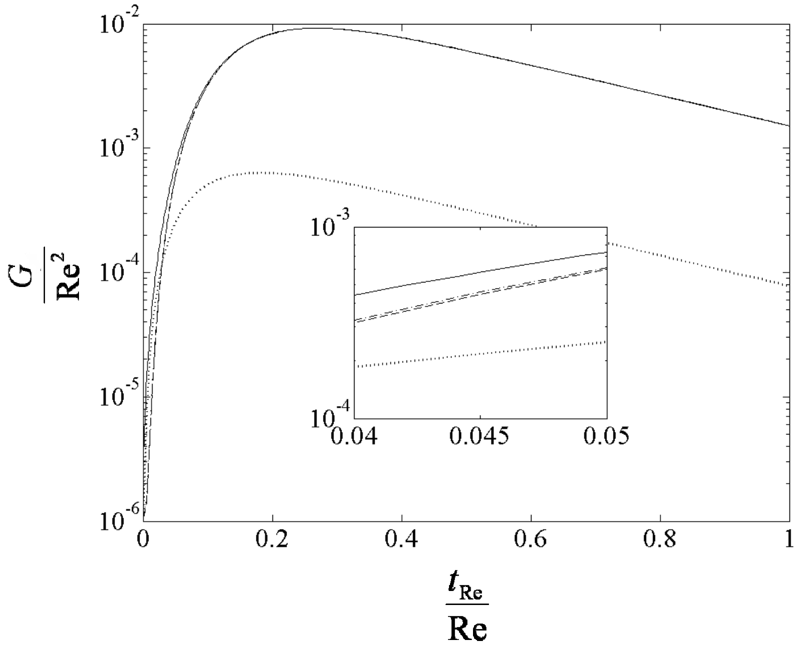

Figure 4.21: Optimal gain curve (———) and time evolution of the growth of perturbations $\frac{\|\boldsymbol{q}\|^2_{\gamma=1}}{\|\boldsymbol{q}_0\|^2_{\gamma=1}}$, where $\boldsymbol{q}_0$ is the normalized adjoint of the leading eigenmode (− − −−), the optimal initial condition corresponding to the maximum optimal gain (− · − · −) and the normalized Rayleigh-Bénard mode without its streamwise velocity component (· · · · · ·) at $Re = 1000$, $Ra = 1300$, $Pr = 1$, $\alpha = 0$ and $\beta = 2.04$ for $\gamma = 1$.

shear flow and that for the most unstable Rayleigh-Bénard convection mode as the Rayleigh number increases towards the critical Rayleigh number in RBI. The large Reynolds number scaling laws, such as, $G_{max} \propto Re^2$ and $t_{max} \propto Re$, were shown to remain valid in both RBP and RBC flows for all Rayleigh and Prandtl numbers.

The associated dominant growth mechanisms for the production of streamwise velocity streaks in the presence of an unstable temperature gradient were identified. A 3D vector model of the governing equations was used to demonstrate that the *short-time* behavior is governed by the inviscid lift-up mechanism and that the effect of Rayleigh number on this mechanism is secondary and negligible. By contrast, the optimal initial condition for the largest *long-time* response is given by the Rayleigh-Bénard mode without its streamwise velocity component. It was established that such a disturbance sets up streamwise-uniform convection rolls with no streamwise velocity component which act in tandem with the inviscid lift-up mechanism to produce and sustain streamwise motion in the form of streaks. A good approximation to the optimal initial condition was shown to be the dominant-adjoint-eigenmode, namely, the RB mode with zero streamwise velocity.

It was shown that the Prandtl number Pr of a Boussinesq fluid plays an important role in the coupling between temperature perturbations and the lift-up mechanism. At large Pr for a given Rayleigh number Ra, the convection rolls cannot take place before the viscous diffusion process and hence, the short-time optimal transient growth is similar to the case without cross-stream temperature gradient: the classical inviscid lift-up mechanism without thermal convective motion. Whereas, at small Pr, the convection rolls can effectively couple with the lift-up mechanism, thereby resulting in large transient growth.

An analysis of the direct and adjoint equations (2.37) and (2.43) revealed that the resulting transient growth depends on the type of norm selected. Thus, for the norm $\|\boldsymbol{q}\|_{\gamma}$, optimal growth $G(t)$ can vary largely as a function of γ and, when $\gamma \neq \sqrt{|Ra_{h/2}|\, Pr}$, the increase in $G(t)$ is due to the off-diagonal terms that render the governing equations explicitly non-normal. It was shown, however, that the dominant mechanism of transient growth is independent of the norm used to quantify it.

This study of the transient growth phenomenon in Rayleigh-Bénard-Poiseuille and Rayleigh-Bénard-Couette flows were summarized in an article which is under consideration by *Physics of Fluids* since early August 2011.

Part II

Consequences of the Squire transformation on 3D Optimal Perturbations

Chapter 5

Squire's transformation and 3D disturbances

"When you follow two separate chains of thought, Watson, you will find some point of intersection which should approximate the truth."

– Sherlock Holmes, The disappearence of Lady Francis Carfax
Sir Arthur Canon Doyle

5.1 Introduction

For over a decade now[76], the linear stability analysis of shear flows are followed in two parts, namely, modal stability analysis[45, 10, 18] and non-modal stability analysis[75]. The former analysis involves, the so-called method of normal modes, wherein the initial-value problem with linearized Navier-Stokes equations is reduced to an eigenvalue problem by considering modal solutions that grow, or decay, exponentially in time. Whereas the latter, and more general, analysis investigates the dynamics of disturbances over a finite-time horizon without assuming exponential time dependence. One of the main consequence of Squire's transformation [80] on the modal stability of $3D$ disturbances in parallel shear flows is Squire's theorem which states that for every $3D$ modal perturbation at a given Reynolds number, there is a $2D$ perturbation at a smaller Reynolds number with a larger growth rate. It is a celebrated result [10, 45, 18, 75] in the modal stability analysis as it justifies to reduce the analysis to $2D$ perturbations. In this part of the thesis, the role of Squire's transformation in the linear stability analysis of pure shear flows is revisited in order to understand its effect on (1) the Orr-Sommerfeld and Squire eigenmodes, (2) the Squire equation, (3) the arbitrary solution of the linearised Navier-Stokes equations, (4) the adjoint Orr-Sommerfeld and Squire eigenmodes and (4) the optimal growth for arbitrary wavenumbers and Reynolds numbers.

5.2 Governing equations

The evolution of three-dimensional infinitesimal disturbances in a shear flow is governed by the linearised Navier-Stokes equations with appropriate boundary conditions. For parallel shear flows infinite along streamwise (x-axis) and spanwise (z-axis) directions, wherein the base flow velocity vector is of the form $\vec{\boldsymbol{U}} = [U_0(y), 0, 0]^T$, these equations can be written independently for each streamwise and spanwise wavenumbers (denoted by α and β, respectively) as a system of two ordinary differential equations: the Orr-Sommerfeld equation for the normal-velocity $\tilde{v}(y,t)$ and the Squire equation for the normal-vorticity $\tilde{\eta}(y,t)$ [45, 18, 75]. The dimensionless version[5] of these equations is written as

$$-\frac{\partial}{\partial t}\begin{bmatrix} k^2 - D^2 & 0 \\ 0 & 1 \end{bmatrix} \boldsymbol{q} = \begin{bmatrix} L_{OS} & 0 \\ i\beta \frac{dU_0}{dy} & L_{SQ} \end{bmatrix} \boldsymbol{q}, \tag{5.1}$$

where $\boldsymbol{q} = [\tilde{v}(y,t), \tilde{\eta}(y,t)]^T$, $D = \frac{d}{dy}$ and $k^2 = \alpha^2 + \beta^2$. The symbols L_{OS} and L_{SQ}, respectively, denote the Orr-Sommerfeld and Squire operators:

$$L_{OS} = i\alpha U_0 \left(k^2 - D^2\right) + i\alpha \frac{d^2 U_0}{dy^2} + \frac{1}{Re}\left(k^2 - D^2\right)^2, \tag{5.2}$$

$$L_{SQ} = i\alpha U_0 + \frac{1}{Re}\left(k^2 - D^2\right), \tag{5.3}$$

where Re is the Reynolds number. The DiPrima-Habetler completeness theorem [17] applies to the system of equations governing the linear stability of parallel shear flows that are bounded in the cross-stream direction. Thus, it is possible to represent any solution of the LNS equations (5.1) as an eigenfunction expansion:

$$\begin{bmatrix} \tilde{v}(y,t) \\ \tilde{\eta}(y,t) \end{bmatrix} = \sum A_j \begin{bmatrix} \hat{v}_j(y) \\ \hat{\eta}_j^p(y) \end{bmatrix} \mathrm{e}^{-i\lambda_j t} + \sum B_j \begin{bmatrix} 0 \\ \hat{\eta}_j(y) \end{bmatrix} \mathrm{e}^{-i\mu_j t}, \tag{5.4}$$

where $\{\lambda_j\}$ are the eigenvalues of the Orr-Sommerfeld equation and $\{\mu_j\}$ are the eigenvalues of the Squire equation. The vector eigenfunctions in the first sum are referred to as the Orr-Sommerfeld modes (OS-modes), wherein the wall-normal velocity eigenfunctions $\{\hat{v}_j\}$ and wall-normal vorticity eigenfunctions $\{\hat{\eta}_j^p\}$ are the solutions, respectively, of the OS-equation

$$\left(i\lambda_j (k^2 - D^2) - L_{OS}\right) \hat{v}_j(y) = 0, \tag{5.5}$$

and the forced Squire equation

$$\left(i\lambda_j - L_{SQ}\right) \hat{\eta}_j^p(y) = i\beta \frac{dU_0}{dy} \hat{v}_j(y). \tag{5.6}$$

The eigenfunctions of the Squire equation have no contribution from the wall-normal velocity and are represented by $[0, \hat{\eta}_j(y)]^T$. They are the solutions of the homogeneous Squire's equation

$$\left(i\mu_j - L_{SQ}\right) \hat{\eta}_j(y) = 0, \tag{5.7}$$

and they form the so-called Squire modes (SQ-modes). The coefficients $\{A_j\}$ and $\{B_j\}$ are constants that can be determined from the initial conditions on the state variables. Equation (5.6) has a solution only if λ_j is not in the spectrum of L_{SQ}, i.e all λ_j's are different from μ_j's. This condition can be assumed except for a set of Reynolds numbers and wavenumbers of zero measure.

---

[5] The non-dimensional time, wall-normal velocity and wall-normal vorticity variables are based on some characteristic length scale, and advective velocity scale from the base flow. They should not be confused with the variables in the previous chapters.

5.3 Consequences on the eigenfunctions

When $\alpha \neq 0$, it is well-known that the OS equation (5.5) and the homogeneous part of the SQ equations (5.7) are amenable to the Squire transformation whereby their respective eigenvalue problem at any α, β and Re can be reduced to the case when $\beta = 0$. According to the transformation, when $\alpha \neq 0$, the eigenvalue problem for $\hat{v}_j(y)$ of OS-modes and $\hat{\eta}_j(y)$ of SQ-modes at any α, β and Re reduces to the $2D$ case $\alpha_{2D} = \sqrt{\alpha^2+\beta^2}$, $\beta_{2D} = 0$ and $Re_{2D} = \alpha Re/\sqrt{\alpha^2+\beta^2}$. This implies that

$$\lambda_j(\alpha,\beta,Re) = \frac{\alpha}{\sqrt{\alpha^2+\beta^2}}\,\lambda_j^{2D}(\alpha_{2D},0,Re_{2D}), \tag{5.8}$$

$$\hat{v}_j(y;\alpha,\beta,Re) = \hat{v}_j^{2D}(y;\alpha_{2D},0,Re_{2D}), \tag{5.9}$$

for the OS-modes and

$$\mu_j(\alpha,\beta,Re) = \frac{\alpha}{\sqrt{\alpha^2+\beta^2}}\,\mu_j^{2D}(\alpha_{2D},0,Re_{2D}), \tag{5.10}$$

$$\hat{\eta}_j(y;\alpha,\beta,Re) = \hat{\eta}_j^{2D}(y;\alpha_{2D},0,Re_{2D}), \tag{5.11}$$

for the SQ-modes. To the author's best knowledge the implications of the Squire transformation on the wall-normal vorticity eigenfunction of OS-modes $\hat{\eta}_j^p(y)$ has not been yet discussed in the literature. The extension of the Squire transformation to equation (5.6) of $\hat{\eta}_j^p(y)$ gives

$$\left[i\left(\lambda_j^{2D} - \alpha_{2D}U_0\right) - \frac{1}{Re_{2D}}\left(\alpha_{2D}^2 - D^2\right)\right]\hat{\eta}_j^{p2D}(y) = i\frac{dU_0}{dy}\hat{v}_j^{2D}(y), \tag{5.12}$$

where $\hat{\eta}_j^{p2D}(y)$ is the solution of the $2D$ Squire equation forced at $\lambda_j^{2D}(\alpha_{2D},0,Re_{2D})$ and is related to $\hat{\eta}_j^p$ as

$$\hat{\eta}_j^p(y;\alpha,\beta,Re) = \beta\frac{\sqrt{\alpha^2+\beta^2}}{\alpha}\hat{\eta}_j^{p2D}(y;\alpha_{2D},0,Re_{2D}). \tag{5.13}$$

Since, for the 2D perturbation ($\beta = 0$) ,λ_j^{2D} is not in the spectrum of L_{SQ}, this equation has a solution. Firstly, as a consequence of Squire's transformation, the solution (5.4) of the direct equations (5.1) for arbitrary α, β and Re can be deduced simply from two simple cases: (1) at $\alpha = 0$, β, Re and (2) at α_{2D}, $\beta_{2D} = 0$, Re_{2D}. Secondly, the Squire transformation implies that by decreasing α at a constant $\alpha_{2D} = k = \sqrt{\alpha^2+\beta^2}$ and Re_{2D} the wall-normal vorticity in the OS-mode diverges as $\frac{1}{\alpha}$ while the wall-normal velocity remains constant. This is another manifestation of the lift-up mechanism in $3D$ disturbances whereby $\hat{\eta}_j$ is a passive response to the $\hat{v}_j$ forcing in the OS-mode. Note that $\alpha Re = \alpha_{2D}Re_{2D}$ and, thus, decreasing the streamwise wavenumber α is equivalent to increasing the flow Reynolds number Re at a constant Re_{2D} and α_{2D}. This implies that, for the same initial condition with zero wall-normal vorticity, the solution (5.4) to the initial value problem (5.1) corresponding to all $\alpha \neq 0$, β and Re at a given Re_{2D} and α_{2D} can be rewritten as

$$\begin{aligned}\begin{bmatrix}\tilde{v}(y,t)\\ \tilde{\eta}(y,t)\end{bmatrix} &= \sum A_j \begin{bmatrix}\hat{v}_j^{2D}(y)\\ \left(\frac{\beta Re}{Re_{2D}}\right)\hat{\eta}_j^{p2D}(y)\end{bmatrix}\exp\left(-iRe_{2D}\lambda_j^{2D}\frac{t}{Re}\right)\\ &+\left(\frac{\beta Re}{Re_{2D}}\right)\sum B_j^{'}\begin{bmatrix}0\\ \hat{\eta}_j^{2D}(y)\end{bmatrix}\exp\left(-iRe_{2D}\mu_j^{2D}\frac{t}{Re}\right).\end{aligned} \tag{5.14}$$

Here, A_j's and $B_j^{'}$'s are independent of the streamwise wavenumber α, β and Re. When Re increases (or α decreases), the response to such an initial condition is slower since the time variable is rescaled by Re in the exponential terms. The amplitude of the Squire modes needed to cancel the wall-normal vorticity initially increases as the Reynolds number and thereby offering the possibility of transient growth. It can be seen that the short-time expansion of the wall-normal vorticity in the solution (5.14), for the same initial condition, is

$$\tilde{\eta}(y,t) \sim -i\beta t \sum A_j \hat{\eta}_j^{p2D}(y) \left(\lambda_j^{2D} - \mu_j^{2D}\right). \tag{5.15}$$

for all $t << Re$. When Re_{2D} and α_{2D} are given, for disturbances with arbitrary α and β , this is a Reynolds-number-independent short-term growth in the wall-normal vorticity similar to the classical inviscid lift-up mechanism that usually attributed streamwise-uniform disturbances. The results (5.14) and (5.15) are applicable for all non-zero streamwise wavenumbers, spanwise wavenumbers and Reynolds numbers such that $\alpha Re = \alpha_{2D} Re_{2D}$.

Conventionally, the optimal growth characteristics are obtained by solving equations (5.1) for an initial disturbance field that would give rise to the maximum possible growth at a particular time horizon t and it is defined by the gain function

$$G(t;\alpha,\beta,Re) = \max_{\forall \boldsymbol{q}_0 \neq \boldsymbol{0}} \frac{\|\boldsymbol{q}(t)\|^2}{\|\boldsymbol{q}_0\|^2}, \tag{5.16}$$

which is referred to as the optimal gain, i.e. the maximum possible growth at some time t over all possible non-zero initial conditions. The commonly used positive-definite norm of the growth of disturbances is the kinetic energy. Such a norm can be defined using the scalar product

$$\langle \boldsymbol{q}_1,\ \boldsymbol{q}_2 \rangle = \int_{-1}^{1} \boldsymbol{q}_2^H \mathbf{M} \boldsymbol{q}_1 dy, \tag{5.17}$$

where ^{H} represents the conjugate-transpose of a matrix and

$$\mathbf{M} = \begin{bmatrix} k^{-2} & 0 \\ 0 & 1 \end{bmatrix}. \tag{5.18}$$

The kinetic energy of the disturbances, in terms of wall-normal velocity and wall-normal vorticity, reads

$$\|\boldsymbol{q}\|^2 = \frac{1}{2}\int_{-1}^{1} \left[|\hat{v}|^2 + \frac{1}{k^2}\left(|D\hat{v}|^2 + |\hat{\eta}|^2 \right) \right] dy. \tag{5.19}$$

With respect to the scalar product (5.17), the adjoint equations are derived to be [75]

$$-\frac{\partial}{\partial t}\begin{bmatrix} k^2 - D^2 & 0 \\ 0 & 1 \end{bmatrix} \boldsymbol{q}^A = \begin{bmatrix} L_{OS}^A & -i\beta \frac{dU_0}{dy} \\ 0 & L_{SQ}^A \end{bmatrix} \boldsymbol{q}^A, \tag{5.20}$$

where L_{OS}^A and L_{SQ}^A are the adjoint-Orr-Sommerfeld and adjoint-Squire operators, respectively [75],

$$L_{OS}^A = -i\alpha U_0 \left(k^2 - D^2\right) + 2i\alpha \frac{dU_0}{dy} D + \frac{1}{Re}\left(k^2 - D^2\right)^2, \tag{5.21}$$

$$L_{SQ}^{A} = -i\alpha U_0 + \frac{1}{Re}\left(k^2 - D^2\right), \tag{5.22}$$

and the adjoint state vector is $\boldsymbol{q}^A = [\tilde{\xi}(y,t), \tilde{\zeta}(y,t)]^T$. Here, $\tilde{\xi}(y,t)$ and $\tilde{\zeta}(y,t)$ denote the adjoint wall-normal velocity and wall-normal vorticity components, respectively. Observe that, in the adjoint linear operator (5.20), it is the wall-normal vorticity $\tilde{\zeta}(y,t)$ that forces the adjoint wall-normal velocity equation whereas the adjoint Squire equation is independent of the adjoint wall-normal velocity. The advantage of the adjoint problem is that the spectrum of the adjoint OS operator L_{OS}^A is the complex conjugate of the spectrum of the direct OS operator L_{OS} and similarly for the SQ operator L_{SQ}. Thus, the solution to the adjoint equations can be written as an infinite sum of adjoint eigenfunctions:

$$\begin{bmatrix} \tilde{\xi}(y,t) \\ \tilde{\zeta}(y,t) \end{bmatrix} = \sum P_j \begin{bmatrix} \hat{\xi}_j(y) \\ 0 \end{bmatrix} \mathrm{e}^{-i\lambda_j^* t} + \sum Q_j \begin{bmatrix} \hat{\xi}_j^p(y) \\ \hat{\zeta}_j(y) \end{bmatrix} \mathrm{e}^{-i\mu_j^* t}, \tag{5.23}$$

where the coefficients $\{P_j\}$ and $\{Q_j\}$ are constants and * on the eigenvalues denotes the complex conjugate[6]. The vector eigenfunctions of L_{OS}^A correspond to zero wall-normal vorticity i.e., the adjoint OS-modes are of the form $[\hat{\xi}_j, 0]^T$. Conversely, the adjoint SQ modes have a non-zero wall-normal velocity corresponding to the forcing of the adjoint OS operator by the off-diagonal term $-i\beta\frac{dU_0}{dy}$ in the adjoint equation (5.20) and they read $[\hat{\xi}_j^p, \hat{\zeta}_j]^T$.

Remarkably, the Squire transformation also applies to the homogeneous part of the adjoint Orr-Sommerfeld equation and to the adjoint Squire equation. Thus, a $3D$ adjoint OS-mode at any α, β and Re, is related to a $2D$ adjoint OS-mode at $\alpha_{2D} = \sqrt{\alpha^2 + \beta^2}$, $\beta_{2D} = 0$ and Re_{2D} via the transformation

$$\lambda_j^*(\alpha, \beta, Re) = \frac{\alpha}{\sqrt{\alpha^2 + \beta^2}}\ \lambda_j^{*2D}(\alpha_{2D}, 0, Re_{2D}), \tag{5.24}$$

$$\hat{\xi}_j(y; \alpha, \beta, Re) = \hat{\xi}_j^{2D}(y; \alpha_{2D}, 0, Re_{2D}). \tag{5.25}$$

In order to complete the general solution (5.23), it only remains to find the particular integrals $\hat{\xi}_j^p(y)$ of the adjoint OS equation forced by $\hat{\zeta}_j(y)$ for $\beta \neq 0$. This component of the adjoint SQ-mode can be deduced from a similar extension of the Squire transformation discussed above, applied here to the forced adjoint OS equation. Thus, as a consequence of the Squire transformation, the adjoint SQ-mode at any α, β and Re reads

$$\hat{\xi}_j^p(y; \alpha, \beta, Re) = \beta\frac{\sqrt{\alpha^2 + \beta^2}}{\alpha}\hat{\xi}_j^{p2D}(y; \alpha_{2D}, 0, Re_{2D}), \tag{5.26}$$

$$\hat{\zeta}_j(y; \alpha, \beta, Re) = \hat{\zeta}_j^{2D}(y; \alpha_{2D}, 0, Re_{2D}), \tag{5.27}$$

where $\hat{\xi}_j^{p2D}$ satisfies the two-dimensional adjoint Orr-Sommerfeld equation forced at $\mu_j^{*2D}(\alpha_{2D}, 0, Re_{2D})$ such that

$$\left[i(\mu_j^{*2D} + \alpha_{2D}U_0)(\alpha_{2D}^2 - D^2) - 2i\alpha_{2D}\frac{dU_0}{dy}D - \frac{1}{Re_{2D}}(\alpha_{2D}^2 - D^2)^2\right]\hat{\xi}_j^{p2D}(y) = -i\frac{dU_0}{dy}\hat{\zeta}_j^{2D}(y), \tag{5.28}$$

---

[6] Note that, throughout this chapter, * denotes complex conjugate

and

$$\mu_j^*(\alpha, \beta, Re) = \frac{\alpha}{\sqrt{\alpha^2+\beta^2}}\, \mu_j^{*2D}(\alpha_{2D}, 0, Re_{2D}). \tag{5.29}$$

Note that the solution $\hat{\xi}_j^{p2D}$ of the $2D$ adjoint OS equation (5.28) exists because μ^{*2D} is not present in the spectrum of the $2D$ adjoint OS operator.

In general, the solution of the adjoint system (5.20) for arbitrary α, β and Re can also be deduced simply from two simple cases: (1) at $\alpha = 0$, β, Re and (2) at α_{2D}, $\beta_{2D} = 0$, Re_{2D}.

5.4 Consequences on long-time optimal gains

The definition of the adjoint problem allows for a simple resolution of equation (5.4), since for any initial condition $\boldsymbol{q}_0$, the coefficients in the eigenfunction expansion (5.4) given by:

$$A_j = \frac{\langle \boldsymbol{q}_0, \begin{bmatrix}\hat{\xi}_j(y)\\ 0\end{bmatrix}\rangle}{\langle \begin{bmatrix}\hat{v}_j(y)\\ \hat{\eta}_j^p(y)\end{bmatrix}, \begin{bmatrix}\hat{\xi}_j(y)\\ 0\end{bmatrix}\rangle} \quad \& \quad B_j = \frac{\langle \boldsymbol{q}_0, \begin{bmatrix}\hat{\xi}_j^p(y)\\ \hat{\zeta}_j(y)\end{bmatrix}\rangle}{\langle \begin{bmatrix}0\\ \hat{\eta}_j(y)\end{bmatrix}, \begin{bmatrix}\hat{\xi}_j^p(y)\\ \hat{\zeta}_j(y)\end{bmatrix}\rangle}. \tag{5.30}$$

For $t >> 1$, the long-time response is dominated by the leading eigenmode with a non-zero co-efficient in the solution (5.4). The leading eigenmode, in general, can either be the OS-mode or the SQ-mode. Consider the case when the long-time response is due to the leading OS-mode, say, $\phi_1 = [\hat{v}_1(y), \hat{\eta}_1^p(y)]^T$. Then at $t >> 1$,

$$\boldsymbol{q}\,(t) \sim A_1 \phi_1 \mathrm{e}^{-i\lambda_1 t}, \tag{5.31}$$

and maximizing the long-time gain reduces to maximizing the coefficient A_1. Using expression (5.30), it is observed that the large-time gain is achieved by taking as an initial condition, the leading adjoint OS-mode, say, $\phi_1^A = [\hat{\xi}_1(y), 0]^T$ and hence the gain reads

$$G(\alpha, \beta, t; Re) \sim \frac{\|\phi_1\|^2 \left\|\phi_1^A\right\|^2}{\left|\langle \phi_1,\ \phi_1^A\rangle\right|^2} \left|\mathrm{e}^{-i\lambda_1 t}\right|^2, \tag{5.32}$$

where λ_1 is the dominant eigenvalue of OS equation. Let $G_\infty^{OS} = \frac{\|\phi_1\|^2 \left\|\phi_1^A\right\|^2}{\left|\langle \phi_1,\ \phi_1^A\rangle\right|^2}$ denote the resulting extra gain, taking the adjoint OS-mode ϕ_1^A as the initial condition, compared to the gain $\left|\mathrm{e}^{-i\lambda_1 t}\right|^2$, achieved by choosing as initial condition the direct OS-mode ϕ_1. Similarly, in the case where the leading eigenmode is the SQ-mode, say, $\psi_1 = [0, \hat{\eta}_1^p(y)]^T$, let $G_\infty^{SQ} = \frac{\|\psi_1\|^2 \left\|\psi_1^A\right\|^2}{\left|\langle \psi_1,\ \psi_1^A\rangle\right|^2}$ denote the extra gain compared to the gain $\left|\mathrm{e}^{-i\mu_1 t}\right|^2$, achieved by choosing as initial condition the direct SQ-mode ψ_1. In this instance, μ_1 is the dominant eigenvalue of the Squire equation and $\psi_1^A = [\hat{\xi}_1^A(y), \hat{\zeta}_1(y)]^T$ is the adjoint of the leading SQ-mode.

5.4.1 Case (1): Streamwise-uniform disturbances ($\alpha = 0$)

Under this assumption, the direct OS equation and the homogeneous part of the adjoint OS equations become identical. So, $\hat{v}_j(y) = \hat{\xi}_j(y)$ and the leading direct and adjoint OS-modes can be rewritten as, respectively,

$$\phi_1 = \phi_1^v + \phi_1^{\eta^p}, \tag{5.33}$$

$$\phi_1^A = \phi_1^v, \tag{5.34}$$

where $\phi_1^v = [\hat{v}_1(y), 0]^T$ and $\phi_1^{\eta^p} = [0, \hat{\eta}_1^p(y)]^T$. If the leading eigenmode is an OS-mode, the long-time optimal gain becomes

$$G_\infty^{OS}(0, \beta; Re) = \left(1 + \frac{\left\|\phi_1^{\eta^p}\right\|^2}{\left\|\phi_1^v\right\|^2}\right). \tag{5.35}$$

Since the SQ operator is self-adjoint, the leading direct and adjoint SQ-modes can be rewritten as

$$\psi_1 = \psi_1^\eta, \tag{5.36}$$

$$\psi_1^A = \psi_1^{\xi^p} + \psi_1^\eta, \tag{5.37}$$

where $\psi_1^\eta = [0, \hat{\eta}_1(y)]^T$ and $\psi_1^{\xi^p} = [\hat{\xi}_1^p(y), 0]^T$. Thus, if the leading eigenmode is a SQ-mode, the long-time optimal growth becomes

$$G_\infty^{SQ}(0, \beta; Re) = \left(1 + \frac{\left\|\psi_1^{\xi^p}\right\|^2}{\left\|\psi_1^\eta\right\|^2}\right). \tag{5.38}$$

The expressions (5.35) and (5.38) represent the extra optimal gain associated with the lift-up mechanism resulting from the leading OS-mode and SQ-mode, respectively. They are functions of β and Re. If a Gustavsson-type [31] scaling is used for the forced Squire equation and the forced adjoint Orr-Sommerfeld equation at $\alpha = 0$:

$$\bar{t} = \frac{t}{Re}, \tag{5.39}$$

$$\bar{v}(y) = \hat{v}(y), \;\; \bar{\eta}(y) = \frac{\hat{\eta}(y)}{\beta Re}, \tag{5.40}$$

$$\bar{\xi}(y) = \frac{\hat{\xi}(y)}{\beta Re}, \;\; \bar{\zeta}(y) = \hat{\zeta}, \tag{5.41}$$

whereby the state variables can be rendered independent of Reynolds number. The gains (5.35) and (5.38) can then be rewritten as

$$G_\infty^{OS}(0, \beta; Re) = \left(1 + \beta^2 Re^2 \frac{\left\|\bar{\phi}_1^{\eta^p}\right\|^2}{\left\|\bar{\phi}_1^v\right\|^2}\right), \tag{5.42}$$

and

$$G_{\infty}^{SQ}(0,\beta;Re) = \left(1 + \beta^2 Re^2 \frac{\left\|\bar{\psi}_1^{\xi^p}\right\|^2}{\left\|\bar{\psi}_1^{\eta}\right\|^2}\right). \tag{5.43}$$

Note that the norms are independent of the Reynolds number.

5.4.2 Case (2): $3D$ long-time optimal perturbations

Consider now case (2): $\alpha \neq 0$. As a consequence of Squire's transformation, the direct and adjoint OS-modes can be written as, respectively,

$$\phi_1 = \phi_1^{v2D} + \left(\frac{\beta Re}{Re_{2D}}\right)\phi_1^{\eta^{p2D}}, \tag{5.44}$$

$$\phi_1^A = \phi_1^{\xi 2D}, \tag{5.45}$$

where $\phi_1^{v2D} = [\hat{v}_1^{2D}(y), 0]^T$, $\phi_1^{\eta^p} = [0, \hat{\eta}_1^{p2D}(y)]^T$ and $\phi_1^{\xi 2D} = [\hat{\xi}_1^{2D}(y), 0]^T$. The superscript $2D$ represents the eigenfunctions at α_{2D}, $\beta_{2D} = 0$ and Re_{2D}. Note that $\hat{\eta}_1^{p2D}(y)$ is the particular integral of the rescaled-Squire equation (5.12) which depends only on Re_{2D} and α_{2D}. Using (5.44) and (5.45), the long-time optimal growth (5.31) can be split into two contributions according to the expression

$$G_{\infty}^{OS}(\alpha,\beta;Re) = G_{\infty}^{OS}(\alpha_{2D},0;Re_{2D})\left(1 + \frac{\beta^2 Re^2}{Re_{2D}^2}\frac{\left\|\phi_1^{\eta^{p2D}}\right\|^2}{\left\|\phi_1^{v2D}\right\|^2}\right), \tag{5.46}$$

where $G_{\infty}^{OS}(\alpha_{2D},0;Re_{2D})$ is the gain that would be obtained in the $2D$ case and which is known to result from the Orr-mechanism [65] and the second term on the $R.H.S$ is precisely the extra gain from the $3D$ effect, the contribution to the optimal transient growth arising from the lift-up mechanism [21, 53, 72] due to the forcing of the wall-normal vorticity by the wall-normal velocity. Note that $G_{\infty}^{OS}(\alpha_{2D},0,t;Re_{2D}) \sim \mathcal{O}(1)$ while the second term is $\mathcal{O}(\beta^2 Re^2/Re_{2D}^2)$. Similarly if the leading eigenmode is a SQ-mode, the long-time optimal growth becomes

$$G_{\infty}^{SQ}(\alpha,\beta;Re) = \left(1 + \frac{\beta^2 Re^2}{Re_{2D}^2}\frac{\left\|\psi_1^{\xi^{p2D}}\right\|^2}{\left\|\psi_1^{\eta 2D}\right\|^2}\right). \tag{5.47}$$

In this instance, $\psi_1 = \psi_1^{\eta 2D} = [0, \hat{\eta}_1^{2D}(y)]^T$, $\psi_1^{\xi^{p2D}} = [\hat{\xi}_1^{p}(y), 0]^T$ and $\psi_1^A = (\beta Re/Re_{2D})\,\psi_1^{\xi^{p2D}}$ $+\ \psi_1^{\eta 2D}$ (since the $2D$ SQ operator is self-adjoint). The particular integral $\hat{\xi}_1^{p2D}(y)$ of the $2D$ adjoint OS equation is given by the equation (5.28) which is dependent on α_{2D} and Re_{2D} only.

Note that equations (5.42), (5.43), (5.46) and (5.47) are derived for $t >> 1$. They are valid irrespective of the base flow, Reynolds number and wavenumber.

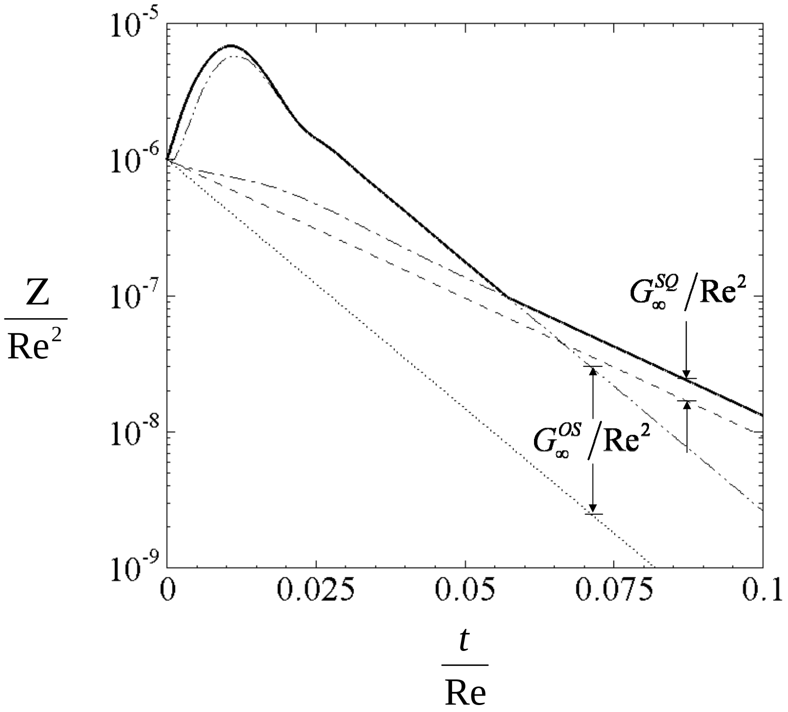

Figure 5.1: Direct computations in Plane Poiseuille flow for $\alpha = 1$, $\beta = 0$ and $Re = 1000$: Temporal variation of optimal gain (——) and the growth of perturbations $Z = \frac{\|q(t)\|^2}{\|q(t_0)\|^2}$ for various normalized initial conditions: adjoint of the leading OS-mode ($-\cdot\cdot-$), adjoint of the leading SQ-mode ($-\cdot-\cdot$), leading OS-mode ($\cdots\cdots$) and leading SQ-mode ($---$) at $Re_{2D} = 1000$ and $\alpha_{2D} = 1$, $\beta_{2D} = 0$.

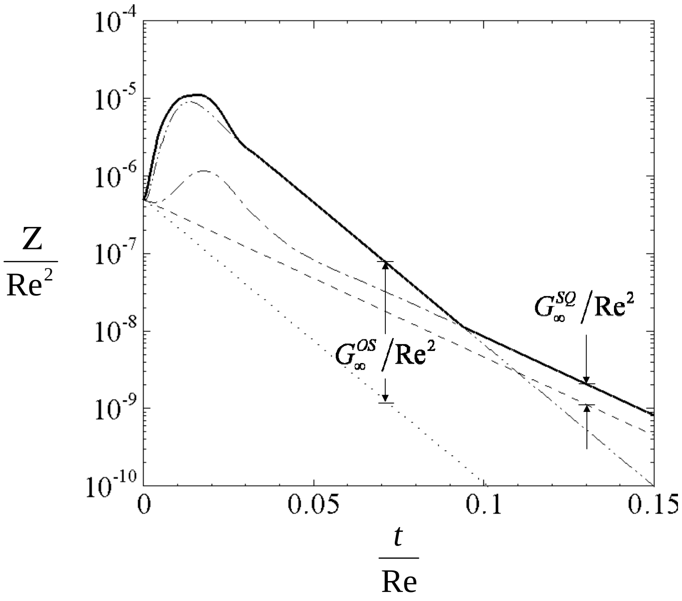

Figure 5.2: Direct computations in Plane Poiseuille flow for $\alpha = \frac{1}{\sqrt{2}}$, $\beta = \frac{1}{\sqrt{2}}$ and $Re = 1414.2$: Same as figure 5.1.

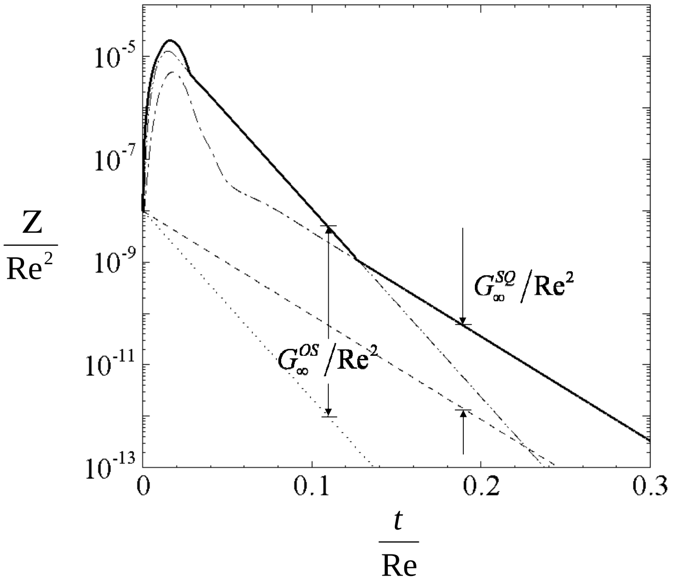

Figure 5.3: Direct computations in Plane Poiseuille flow for $\alpha = 0.1$, $\beta = 0.9949$ and $Re = 10^4$: Same as figure 5.1.

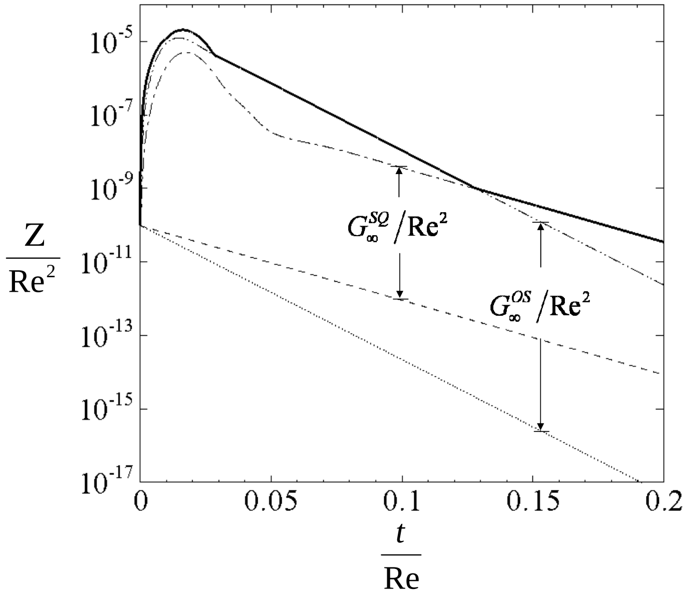

Figure 5.4: Direct computations in Plane Poiseuille flow for $\alpha = 0.01$, $\beta = 0.99995$ and $Re = 10^5$: Same as figure 5.1.

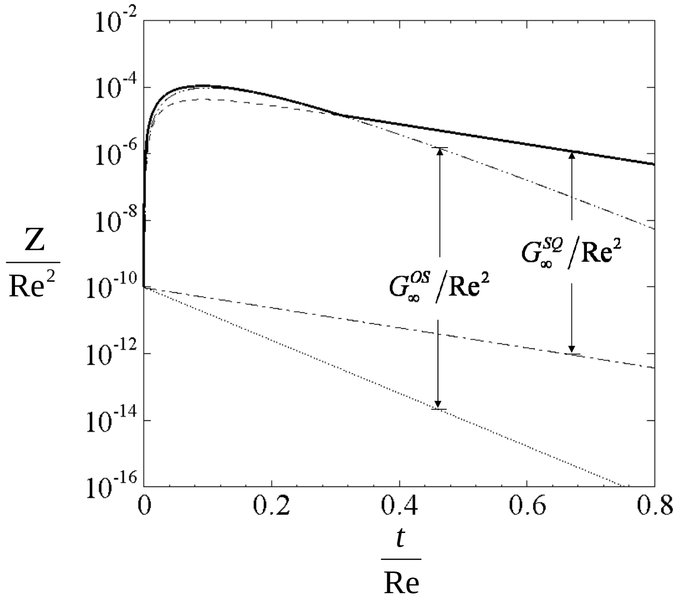

Figure 5.5: Direct computations in Plane Poiseuille flow for when $Re = 10^5$ and $\alpha = 0$, $\beta = 1$: Same as figure 5.1

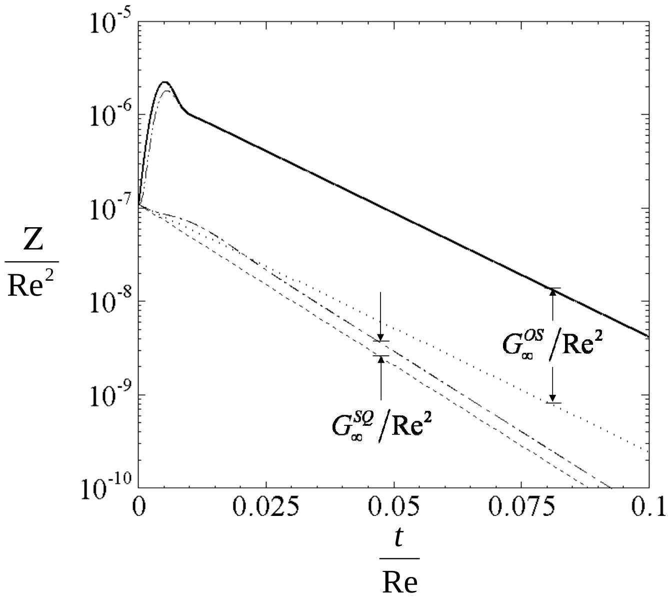

Figure 5.6: Plane Poiseuille flow at $Re_{2D} = 3000$ and $\alpha_{2D} = 1$, $\beta_{2D} = 0$: Same as figure 5.1 when $\alpha = 1$, $\beta = 0$ and $Re = 3000$.

5.5 Discussion

Figures 5.1−5.3 display, for different streamwise and spanwise wavenumbers, the time evolution of the logarithm of optimal transient growth (——) as defined in equation (5.16) and the response $Z = \frac{\|\boldsymbol{q}(t)\|^2}{\|\boldsymbol{q}(t_0)\|^2}$ for various normalized initial conditions: adjoint of the leading OS-mode (− · ·−), adjoint of the leading SQ-mode (− · −·), leading OS-mode (· · · · ·) and leading SQ-mode (− − −). These results were obtained for the case of plane Poiseuille flow. The long-time optimal gains G_∞^{OS} and G_∞^{SQ} were computed using the expressions (5.46) and (5.47), respectively. In figures 5.1−5.3, $Re_{2D} = 1000$ and $\alpha_{2D} = 1$ while α and Re vary with respect to β such that $\alpha^2 + \beta^2 = \alpha_{2D}^2 = 1$ and $\alpha Re = \alpha_{2D} Re_{2D} = 1000$. For all α and β values shown here, the responses to the adjoint of the leading OS and SQ modes display transient growth whereas the responses to the leading OS and SQ modes exhibit exponential decay $e^{2\Im(\lambda_1)t}$ and $e^{2\Im(\mu_1)t}$, respectively (here, $\Im(\lambda)$ represents the imaginary part of λ). At $t >> 1$, the gain Z corresponding to the adjoint of the leading SQ-mode coincides with the continuous curve representing the optimal transient growth and Z of the adjoint of the leading OS-mode coincides with the optimal growth curve at intermediate time steps in all the cases. Irrespective of α and β shown here, the large-time optimal response due to the adjoint OS-mode G_∞^{OS} is observed to be greater than the large-time optimal response due to the adjoint SQ-mode G_∞^{SQ}. Note that it is the leading-adjoint OS-mode that displays a large growth, as much as the optimal growth, before eventually decaying. If t^* represents the time at which the response to the leading adjoint OS-mode equals the optimal transient growth, it is observed in all cases that $t^* \approx t_{max}$, where t_{max} is the time at which the maximum transient growth occurs. This suggests that the adjoint of the leading OS-mode is likely to be a good approximation to the optimal initial condition at $t \sim \mathcal{O}(t_{max})$ for all $\alpha \neq 0$ and β. Thus, the evolution of the leading adjoint OS-mode can, at worst, provide valuable insights on the most dominant transient growth mechanisms in a parallel shear flow. This implies that the gain G_{∞}^{OS} (the product of the gains from the 2D Orr-mechanism and the lift-up mechanism) is a good approximation of the maximum optimal gain in these flows.

In figures 5.1−5.5, the large-time optimal response due to the adjoint SQ-mode G_{∞}^{SQ} increases rapidly as the streamwise wavenumber α approaches zero. Consider figure 5.5 corresponding to the case when $\alpha = 0$ and $\beta = 1$ at $Re = 10^5$. Here, the various curves denote the same responses as in figures 5.1−5.3. Note that G_{∞}^{SQ} is very large and the evolution of the adjoint of the first dominant SQ-mode exhibits larger transient growth than that in the case of $\alpha = 0.1$ and $\beta = 1$ at the same Reynolds number. The adjoint of the leading OS-mode, however, grows as large as the maximum optimal growth and its gain Z approximately coincides with the optimal growth curve at all times except at very large time. *The optimal initial condition at $t \sim \mathcal{O}(t_{max})$ for all α and β, up to a first approximation, is the adjoint of the leading OS-mode and the gain G_{∞}^{OS} is a good estimation of the maximum optimal growth.*

By employing the method of Gustavsson[31] and Reddy et. al.[72], the wall-normal vorticity in the Squire equation can be rescaled as $\bar{\eta} = \hat{\eta}/\beta Re$ and $\bar{t} = t/Re$. Thus, when $\alpha = 0$, (5.1), (5.2) and (5.3) become independent of Re and the state vector $\left[\hat{v}, \bar{\eta}\right]^T$ depends only on β. The norm (5.19) of the perturbations in the new variables can then be expressed as

$$E(\bar{t}) = \frac{1}{2} \int_{-1}^{1} \left[|\hat{v}|^2 + \frac{1}{\beta^2} |D\hat{v}|^2 + Re^2 |\bar{\eta}|^2 \right] dy, \tag{5.48}$$

Therefore, if $E_{(\hat{v})}(\bar{t}) = \frac{1}{2}\int_{-1}^{1} \left(|\hat{v}|^2 + \frac{1}{\beta^2} |D\hat{v}|^2 \right) dy$ and $E_{(\bar{\eta})}(\bar{t}) = \frac{1}{2}\int_{-1}^{1} |\bar{\eta}|^2 \, dy$, the growth function (5.16) may be rewritten as:

$$G(\bar{t}) = \max_{\forall \boldsymbol{q}(t_0) \neq \boldsymbol{0}} \left[\frac{E_{(\hat{v})}(\bar{t}) + Re^2 E_{(\bar{\eta})}(\bar{t})}{E_{(\hat{v})}(0) + Re^2 E_{(\bar{\eta})}(0)} \right]. \tag{5.49}$$

Note that the operators L_{OS} and L_{SQ} are self-adjoint in this case. In order to obtain a large gain $G(\bar{t})$ from the lift-up mechanism at $Re >> 1$, it is expensive to have a non-zero normal vorticity in the initial condition [72, 75]. The normal vorticity is zero in the leading adjoint OS-mode whereas it is non-zero in the leading adjoint SQ-mode. Since the optimal initial condition for large time is the leading adjoint eigenmode, it is expected that the gain from transient growth of the adjoint OS-mode is larger than the gain from the transient growth of the adjoint SQ-mode. This is reflected in the results displayed in figures 5.1−5.5, wherein G_{∞}^{OS} is observed to be always larger than G_{∞}^{SQ}. It was noted already that the adjoint of the leading OS-mode exhibits a transient growth as large as the optimal initial condition at t_{max}. The adjoint of the leading SQ-mode, however, does not grow as large because of the presence of a non-zero wall-normal vorticity component.

Figure 5.6 displays the time evolution of the logarithm of optimal transient growth (——) as defined in equation (5.16) and the response $Z = \frac{\|\boldsymbol{q}(t)\|^2}{\|\boldsymbol{q}(t_0)\|^2}$ for various normalized initial conditions similar to figure 5.1. Here, $Re_{2D} = 3000$ and $\alpha_{2D} = 1$, $\beta_{2D} = 0$. In this range of parameters, the leading eigenmode in plane Poiseuille flow is an OS-mode corresponding to Tollmien-Schlichting waves. The response to the adjoint of the leading

OS-mode grows as large as the maximum optimal gain and coincides with the optimal growth curve for all $t/Re > 0.0125$. At $t >> 1$, compared to case shown in figures 5.1−5.5, the logarithm of optimal growth is a single straight line. However, all the observations made in figures 5.1−5.5 are equally valid in this case.

5.6 Conclusion

In summary, the Squire transformation has been extended to obtain eigenvalues of the Squire mode for inclined wave as a function of the $2D$ case and the eigenfunctions of not only the wall-normal velocity but also the wall-normal vorticity. It has all been extended to the eigen-solutions of the adjoint operator with respect to the kinetic energy norm. The transformation then permits us to derive expressions for the large-time optimal gain corresponding to Orr-Sommerfeld and Squire modes at arbitrary wavenumbers and Reynolds numbers in bounded parallel shear flows. Remarkably, the Squire transformation predicts that the long-time optimal gain for OS-modes G_{∞}^{OS} is the product of the gain of the 2D Orr-mechanism at a smaller Reynolds number and a term that can be identified as the contribution from the lift-up mechanism from inclined waves.

The results were verified for arbitrary wavenumbers in the context of plane Poiseuille flow using a direct computation of the optimal gain. It was observed that the leading adjoint OS-mode and G_{∞}^{OS} are good approximations to the optimal initial condition and the maximum optimal transient growth, respectively, in wall-bounded parallel shear flows. If the least stable eigenmode is a Squire mode, the optimal gain curve can be approximated by the response of the adjoint of the leading SQ-mode at $t >> 1$ and the response of the adjoint of the leading OS-mode at intermediate times. If the least stable eigenmode is an Orr-Sommerfeld mode, the optimal growth curve can be well-approximated by the adjoint of the leading OS-mode at all times. This is valid for all wavenumbers and Reynolds numbers.

These results are being brought together as an article to be submitted soon in *Physics of Fluids*.

Chapter 6

Remarks and Perspectives

"I do not know what I may appear to the world, but to myself I seem to have been only like a boy playing on the sea-shore, and diverting myself in now and then finding a smoother pebble or a prettier shell than ordinary, whilst the great ocean of truth lay all undiscovered before me."

– Sir Isaac Newton
Sir Arthur Canon Doyle

A brief summary of perspectives that branch out from this thesis is presented in this chapter.

The optimal growth mechanisms identified in this thesis are expected to motivate experimental investigation in Rayleigh-Bénard-Poiseuille/Couette convection. To the author's best knowledge, no such experiments are available up-to-date. Since Prandtl number is a control parameter in switching on/off the coupling between inviscid lift-up mechanism and the *RB* convection, it would be interesting to decrease/increase the Prandtl number of the fluid, by adding appropriate solvents that change the heat conducting (or viscous diffusion) property of the fluid, to increase/hinder the optimal growth of infinitesimal perturbations in shear flows with heat addition.

The transient growth analysis in the thesis is confined to the stable region in the *Re*-*Ra* plane. It is, however, interesting to study the competition between the exponentially growing modes and algebraically growing perturbations corresponding to control parameters beyond the stable region in *Re*-*Ra* plane. In particular, when $Ra > Ra_c^{RB}$ at some relatively small Reynolds and Prandtl numbers, the growth of the dominant optimal response and the modal response would be comparable. Further work for this parameter range is expected.

It is, also, possible to extend the Squire transformation analysis of the pure shear flow case conducted in chapter 5 to the (direct/adjoint) eigenmodes in Rayleigh-Bénard-Poiseuille/Couette flows. This is due to the fact that the Squire equation is independent of the temperature perturbations. Thus, in this case, one could again look for two sets of solutions:

$$\begin{bmatrix} \hat{v}_j(y) \\ \hat{\theta}_j(y) \\ \hat{\eta}_j^p(y) \end{bmatrix} \quad \text{and} \quad \begin{bmatrix} 0 \\ 0 \\ \hat{\eta}_j(y) \end{bmatrix}, \tag{6.1}$$

so as to write a general solution in the form (4.34). As discussed in section 4.3.4, the former set of solutions are referred to the Orr-Sommerfeld-Oberbeck-Boussinesq ($OSOB$) modes and the latter are the usual Squire modes. Here, the $OSOB$ modes are the solutions of the coupled equations (2.26) for wall-normal velocity and (2.27) for temperature perturbations, involving $\hat{v}$ and $\hat{\theta}$ only; also, $\{\hat{\eta}^p_j\}$'s are the forced wall-normal vorticity functions; and $\{\hat{\eta}_j\}$'s are the solutions of the Squire equation. The Squire transformation is valid also for the equations governing $OSOB$ modes. Thus, all the conclusions derived for the case of pure shear flows in chapter 5 could be possibly extended to the case with temperature perturbations.

Recently, a large family of three-dimensional traveling wave (TW) solutions have been discovered to exist at Reynolds numbers lower than the transitional range in various pure shear flows [64, 20, 11, 12, 22, 23, 83, 84, 38, 37, 78]. It is understood that they arise in saddle-node bifurcations at Reynolds numbers as low as 1250 [23, 84]. The dynamical importance of such structures has been elucidated via a series of numerical and experimental works (see review [19]). It is firmly believed that they provide a framework for the formation of chaotic saddle that can explain intermittent transition: A family of TW solutions can be shown to lie on a surface which separates initial conditions which relaminarize and those which lead to a "turbulent-like" evolution. These are regular solutions of the equations of motion that are embedded in the turbulent dynamics. They were initially called tertiary structures [64, 20, 11, 12] to distinguish them from primary and secondary flows that occur from linear instabilities of the base flow and the primary flow, respectively. In plane Couette flow [64, 11, 12, 83], they are observed to be stationary states whereas, in plane Poiseuille flow [20, 83], they occur only as traveling waves. Both states are coherent structures, dominated by large-scale fluctuations, vortices and streaks. It is also known that these dynamical structures are similar to the ones that exhibit the largest non-modal growth in shear flows [28, 75, 85]. One of the first evidence for such $3D$ TWs was discovered in the case of plane Couette flow with a cross-stream temperature gradient by Clever and Busse [11, 12]. They brought out that some of the $3D$ stationary states can be continued over to the pure plane Couette flow scenario. Remarkably, these states are dominated by vortices aligned in the direction of the base flow, similar to the initial conditions that lead to the largest optimal growth. They, however, "wiggle" in the streamwise direction. It remains, however, inconclusive how these structures are related to optimal initial conditions in pipe flows. In Rayleigh-Bénard-Poiseuille/Couette flows, it would be of academic interest to study the *edge of chaos* [19] which separates perturbations that decay towards laminar profile and those that trigger turbulence. The most akin to the analysis in part I of the thesis is the search for such solutions via direct numerical computations similar to the study by Faisst and Eckhardt [23] and by experiments similar to those presented by B. Hof, C. W. H. van Doorne, J. Westerweel, F. T. M. Nieuwstadt, H. Faisst, B. Eckhardt, H. Wedin, R. R. Kerswell and F. Waleffe [38, 37].

Rayleigh-Bénard-Poiseuille/Couette flows are among the simplest type of flows in which the selection of fully non-linear *global modes* [68, 69] in the context of two-dimensional nonlinear evolution equations can be studied. It is well-known that spatially developing free shear flows such as jets, mixing layers and wakes typically exhibit intrinsic self-sustained oscillations. The origins and the dynamics of such structures can be related to the presence of large regions of absolute instability wherein fluctuations grow indefinitely, only to get saturated at a finite amplitude and become tuned at an overall frequency. Thus, a non-linear *global mode* is such an oscillating state corresponding to a particular spatial distribution of fluctuations beating with an intrinsic frequency depending upon the system. Such structures have been put forward, for instance, by Benoît Pier and Patrick Huerre [68] in the case of one-dimensional nonlinear evolution equations with slowly spatially varying coefficients on a doubly infinite domain. They identified two types of structures, namely, *steep* and *soft* global modes. Steep global modes exhibit a sharp front at a marginally absolutely unstable point and their frequency is determined by the corresponding linear absolute frequency, as in Dee-Langer propagating fronts [68]. Whereas, soft global modes are characterized by slowly varying amplitude over the entire domain and their frequency is determined by the application of a saddle point criterion to the local nonlinear dispersion relation. In the scenario of Rayleigh-Bénard-Poiseuille/Couette flows that vary slowly in the streamwise and spanwise directions, say, an appropriate hot spot in plane Poiseuille/Couette flow, there are many conceptual difficulties in understanding the structure and the development of nonlinear global modes. For example, the definition of front in two-dimensions becomes unclear as the shape and the strength (steepness) of the front will certainly depend on the transverse curvature of the convective/absolute instability boundary. Interestingly, there already exist in the literature linear global modes in these systems for the case of two-dimensional non-uniform temperature distribution in the form of a single hot-spot (Gaussian in the streamwise and spanwise direction) [58]. Also, D. Martinand, P. Carrière and P. A. Monkewitz [57, 8] analyzed the same Rayleigh-Bénard-Poiseuille system in search of linear $3D$ global modes in the framework of envelop equations. It is of both mathematical and dynamical interest to find such nonlinear objects in a slowly varying $2D$ media. Part I of the thesis analyzed Rayleigh-Bénard-Poiseuille/Couette flows for linear temporal instability. Linear spatial instability analysis in such systems have been identified already [7, 29]. Thus, the next step is, perhaps, to look for finite-amplitude solutions that exhibit an overall frequency existing in the linear absolutely unstable regions of the flow. Indeed, one could study such systems starting from a complex Ginzburg-Landau equation in two-dimensions

$$\frac{\partial \boldsymbol{A}}{\partial t} + U\frac{\partial \boldsymbol{A}}{\partial x} = \mu \boldsymbol{A} + |\boldsymbol{A}|^2 \boldsymbol{A} + (1+i\xi)\frac{\partial^2 \boldsymbol{A}}{\partial x^2} + (1+i\zeta)\frac{\partial^2 \boldsymbol{A}}{\partial z^2}, \tag{6.2}$$

where $\boldsymbol{A}(x,z;t)$ is a complex fluctuating scalar field representing the amplitude of the disturbances, ξ and ζ are the dispersion coefficients, $\mu(x,z)$ is the control parameter that determines the linear stability of the basic state $\boldsymbol{A} = 0$ and U is a complex constant. Note that μ is, however, allowed to vary slowly in the streamwise (x-axis) and spanwise (z-axis) directions. This is a simple and easy-to-implement extension of the one-dimensional complex Ginzburg-Landau equation. The linear temporal and spatial stability boundaries are readily obtained by a few algebraic manipulations after a Fourier transform of equation (6.2). In effect, one can obtain a region of absolute instability embedded in a connectively unstable (or stable) region in the x-z plane. The boundary separating these regions can be studied by direct numerical computation of equation (6.2). Such computations are expected to help understand the structure of $2D$ fronts at the absolute-convective boundary and hence, the frequency selection criterion in real flow situations, such as plane Poiseuille/Couette flows with a hot spot, the wake of a circular cylinder with slowly varying diameter in the spanwise direction, etc.

Recent discoveries [30, 39] on large-scale streaks in turbulent plane Couette and Poiseuille flow have reignited a large number of research in wall-bounded turbulent flows [15, 70, 40, 67]. In the near-wall region, streaks, i.e. spanwise alternating patterns of high/low-momentum regions with mean spacing of about 100 wall units, are the most prominent feature of wall-bounded turbulent shear flows. These streaks sustain independently of the turbulent motions in the outer region, and the corresponding process has been understood as a cycle involving amplification of streaks by vortices, breakdown of the streaks via instability and the subsequent nonlinear process generating new vortices [32, 82]. Streaky motions, however, have been also found in the outer region, and they carry a significant fraction of turbulent kinetic energy and Reynolds stress [30, 39]. The self-sustained process at large scales is associated with coherent large-scale streaks that undergo sinuous oscillations and break down to produce coherent large-scale vortices [40] which are gradually damped with time thereby transforming into coherent large-scale streaks. Such a self-sustained process is expected to exist in all wall-bounded shear flows. The effect of heat addition on such large-scale structures have not got any attention so far. It is, however, intriguing to look for such coherent structures and the self-sustaining processes via direct numerical simulations or experiments in Rayleigh-Bénard-Poiseuille/Couette flows.

Bibliography

[1] M. Akiyama, G. J. Hwang, and K. C. Cheng. Experiments on the onset of longitudinal vortices in laminar forced convection between horizontal plates. *J. Heat Transfer*, 93:335–341, 1971.

[2] T. Asai. Cumulus convection in the atmosphere with vertical wind shear: Numerical experiment. *J. Meteor. Soc. Japan*, 42:245–259, 1964.

[3] T. Asai. Three dimensional feature of thermal convection in a plane couette flow. *J. Meteor. Soc. Japan*, 48:18–29, 1970.

[4] H. Bénard. Les tourbillons cellulaires dans une nappe liquide. *Rev. Gen. Sci. Pures Appl.*, 11:1261–1271 and 1309–1328, 1900.

[5] D. Biau and A. Bottaro. The effect of stable thermal stratification on shear flow instability. *Phys. Fluids*, 16(14):4742–4745, 2004.

[6] K. M. Butler and Brian F. Farrell. Three-dimensional optimal perturbations in viscous shear flow. *Phys. Fluids A*, 4:1637–1650, 1992.

[7] P. Carrière and P. A. Monkewitz. Convection versus absolute instability in mixed rayleigh-bénard-poiseuille convection. *J. Fluid Mech.*, 384:243–262, 1999.

[8] P. Carrière, P. A. Monkewitz, and D. Martinand. Envelope equations for the rayleigh-bénard-poiseuille system. part 1. spatially homogeneous case. *J. Fluid Mech.*, 502:153–174, 2004.

[9] K. Chandra. Instability of fluids heated from below. *Proc. Roy. Soc. London A*, 164:231–242, 1938.

[10] S. Chandrasekhar. *Hydrodynamic and Hydromagnetic Stability*. Dover, 1961.

[11] R. M. Clever and F. H. Busse. Three-dimensional convection in a horizontal fluid layer subjected to a constant shear. *J. Fluid Mech.*, 234:511–527, 1992.

[12] R. M. Clever and F. H. Busse. Tertiary and quaternary solutions for plane couette flow. *J. Fluid Mech.*, 344:137–153, 1997.

[13] R. M. Clever, F. H. Busse, and R. E. Kelly. Instabilities of longitudinal convection rolls in couette flow. *Zeit. angew. Math. Phys.*, 28:771–783, 1977.

[14] R. A. Danilov and N. G. A. Ekelund. Phytoplankton communities at different depths in two eutrophic and two oligotrophic temperate lakes at higher latitude during the period of ice cover. *Acta Protozool*, 40:197–201, 2001.

[15] J. C. del Àlamo and J. Jimènez. Linear energy amplification in turbulent channels. *J. Fluid Mech.*, 559:205, 2006.

[16] P. Dennery and A. Krzywicki. *Mathematics for physicists.* Dover, 1996.

[17] R. C. DiPrima and G. J. Habetler. A completeness theorem for non-selfadjoint eigenvalue problem in hydrodynamic stability. *Arch. Rat. Mech. Anal.*, 89:211–228, 1969.

[18] P. G. Drazin and W. H. Reid. *Hydrodynamic Stability.* Cambridge University Press, 1981.

[19] B. Eckhardt, T. M. Schneider, B. Hof, and J. Westerweel. Turbulence transition in pipe flow. *Ann. Rev. of Fluid Mech.*, 39(1):447–468, 2007.

[20] U. Ehrenstein and W. Koch. Three-dimensional wavelike equilibrium states in plane poiseuille flow. *J. Fluid Mech.*, 228:111–148, 1991.

[21] T. Ellingsen and E. Palm. Stability of linear flow. *Phys. Fluids*, 18(4):487–488, 1975.

[22] H. Faisst and B. Eckhardt. Transition from the couette-taylor system to the plane couette system. *Phys. Rev. Lett. E*, 61:7227–7230, 2000.

[23] H. Faisst and B. Eckhardt. Traveling waves in pipe flow. *Phys. Rev. Lett. E*, 91, 2003.

[24] Brian F. Farrell. Optimal excitation of perturbations in viscous shear flows. *Phys. Fluids*, 31(8):2093–2102, 1988.

[25] K. Fujimura and R. E. Kelly. Stability of unstably stratified shear flow between parallel plates. *Fluid Dyn. Re.*, pages 281–292, 1988.

[26] K. S. Gage and W. H. Reid. The stability of thermally stratified plane poiseuille flow. *J. Fluid Mech.*, 33:21–32, 1968.

[27] A. P. Gallagher and A. McD. Mercer. On the behavious of small disturbance in plane couette flow with a temperature gradient. *Proc. Roy. Soc. London*, 286:117–128, 1965.

[28] A. P. Gallagher and A. McD. Mercer. On the instability of pipe poiseuille flow. *Phys. Fluids*, 8(11):2923–2932, 1996.

[29] E. Grandjean and P. A. Monkewitz. Experimental investigation into localized instabilities of mixed rayleigh-bénard-poiseuille convection. *J. Fluid Mech.*, 640:401–419, 2009.

[30] M. Guala, S.E. Hommema, and R.J. Adrian. Large-scale and very-large-scale motions in turbulent pipe flow. *J. Fluid Mech.*, 554:521–541, 2006.

[31] L. Gustavsson. Energy growth in three-dimensional disturbances in plane poiseuille flow. *J. Fluid Mech.*, 224:241–260, 1991.

[32] J.M. Hamilton, J. Kim, and F. Waleffe. Regeneration mechanisms of near-wall turbulence structures. *J. Fluid Mech.*, 287:317–348, 1995.

[33] S. R. Hanna. The formation of longitudinal sand dunes by helical eddies in the atmosphere. *J. Appl. Meteor.*, 8:874–883, 1969.

[34] N. Harnik and E. Heifetz. 100 years to the orr mechanism of shear instability. http://mathsci.ucd.ie/met/seminars/Orr_Heifetz.ppt.

[35] H. Helmholtz. Über discontinuierliche flüssigkeits-bewegungen. *Monatsberichte der Königlichen Preussische Akademie der Wissenschaften zu Berlin*, 23:215–228., 1868.

[36] I. H. Herron. A completeness observation on the stability equations for stratified viscous shear flows. *Phys. Fluids*, 23:836–837, 1980.

[37] B. Hof, C. W. H. van Doorne, J. Westerweel, and F. T. M. Nieuwstadt. Turbulence regeneration in pipe flow at moderate reynolds numbers. *Phys. Rev. Lett.*, 95(214502), 2005.

[38] B. Hof, C. W. H. van Doorne, J. Westerweel, F. T. M. Nieuwstadt, H. Faisst, B. Eckhardt, H. Wedin, R. R. Kerswell, and F. Waleffe. Experimental observation of nonlinear traveling waves in turbulent pipe flow. *Science*, 305(5690):1594–1598, 2004.

[39] N. Hutchins and I. Marusic. Evidence of very long meandering features in the logarithmic region of turbulent boundary layers. *J. Fluid Mech.*, 579:1–28, 2007.

[40] Y. Hwang and C. Cossu. Self-sustained process at large scale in turbulent channel flow. *Phys. Rev. Lett.*, 105:044505, 2010.

[41] M. P. Idrac. Sur les courants de convection dans l'atmosphère dans leur rapport avec le vol à voile et certains formes de nuages. *Comptes Rendus*, 171:42–44, 1920.

[42] M. P. Idrac. Some experiments on periodic columnar forms of vortices caused by convection. *Rep. Aero. Res. Inst. University of Tokyo*, 3:1–52, 1928.

[43] A. P. Ingersoll. Convective instabilities in plane couette flow. *Phys. Fluids*, 9:682–689, 1966.

[44] D. D. Joseph. Nonlinear stability of the boussinesq equations by the method of energy. *Arch. Rational Mech. Anal.*, 22:163–184, 1959.

[45] D. D. Joseph. *Stability of fluid motions I.* Springer-Verlag, 1976.

[46] Dan E. Kelley. Convection in ice-covered lakes: effects on algal suspension. *J. Plankton Res.*, 19(12):1859–1880, 1997.

[47] R. E. Kelly. The onset and development of thermal convection in fully developed shear flows. *Adv. Appl. Mech.*, 31:35–112, 1994.

[48] Lord W. T. Kelvin. Hydrokinetic solutions and observations. *Phil. Magazine*, 42:362–377., 1871.

[49] J. M. Kendall. Experimental study of disturbances produced in a pre-transitional laminar boundary layer by weak freestream turbulence. *AIAA paper*, pages 85–1695, 1985.

[50] P. S. Klebanoff. Effects of free-stream turbulence on a laminar boundary layer. *Bull. Am. Phy. Soc.*, 16, 1971.

[51] E. Kreyszig. *Advanced engineering mathematics.* Wiley, 2001.

[52] J . P. Kuettner. Cloud bands in the earth's atmosphere. *Tellus*, pages 404–425, 1971.

[53] M. T. Landhal. A note on the algebraic instability of inviscid parallel shear flows. *J. Fluid Mech.*, 98:243–251, 1980.

[54] P. Luchini. Reynolds-number-independent instability of the boundary layer over a flat surface: optimal perturbations. *J. Fluid Mech.*, 404:289–309, 2000.

[55] M. Malik, A. Dey, and M. Alam. Linear stability, transient energy growth, and the role of viscosity stratification in compressible plane couette flow. *Phy. Rev. E*, 77:036322–1–036322–15, 2008.

[56] D. Martinand. *Détermination analytique des modes globaux tridimensionnels en écoulement de convection mixte du type Rayleigh-Bénard-Poiseuille.* PhD thesis, École Centrale Lyon, Lyon, France, 2003.

[57] D. Martinand, P. Carrière, and P. A. Monkewitz. Envelope equations for the rayleigh-bénard-poiseuille system. part 2. linear global modes in the case of two-dimensional non-uniform heating. *J. Fluid Mech.*, 502:175–197, 2004.

[58] D. Martinand, P. Carrière, and P. A. Monkewitz. Three dimensional global instability modes associated with a localized hot spot in rayleigh-bénard-poiseuille convection. *J. Fluid Mech.*, 551:275–301, 2006.

[59] masdys. Gravity wave clouds.
http://www.youtube.com/watch?v=NPLLeJKStAo&feature=player_embedded.

[60] M. Matsubara and P. H. Alfredsson. Disturbance growth in boundary layers subjected to free-stream turbulence. *J. Fluid Mech.*, 430:149–168, 2001.

[61] H. W. Müller. *Thermische Konvektion in Horizontaler Scherströmung.* PhD thesis, Universität des Saarlandes, Saarlandes, 1990.

[62] M. V. Morkovin. Critical evaluation of transition from laminar to turbulent shear layer with emphasis on hypersonically traveling bodies. *AFFDL Tech. Rep.*, pages 68–149, 1968.

[63] M. V. Morkovin. Bypass transition to turbulence and research desiderata. *Transition in Turbines*, pages 161–204, 1984.

[64] M. Nagata. Three-dimensional finite-amplitude solutions in plane couette flow: bifurcation from infinity. *J. Fluid Mech.*, 217:519–527, 1990.

[65] W. M. F. Orr. The stability or instability of the steady motions of a perfect liquid and of a viscous liquid. *Proc. R. Irish Acad. A*, 27:9–138, 1907.

[66] M. N. Ouarzazi, F. Mejni, A. Delache, and G. Labrosse. Nonlinear global modes in inhomogeneous mixed convection flows in porous media. *J. Fluid Mech.*, 595:367–377, 2008.

[67] J. Park, Y. Hwang, and C. Cossu. On the stability of large-scale streaks in turbulent poiseulle and couette flows. *C. R. Mecanique.*, 2010.

[68] B. Pier and P. Huerre. Fully nonlinaer global modes in spatially developing media. *Physica D*, 97(10):2433–2435, 1996.

[69] B. Pier, P. Huerre, J-M. Chomaz, and A. Couairon. Steep nonlinear global modes in spatially developing media. *Phys. of Fluids*, 10:206–222, 1998.

[70] G. Pujals, M. Garcìa-Villalba, C. Cossu, and S. Depardon. A note on optimal transient growth in turbulent channel flows. *Phys. Fluids*, 21:015109, 2009.

[71] Lord John W. S. Rayleigh. On convective currents in a horizontal layer of fluid when the higher temperature is on the under side. *Phil. Mag.*, 32:529–546, 1916.

[72] S. C. Reddy and D. S. Henningson. Energy growth in viscous channel flows. *J. Fluid Mech.*, 252:209–238, 1993.

[73] O. Reynolds. An experimental investigation of the circumstances which determine whether the motion of water in parallel channels shall be direct or sinuous and of the law of resistance in parallel channels. *Philos. Trans. R. Soc.*, 174:935–982, 1883.

[74] A. Sameen and R. Govindarajan. The effect of wall heating on instability of channel flow. *J. Fluid Mech.*, 577:417–442, 2007.

[75] P. J. Schmid and D. S. Henningson. *Stability and transition in shear flows.* Springer, 2001.

[76] Peter J. Schmid. Nonmodal stability theory. *Ann. R. Fluid Mech.*, 39:129–162, 2007.

[77] J. Serrin. On the stability of viscous fluid motions. *Arch. Rational Mech. Anal. (1)*, 3:1–13, 1959.

[78] J. D. Skufca, J. A. Yorke, and B. Eckhardt. Edge of chaos in a parallel shear flow. *Phys. Rev. Lett.*, 96, 2006.

[79] Spluchsters. Cloud streets.
http://spluch.blogspot.com/2008/03/cloud-streets.html.

[80] H. B. Squire. On the stability of 3d disturbances of viscous flow between parallel walls. *Proc. Roy. Soc. London A*, 142:621–628, 1933.

[81] G. I. Taylor. Stability of a viscous liquid contained between two rotating cylinders. *Phil. Trans. Royal Society A*, 223:289–343., 1923.

[82] F. Waleffe. On a self-sustaining process in shear flows. *Phys. Fluids*, pages 883–900, 1997.

[83] F. Waleffe. Homotopy of exact coherent structures in plane shear flows. *Phys. Fluids*, 15:1517–1534, 2003.

[84] H. Wedin and R. R. Kerswell. Exact coherent structures in pipe flow: traveling wave solutions. *J. Fluid Mech.*, 508:333–371, 2004.

[85] O. Y. Zikanov. Optimal energy growth in hagen-poiseuille flow. *J. Fluid Mech.*, 277:197, 1994.

Résumé

Les mécanismes de croissance optimale dans des écoulements de cisaillement confinés, en particulier les écoulements de Couette plan et Poiseuille plan, lorsqu'ils sont soumis ou non à un gradient de température déstabilisant normal à la paroi sont étudiés en détail. Dans le cas d'un fluide de Boussinesq soumis à un gradient de température transverse, une analyse exhaustive de stabilité non modale est effectuée pour différents nombres de Reynolds, de Rayleigh et de Prandtl. On montre que les lois d'échelle relatives à la croissance transitoire dans des écoulements cisaillés purs sont robustes, y compris en présence d'un gradient de température déstabilisant. Le mécanisme de "lift-up" non visqueux classique caractérise le comportement aux temps courts alors que le mode propre de Rayleigh-Bénard sans sa composante de vitesse longitudinale caractérise le comportement aux temps longs. Dans le cas d'écoulements cisaillés purs, le rôle de transformation de Squire est étendue à la croissance transitoire optimale d'une perturbation arbitraire 3D dans le cas d'écoulements cisaillés parallèles d'extention transverse finie. Cela permet aussi de démontrer que les croissances optimales aux temps longs pour des perturbations de nombre d'onde arbitraires peuvent être décomposées comme un produit des gains respectifs résultant du mécanisme de Orr 2D et du mécanisme de "lift-up".

MOTS CLÉS: la croissance transitoire, Rayleigh-Bénard, Poiseuille, Couette flow, transformation de Squire

Abstract

Optimal growth mechanisms in wall-bounded shear flows, in particular, plane Couette and plane Poiseuille flow, with and without a destabilizing wall-normal temperature gradient are studied extensively. In the case with a cross-stream temperature gradient in a Boussinesq fluid, a comprehensive non-modal stability analysis is performed over various Reynolds, Rayleigh and Prandtl numbers. The scaling laws pertaining to transient growth in pure shear flows are shown to hold even in the presence of a destabilizing temperature gradient. The lift-up effect remains the predominant transient growth mechanism. The classical inviscid lift-up mechanism characterizes the *short-time* behavior whereas the Rayleigh-Bénard eigenmode without its streamwise velocity component characterizes the *long-time* behavior. The Squire transformation is extended to provide new insights on the optimal growth of arbitrary 3D disturbances in parallel shear flows bounded in the cross-stream direction. It also permits to demonstrate that the *long-time* optimal growth for perturbations of arbitrary wavenumbers may be decomposed as a product of the respective gains arising from the $2D$ Orr-mechanism and the lift-up mechanism. This asymptotic solution is shown to describe the *long-time* and even the *intermediate-time* dynamics of the optimal disturbances and provides a good estimate of the maximum optimal gain at all time.

KEYWORDS: transient growth, Rayleigh-Bénard, Poiseuille, Couette flow, Squire's transformation